A Microhotplate for Gas Sensing and Vacuum Measurements

Dmytry Grudin

A Thesis

In the Department

of

Electrical and Computer Engineering

Presented in Partial Fulfillment of the Requirements

for the Degree of Master of Applied Science (Electrical and Computer Engineering)

Concordia University

Montreal, Quebec, Canada

May 2020

CONCORDIA UNIVERSITY

SCHOOL OF GRADUATE STUDIES

This is to certify that the thesis prepared

By: Dmytry Grudin

Entitled: A Microhotplate for Gas Sensing and Vacuum Measurements

and submitted in partial fulfillment of the requirements for the degree of

Master of Applied Science (Electrical and Computer Engineering)

complies with the regulations of this University and meets the accepted standards with respect to originality and quality.

Signed by the final examining committee:

_____ Chair

Dr. A.K. Rathore

_____ External Examiner

Dr. J. Dargahi (MIAE)

_____ Internal Examiner

Dr. I. Stateikina

_____ Supervisor

Dr. Mojtaba Kahrizi

Approved by: _____

Dr. Y. R. Shayan, Chair

Department of Electrical and Computer Engineering

_____20____ _____

Dr. Mourad Debbabi, Interim Dean

Gina Cody School of Engineering and Computer Science

ABSTRACT

This thesis is devoted to the design, analysis and characterization of the thermal sensor based on Complementary Metal-Oxide-Semiconductor, (CMOS) compatible microhotplate (MHP). The MHP contains a split electric heater and temperature sensor, has a small area of $0.02mm^2$ and operates at low overheating temperature. These features of the sensing element which are not typical for traditional thermal sensors have been selected to compromise restrictions imposed by the CMOS fabrication process and materials available for the building of functional elements.

The operating mode of the sensor, signal processing algorithms and the layout of the MHP were analyzed and adjusted such that to provide a stable and low noise operation even with potentially unstable poly-Si as the material used for the heater and temperature sensor. It was experimentally demonstrated that the proposed approach allows to detect extremely small variations of CO_2 and O_2 concentration in air. The sensor tested as a vacuum gauge demonstrated good sensitivity down to 1mTorr.

The developed MHP due to its small size and true compatibility with CMOS fabrication process has good potential for volume production and can be used in applications where miniature and inexpensive sensors are needed. Freeze drying technology widely used in the pharmaceutic industry is suggested to be one of the possible applications for the developed sensor. It was demonstrated that the network of the developed thermal sensors can be used to monitor water sublimation during primary drying stage that may have an important practical value for the improvement of the quality and efficiency of the freeze drying process.

TABLE OF CONTENTS

List of Figures:

List of Tables:

CHAPTER 1: INTRODUCTION

1.1 Motivation/Brief Description

Thermal conductivity sensors are widely used in industrial applications, biological and pharmaceutical technology, and medicine in order to measure different gas compositions and vacuum pressure. Examples of such applications include, freeze-drying [1], gas sensing [2, 9-11, 13, 14], humidity sensing [3-6] and vacuum pressure measurements [7-8, 12].

MEMS (Microelectromechanical systems) technology allows to build a Micro-Hot Plate, MHP which is a basic functional element of a Thermal Conductivity, TC sensor. An MHP typically possesses a high level of thermal isolation from the bulk Silicon chip and can be heated to significant temperatures by dissipating low electrical power [15]. Different fabrication techniques and a big variety of materials for the functional element of the TC sensor have been used in the last decades. Bulk micromachining including back side and front side Silicon etching and surface micromachining were used for releasing of the MHP [19]. TC sensors are attractive due to their simple operating mode and processing electronics.

The motive of the present research is to investigate the possibility to design a CMOS compatible TC sensor with high performance for vacuum applications primarily for freeze drying technique as well as to determine technical solutions which can overcome certain limitations imposed by the need to follow design rules specific to CMOS process.

Thermal gas sensors based on MEMS micro-hot plates, MHPs along with the use of thermal conductivity of an ambient gas as a measured parameter are used for identification of gas compositions and absolute pressure measurements. The operating principle is based on the evaluation of heat loss through the surrounding gas which depends on the thermal conductivity of a gas and concentration of gas molecules in the case of vacuum pressure measurements. In order to measure the heat loss coefficient, HLC, the ratio of overheating temperature to electrical power dissipated on the MHP is measured.

Typical thermal sensors contain a sensing element made from metal films such as molybdenum, nickel, platinum or other materials with a high temperature coefficient of resistance, TCR and good long-term stability [16-18]. Usage of such materials which are not typical for standard CMOS process requires an introduction of additional customized fabrication steps that complicates the whole manufacturing process.

The design of thermal gas sensors with a high level of compatibility with existing CMOS fabrication process is of certain interest especially if good manufacturability and small size of the sensing element are required. Designers of such sensors must apply serious efforts to overcome limitations imposed by CMOS compatibility.

One of the main limitations is the marginal quality of polysilicon as a material used for the temperature sensing element. By varying doping levels, it is possible to increase the TCR of polysilicon resistors. However, it is still significantly lower than the TCR of metal film resistors. The stability of polysilicon resistors is typically worse than the stability of metal film resistors. It will be shown how these limitations can be compensated by implementing a special design of the sensing element, electronic circuitry and signal processing algorithm.

If the MHP is fabricated using a custom dedicated process, its size and shape can be varied in a wide range. If the fabrication of the MHP is performed by post-processing of a CMOS wafer, etching is performed after all functional elements including bonding pads have already been created on a wafer surface. In this case, the etching time may be limited which also limits the size of the MHP. A small MHP size is preferable to reduce the entire size of the whole Silicon chip.

1.2 Targets/Objectives

The main target of this project was to design and characterize and optimize a thermal gas sensor for vacuum pressure sensing. CMOS technology combined with MEMS post-processing allows to fabricate miniature Silicon sensing elements on dies with dimensions of about 1-2mm and low-cost at batch production. Thermal gas sensors characterized in the present project were built with the existing technology owned by First-Sensor Corp, 1980 Sherbrooke St. West Suite 220, Montreal, QC, H3H 1E8.

Basic characteristics of the TC sensor such as sensitivity to variation of gas thermal conductivity and resolution of measurements are to be investigated.

The use of TC sensor in freeze drying process where the control of primary drying stage is of special interest. The sensors' network for monitoring of the process of water sublimation at vacuum was designed and tested.

1.3 Thesis Organization

The subsequent chapters are briefly explained below.

Chapter 2: Thermal Sensors

In this chapter, a description of a thermal sensor will be presented along with an operating principle of thermal conductivity sensors and their functionality. Applications of thermal sensors will be discussed primarily in the field of freeze drying.

Chapter 3: Design of a CMOS Compatible TC Sensor

The design of the device and properties of polysilicon resistors of the MHP as a basic functional element of the sensor will be analyzed. The physical interaction between the MHP and the molecules in the medium will be considered. Signal waveforms of the heater and sensor nodes will be shown to demonstrate the underlying operation of the MHP. Finally, the MHP's resistance and overheating temperature will be presented as a function of power to demonstrate the TCR of the heater and sensor resistors.

Chapter 4: Simulation of Temperature Distribution of the MHP

Temperature distribution of the MHP will be depicted portraying the comparison between COMSOL simulation and Python simulation. Results will be analyzed for an input current of 1mA. Afterwards, the temperature distribution of two TCR cases will studied. The first case with an approximated TCR of the Polysilicon; the second case with an experimentally determined TCR of the Polysilicon. Results will be compared and analyzed. An improvement of the temperature uniformity will be shown by placing an Aluminum slab across the MHP to stabilize the overheating

temperature. Finally, three temperatures profiles will be analyzed for currents of 0.6, 0.7 and 0.8mA.

Chapter 5: Experimental Measurements

In this chapter, a brief background of gas and pressure sensing of the aforementioned device will be explained. Data acquisition and signal processing of the MHP will be described. The sensor will be placed inside the vacuum chamber to detect its sensitivity to a variety of gases and water. Afterwards, measurements with two Pirani-type sensors will be performed to detect pressure gradients inside the chamber during water sublimation. Detection of pressure gradients with three thermal conductivity sensors in the presence of water will be demonstrated. Special Visual Basic application for this application will be described. Experimental results will be discussed. Lastly, detection of pressure gradients in a real freeze drying process will be shown.

Chapter 6: Design of a TC Sensor Using PolyMUMPs Process

Alternative design of a MHP based on PolyMUMPs process will be presented. A layout design was made with Cadence Virtuoso.

CHAPTER 2: THERMAL SENSORS

2.1 Description of MEMS Thermal Sensor

MEMS is an abbreviation for microelectromechanical systems. MEMS have been used to describe micro-miniature systems that are constructed with both Integrated Circuit, IC based fabrication techniques and other mechanical fabrication techniques [24]. In many cases, designers developing sensors for temperature, pressure, flow, humidity, gas composition measurements, etc [25] apply special efforts to implement methods for building micro-structures which are compatible with IC techniques to ensure availability of signal processing electronics close to MEMS sensing elements [26].

In this chapter, two techniques for the fabrication of microelectromechanical devices will be introduced: *Bulk micromachining* and *Surface micromachining*.

Bulk micromachining:

Areas of single crystal silicon that have first been exposed through a photo mask are removed by alkaline chemicals. The process of bulk micromachining consists of etching which can produce concave, pyramidal or V-shaped grooves depending on the direction and angle of the cut [27]. Using these methods, it is possible to obtain sculpted-out cavities which can become building blocks for MHP [24]. Fig 2-1 and 2-2 depict back-side and front-side etching of the MHP, respectively.

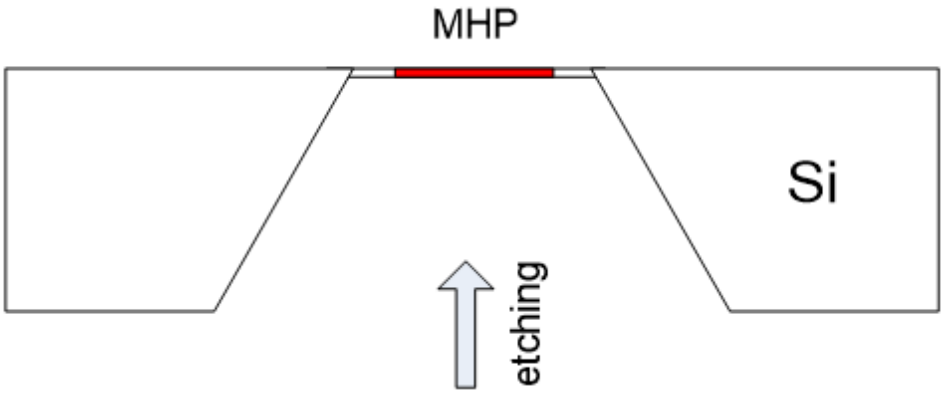

Fig. 2-1: Fabrication of the MHP using back-side etching

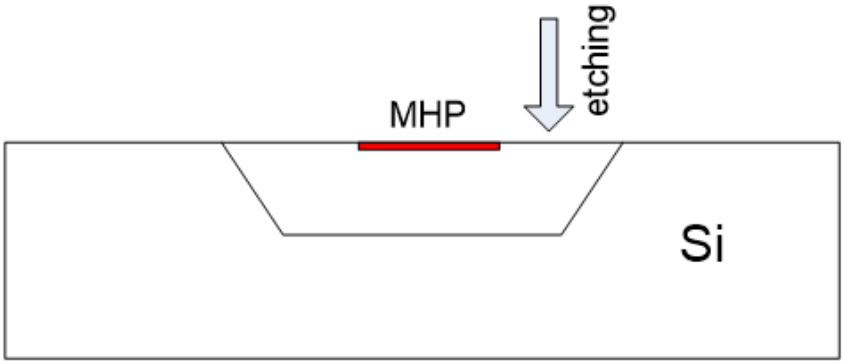

Fig. 2-2: Fabrication of the MHP using front-side etching

Surface micromachining:

The fabrication process of surface micromachining is a method by depositing, patterning and etching a sequence of thin films usually in the range of 1-10µm thick [28]. One of the steps consists of depositing a sacrificial layer on top of the substrate with a patterned window for the anchor. In the subsequent step, a structural layer is deposited on top of the sacrificial layer. Finally, the sacrificial layer is etched using selective etching such as hydrofluoric acid, HF for etching SiO_2 [29]. These steps may be repeated for further consecutive layer additions. As a result, suspended structure(s) are formed on top of a substrate. Fig. 2-3 shows a suspended MHP over the substrate.

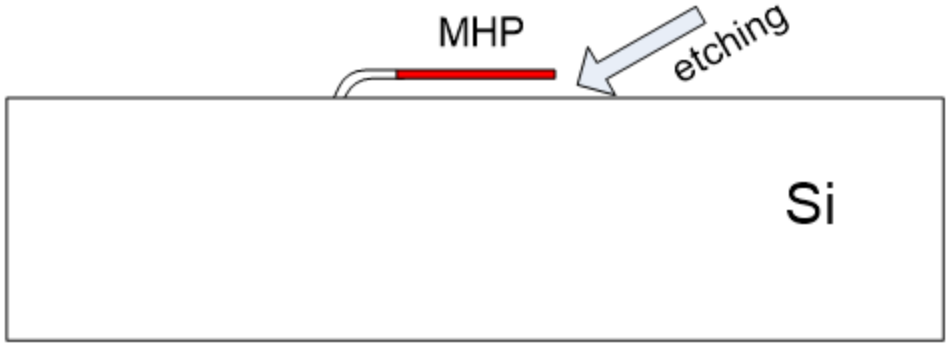

Fig. 2-3: Fabrication of the MHP using surface micromachining

Sensing elements fabricated by any of the techniques described above are fragile and can be damaged during silicon wafer dicing. To protect MEMS structures, different methods are used. Fig. 2-4 shows one possible solution where the sensing element of the thermal sensor is protected with a bonded Si top cap with pre-etched cavities. This approach was used to build thermal flow sensors [30]. The thermal conductivity sensor investigated in the present project has a similar structure containing the MHP fabricated using bulk micromachining technique with front side etching and protected with a Si top cap with an opening in it to connect the MHP with ambient gas medium. The design of the sensor is schematically shown on Fig. 2-4.

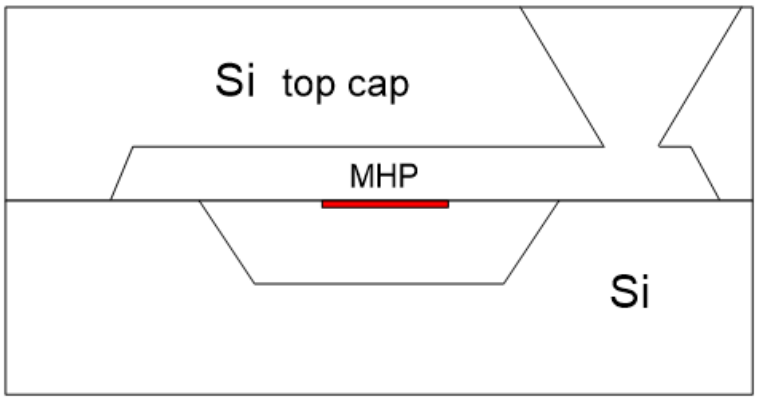

Fig. 2-4: Example of the thermal sensor with a top cap protection

2.2 Operating Principle of Thermal Conductivity Sensors

The fundamental principle of a TC sensor is based on the interaction of the heated MHP with an ambient gas medium. When electric power is applied, the overheating of the MHP causes heat transfer into the environment. During this process, gas molecules collide with the MHP and trap the dissipated heat. The heated molecules float away with the collected heat which results in a cooling of the MHP. For low pressures, gas is rarified and fewer molecules manage to collide with the surface of the MHP to trap the collected heat. As a result, the Heat Loss Coefficient, HLC is low. For high pressures, the inverse process happens. The gas is abundant of molecules forcing many molecules to collide with the MHP to trap heat. In this case, the HLC is high providing a higher heat exchange with an ambient gas. Fig. 2-5 depicts an analogous graphical representation of the working principle of the classical vacuum TC sensor [21].

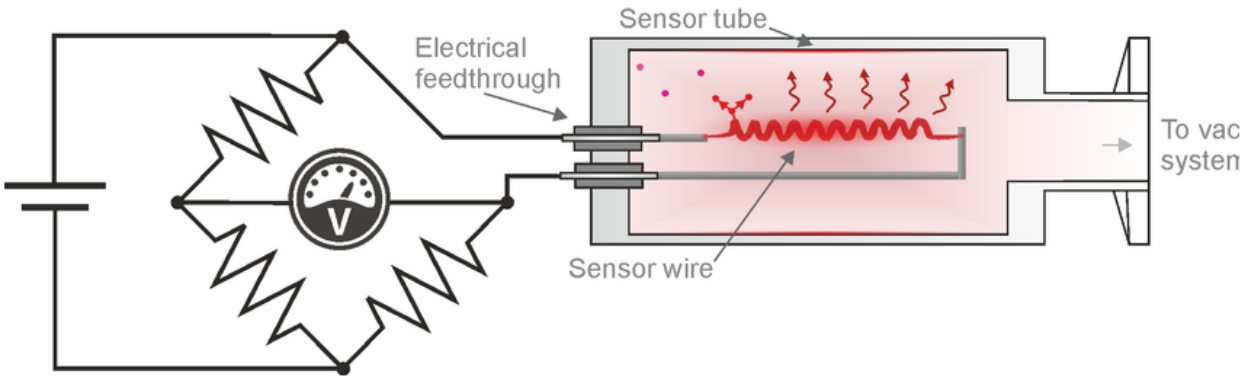

Fig. 2-5: Analogous graphical representation of the working principle of the MHP

As observed on the figure above, the heating element's heat is gathered by the molecules of the gas inside a vacuum system.

2.3 Applications for Thermal Gas Sensors

TC sensors detect and measure gas concentrations between 0 and 100% of the volume. Measurements of gas mixture compositions are possible if the mixed gases have significantly different thermal conductivities. Examples of such mixed gases with air include Helium, Methane, Carbon dioxide, Argon, and other hydrocarbons. Fig. 2-6 presents thermal conductivities of some gases as a function of temperature [41].

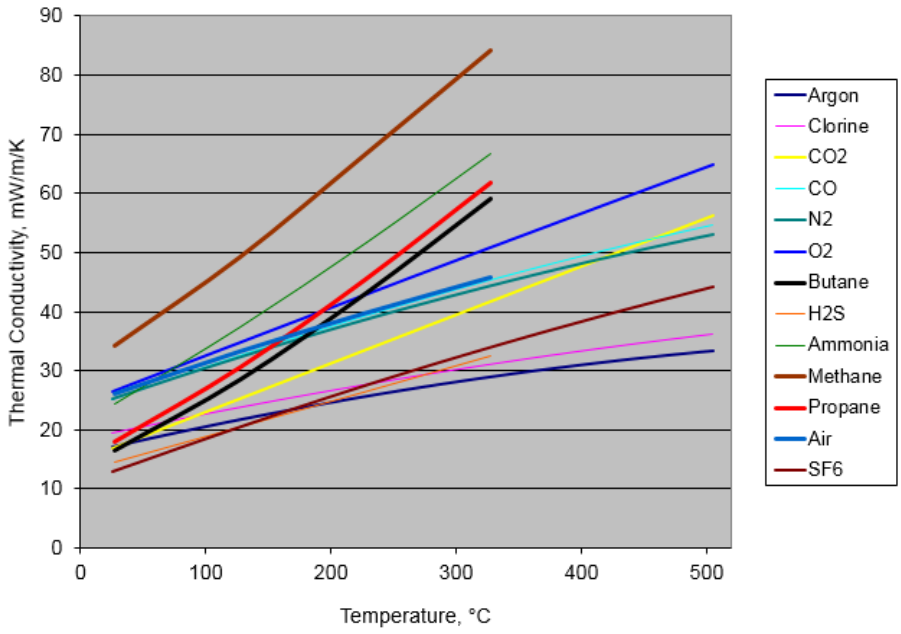

Fig. 2-6: Thermal conductivities of various gases [41]

2.3.1 Freeze Drying

Freeze drying technology is one of the main applications where thermal sensors can be potentially employed. A certain explanation of the problems which can be mitigated with thermal sensors is required.

Freeze-drying or Lyophilization is a process in which a product is dried under low temperature and vacuum pressure [1, 22, 23]. The water in the frozen sample is directly removed by turning the ice into vapor. The unique advantage of Freeze-drying is that samples remain frozen during the entire drying process, thereby preserving thermo-labile components such as proteins, flavors, colors and texture, while maintaining the original shape, size and composition. The dried substances such as microorganisms, food, biological and pharmaceutical products can then be stored for long periods of time without the risk of changing the composition or being infected by microorganisms, which is all done due to a lack of water.

The primary drying phase is the main component of Freeze-drying. During this stage, the ice sublimates under ultra-low pressure, typically in the range of 100mTorr or lower. The driving force of sublimation is the pressure difference related to the corresponding temperature difference between the product's ice surface and the condenser's ice surface. Therefore, meticulous monitoring of pressure differences during Freeze-drying can be a possible indicator of the end of sublimation. Fig. 2-7 shows an example of one of the shelves with vials containing drying material loaded inside the vacuum chamber.

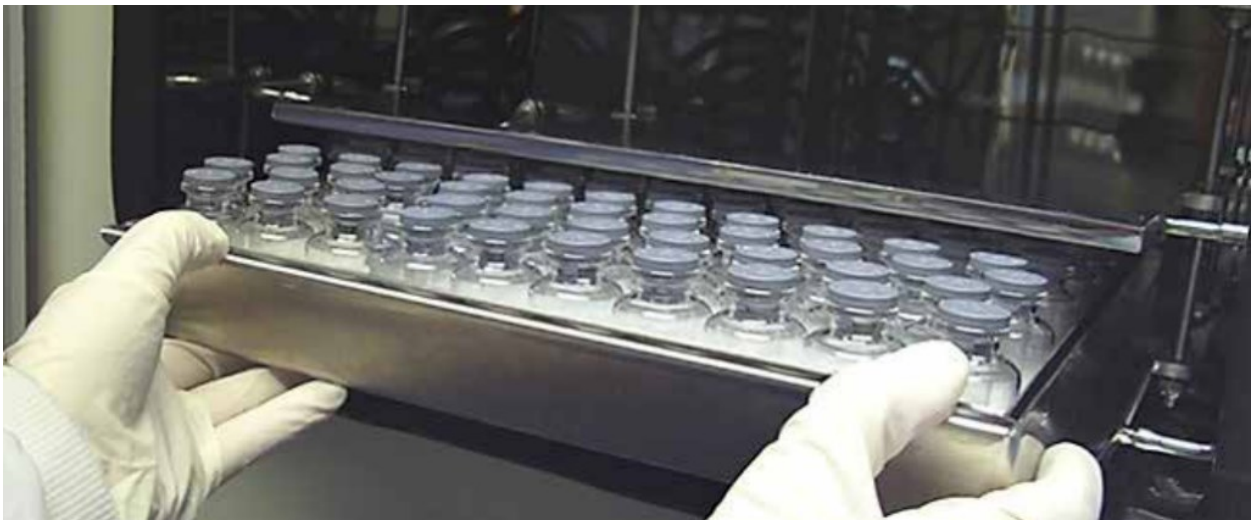

Fig. 2-7: A shelf with vials loaded inside the vacuum chamber

Freeze-drying is an expensive process with relatively long processing times (tens of hours) where primary drying is the longest step, and hence, optimization of this step is the focus in the industry. The end point of primary drying is determined by several techniques which have certain limitations [1]:

- Comparative pressure measurements (ie. Pirani sensor vs MKS Baratron)
- Dewpoint, lyotrack (gas plasma spectroscopy)
- Water concentration from a tunable diode laser absorption spectroscopy

The possibility of determining the end of primary drying stage by monitoring pressure gradients inside the vacuum chamber will be investigated. It is known that pressure gradients between the condenser which may be cooled down to very low temperatures (to about -60°C or lower) and the vials with drying materials (maintained at approximately -10°C) is the driving force for water vapor transport. The end of sublimation (end of primary drying) must affect the pressure gradients in the chamber in order for it to be detected by the pressure sensors.

It is assumed that miniaturized thermal pressure sensors are capable of measuring pressures in the range of 10 – 300mTorr and can be placed in multiple locations between the shelves of the freeze dryer and nearby the condenser. By processing signals from this network of pressure sensors, it is possible to detect the end of primary drying stage.

CHAPTER 3: DESIGN OF A CMOS COMPATIBLE TC SENSOR

3.1 Characterization of polySi Resistors

The performance of thermal sensors depends in great extent on the characteristics of temperature sensitive elements. The requirements of CMOS compatibility restrict the choice of materials of thermo-resistors with polysilicon. Two types of polysilicon, poly_A and poly_B with different doping levels were available in the fabrication process. The third type of polysilicon with a lower sheet resistance which is doped with Phosphorus was used as a material for the resistive heater.

The TCRs of poly_A and poly_B resistors were measured in a temperature range from -20°C to 150°C in the laboratory oven SD302 (Associated Environmental Systems) and from 150°C to 250°C in the laboratory oven EC10 (Sun Electronic Systems Inc.). Measurement results are presented in Fig. 3-8. For both types of polysilicon, absolute values of *TCR* reduce significantly with an increase of temperature.

In Fig. 3-9, in the narrower temperature range from 0°C to 150°C, TCRs can be approximated with an acceptable accuracy by a linear function of temperature presented in equation (3-1):

$$TCR = \alpha + \beta(T - T_0), \tag{3-1}$$

where T_0 is the room temperature which is approximately equal to 22°C.

The values for coefficients α and β are shown in Table 1.

Table 1: Values of TCRs of poly_A and poly_B

	Poly_A	Poly_B
α, ppm/K	-1324.4	-2511.8
β, ppm/K^2	1.64	4.33

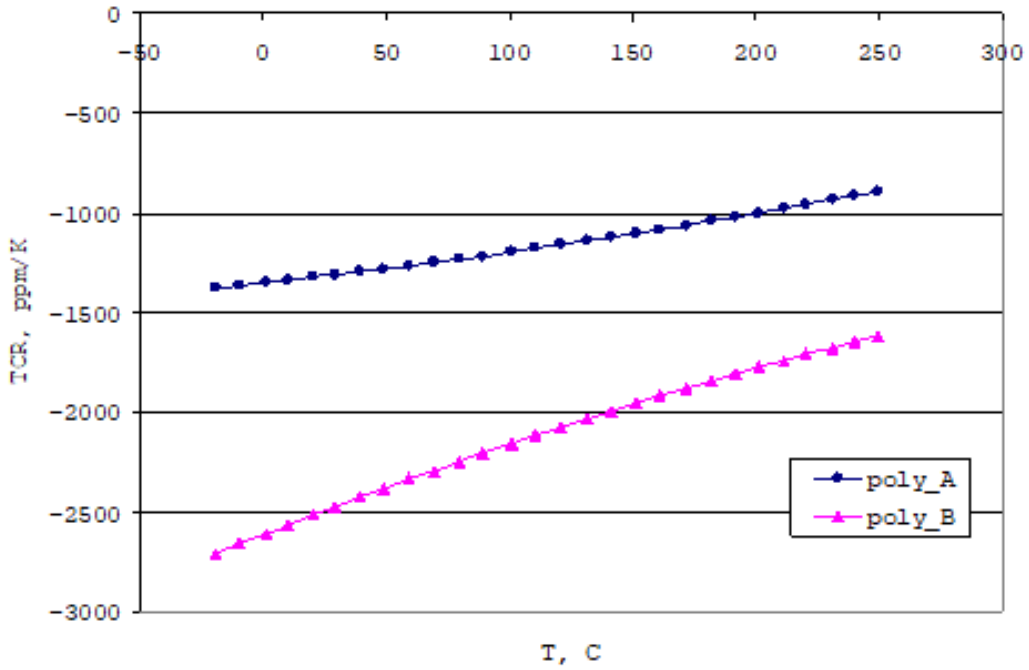

Fig. 3-8: TCR of polysilicon resistors

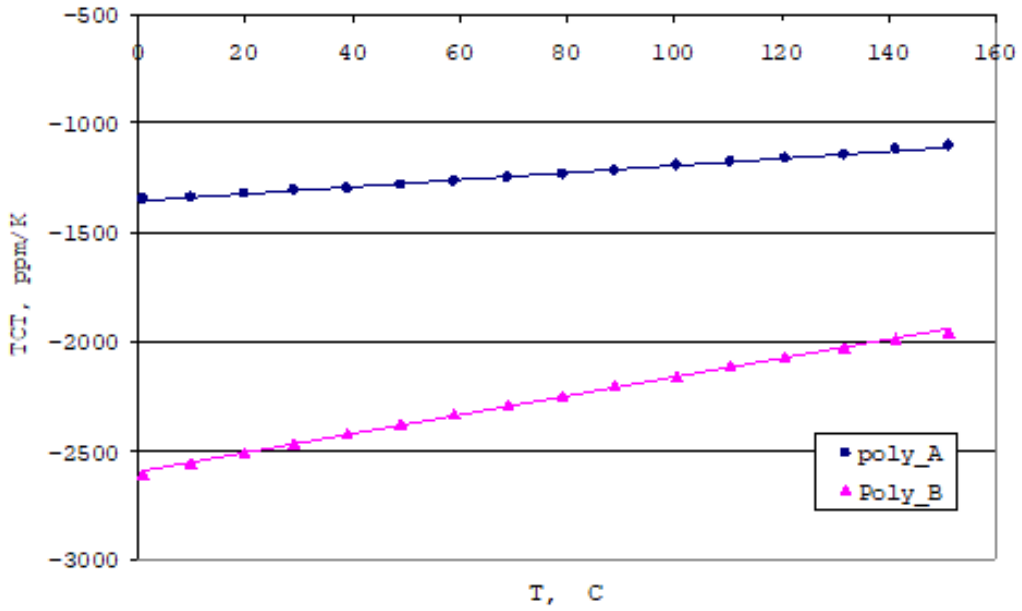

Fig. 3-9: TCR of polysilicon resistors from 0°C to 150°C

Calculation of the temperature of the MHP based on the measurement of the resistance of the thermo-resistor has to be modified compared to the case when the *TCR* is constant in the entire operating temperature range. The resistance of polysilicon resistors as a function of temperature, *T* is represented in equation (3-2).

$$R = R_0(1 + \alpha(T - T_0) + \beta(T - T_0)^2) \quad , \tag{3-2}$$

where R_0 is the resistance of the thermo-resistor measured at temperature T_0.

The temperature of the resistor is determined explicitly from (3-2) as in (3-3).

$$T = T_0 + \frac{-\alpha - \sqrt{\alpha^2 + 4\beta\left(\frac{R}{R_0} - 1\right)}}{2\beta} \tag{3-3}$$

The observed behavior of polysilicon allows formulating the first guidelines for the design of thermal sensors containing polysilicon resistors.

The operating temperature of the MHP should not exceed ~150-200°C. At higher temperatures, a decrease of the *TCR* value reduces the sensor's sensitivity. If the operating ambient temperature reaches 60-80°C, the overheating temperature of the MHP should not exceed ~100°C.

The layout of the MHP must be designed such that to exclude or minimize the size of hot spots on its surface as much as possible. Segments of the polysilicon resistor located in these hot spots have a lower *TCR* which reduces the sensitivity of the sensor.

Reasonably low and moderate operating temperatures are also beneficial to reduce the thermal stress of polysilicon resistors and improve its long term stability.

The calculation of the MHP temperature must be done based on the equation (3-3). Ignoring the temperature dependence of *TCR* may result in an underestimation of an actual temperature which may reach up to 10°C and more at overheating temperatures of around 60°C which was found experimentally.

3.2 Structure of the MHP

The MHP comprises of two electrically isolated functional elements: Heater, R_H and thermo-resistor, *Rs*. The MHP circuit consists of four resistors shown on Fig. 3-10.

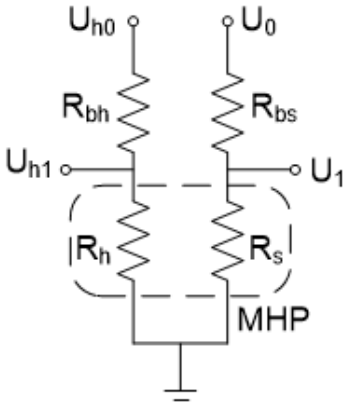

Fig. 3-10: Simple circuit of the MHP containing the 4 resistors

The heater is made from a Phosphorous-doped polysilicon with a resistance of 1.5kΩ (option 1) and 4kΩ (option 2). The thermo-resistor used as a temperature sensing element is fabricated from two types of polysilicon; one with resistance of 27kΩ (poly_A), the other one with 100kΩ (poly_B). The two resistors are placed on a suspended SiO_2 membrane with an area of about $0.02mm^2$.

The depth of the cavity beneath the MHP is about 90μm which determines the distance to the first heat sink. A silicon top cap bonded to the chip with the MHP provides a second heat sink at a distance of 70μm from the MHP.

The MEMS structure was fabricated using standard 1μm CMOS process with few post-processing steps such as deep KOH etching of Si from the front side of the wafer and subsequent wafer bonding.

A similar structure of the MHP with an electrically split resistive heater and temperature sensing element was designed for standard polyMUMPS process and is presented in Fig. 3-11. The heater and the temperature-sensitive resistor are serpentine structures made from polysilicon and suspended approximately 3μm over the surface of the wafer and attached to the anchors made from SiO_2 material. The anchors act as frames to support the entire MHP structure. Metal layers are served as electrode connections which bridge both the heater and the temperature sensor together.

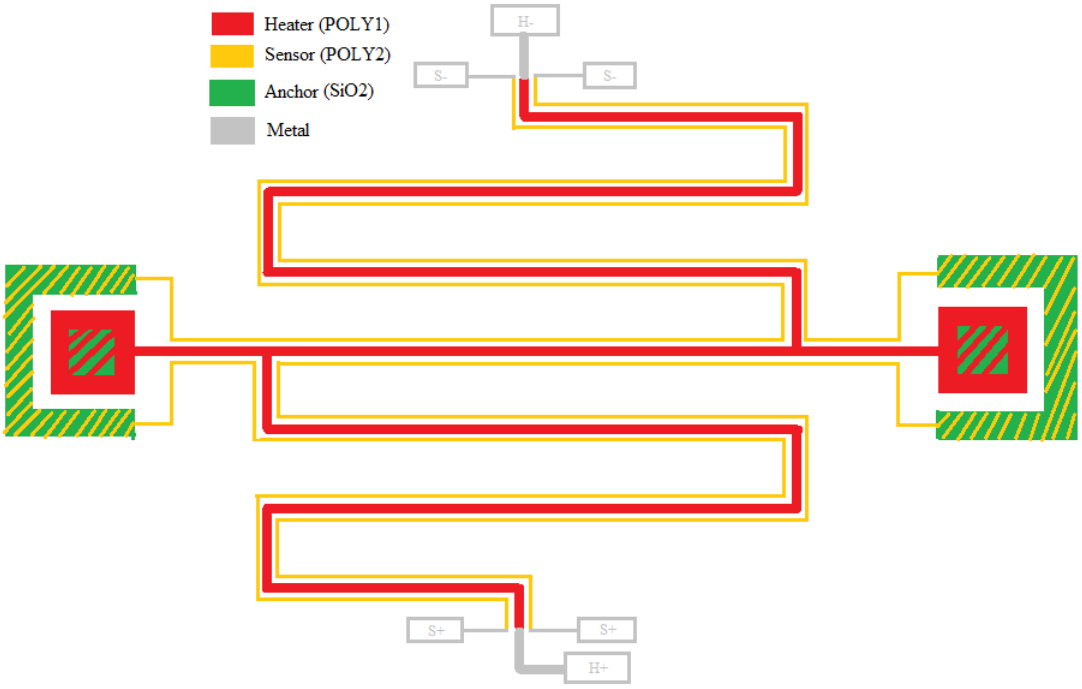

Fig. 3-11: Schematic structure of the MHP using polyMUMPS process.

The heater meander runs parallel to the thermo-resistor segments. The heating of the structure is reached by applying an excitation voltage to the heater terminals [32]. Heat transfer through the gas gap between the heater and the sensing element causes an overheating of the sensing thermo-resistor [32, 33, 34].

The structure is designed in Cadence Virtuoso with polyMUMPs process and will be presented in Chapter 6 in more detail.

3.3 Operating Mode of the MHP

The operating principle of the MHP consists of applying excitation voltage pulses on the heater (U_{h0}) and measuring the output voltage on the temperature sensor (U_1) (refer to Fig. 3-10). A constant voltage $U_0 = 5V$ is applied to the sensor divider.

3.3.1 Equations of Molecular Interactions

Overheating temperature, rate of overheating, temperature gradients, heat dissipation and overheating rate are the most informative parameters of the thermal sensor depending on thermo-physical properties of surrounding gas which in turn depend on chemical composition and gas concentration. Conservation of energy law dictates that the amount of energy entering the system must be equal to the amount of energy exiting the system. The energy equilibrium is shown in (3-4) below. Table 2 presents the description of the used parameters.

Table 2: Description of the parameters

Parameter	Description
m, kg	Mass of the MHP
c, J/kg*K	Specific heat of the MHP material
T_0, K	Ambient temperature
T, K	Temperature of the MHP
σ, W/um*K	Thermal conductivity of gas
S, um^2	Area of the MHP
l, um	Equivalent distance from the membrane to the heat sink [12]
P, W	Dissipated power of the MHP

$$Q = P\Delta t = mc\Delta T + \frac{\sigma S}{l} T\Delta t \qquad (3\text{-}4)$$

Analyzing (3-4), the first term on the right-hand side of the equation corresponds to the dissipated heat in the sensor as work exited; the second term on the right-hand side of the equation corresponds to heat loss through gradient fluxes of the MHP. Dividing equation (3-4) by the incremental time, Δt equation (3-5) is obtained.

$$P = mc\frac{dT}{dt} + \frac{\sigma S}{l}T \tag{3-5}$$

In the stationary case, when dT/dt = 0, the relationship in (3-6) is obtained.

$$P = \frac{\sigma S}{l}T \tag{3-6}$$

HLC is proportional to the thermal conductivity of the gas, to the area of the MHP and inversely proportional to the equivalent distance from the MHP's membrane to its heat sink [12].

This confirms our statement discussed in section 2.2. At low pressures, the gas is sparse of molecules meaning less molecules would interact with the MHP thus trapping the heat. In this case, the amount of heat dissipated in the environment is little while the overheating temperature of the device is large. At high pressures, the opposite effect occurs. There are many gas molecules present in the environment forcing them to trap heat from the MHP. Heat loss rises while the overheating temperature is meager.

Fig. 3-12a presents the overheating temperature for three different thermal conductivities of gas by solving the differential equation in (3-5).

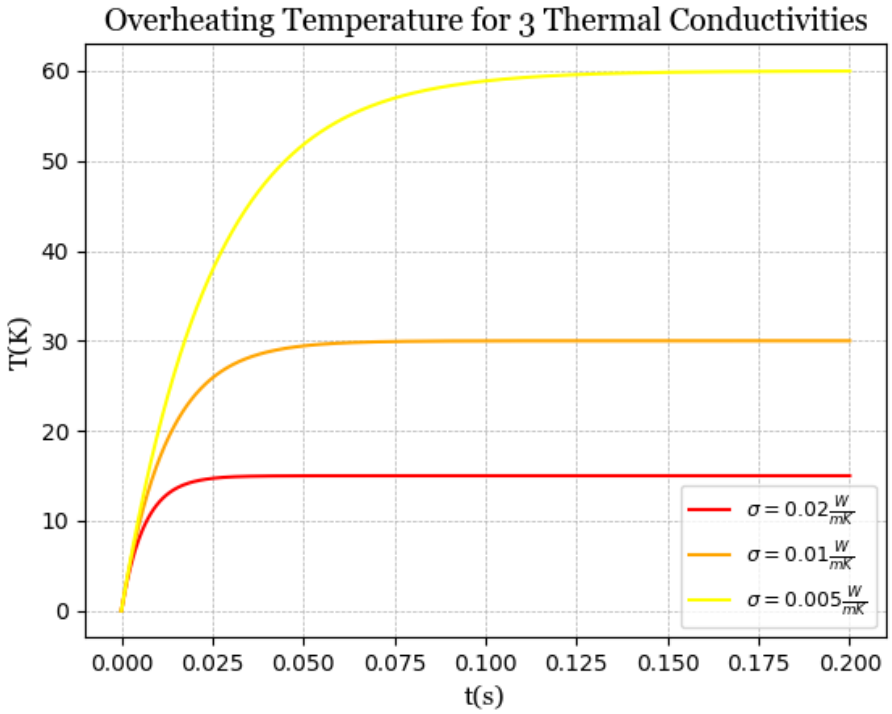

Fig. 3-12a: Overheating temperatures for 3 various thermal conductivities

It is observed that for larger thermal conductivities, overheating occurs at lower temperatures and the plateaus are reached in smaller time. The recording of the sensor's parameters such as *HLC*, *Rs*, R_H, *dT*, can be accomplished at faster intervals if operated at higher thermal conductivities.

3.3.2 Equations of the Sensing Element

In order to determine the gas pressure or the thermal conductivity of the gaseous mixture, the heat loss coefficient, *HLC* of the MHP is measured. *HLC* is the ratio between dissipated power P_{diss} and the overheating temperature, *dT* as determined. Referring to Fig. 3-10, the power dissipated on the heater is presented in equation (3-7).

$$P_{diss} = \frac{U_{h1}(U_{h0} - U_{h1})}{R_{bh}} \qquad (3\text{-}7)$$

The resistance, R_s is calculated and presented in (3-8).

$$R_s = \frac{R_{bs}}{\frac{U_0}{U_1} - 1} \tag{3-8}$$

To measure the overheating temperature, dT, the resistance of the thermo-resistor, R_s is measured at zero dissipated power (R_{s1}) and at power, P_{diss} (R_{s2}). The overheating temperature is calculated in two steps. First, the ambient temperature T_{amb} is calculated at zero dissipated power, then temperature T_2 is calculated at power, P_{diss}. This is presented in equations (3-9), and (3-10), respectively.

$$T_{amb} = T_0 + \frac{-\alpha - \sqrt{\alpha^2 + 4\beta\left(\frac{R_{s1}}{R_{s0}} - 1\right)}}{2\beta} \tag{3-9}$$

$$T_2 = T_0 + \frac{-\alpha - \sqrt{\alpha^2 + 4\beta\left(\frac{R_{s2}}{R_{s0}} - 1\right)}}{2\beta} \tag{3-10}$$

The overheating temperature, dT is determined as illustrated in equation (3-11).

$$dT = T_2 - T_{amb} \tag{3-11}$$

Note that the ambient temperature, T_{amb} may be fundamentally different from room temperature (T_0 = 22°C) defined during the calibration of polysilicon resistors (refer to (3-1) and (3-2)).

It is important to take into consideration that a possible drift of resistance, R_s caused by its instability does not affect measurements of the overheating temperature which depends on a relative increment of the resistance caused by the power dissipated on the MHP. Analogously, the dissipated power is measured accurately and independently on the possible drift of resistance, R_h. In both cases, the stability of the external ballast resistors R_{bs} and R_{bh} is crucial.

Advanced electronic circuitry providing better signal-to-noise ratio, *SNR* is shown on Fig. 3-13. The temperature sensitive resistor, R_s is connected in a Wheatstone bridge type configuration with a ballast resistor, R_{bs} and two permanent resistors, R.

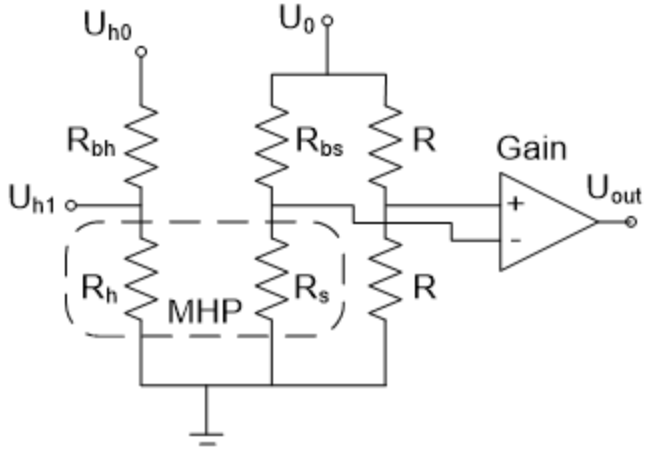

Fig. 3-13: Modified circuit of the sensing element

The output of the instrumentation amplifier is shown in equation (3-12).

$$U_{out} = \frac{U_0}{2}\left\{1 + Gain\left(1 - \frac{2R_s}{R_s+R_{bs}}\right)\right\} \qquad (3\text{-}12)$$

The resistance, R_s is determined from (3-12) and is presented in (3-13).

$$R_s = R_{bs}\frac{U_0(Gain+1)-2U_{out}}{U_0(Gain-1)+2U_{out}} \qquad (3\text{-}13)$$

3.4 Signal Waveforms of the Heater and Sensor

The signal of the sensor was determined after applying a pulse wave on the heater part (U_{h0}) and recording the output of the sensor (U_1) as was shown on Fig. 3-10 above.

A sample chip containing three separate MHPs was chosen to study the waveforms of the heater and sensor signals.

Fig. 3-14 presents a pinout schematic of the following chip. The numbers correspond to the respective pins. Pin 7 is grounded. H1, S1 correspond to the ballast resistors of the heater and the sensor of MHP1, correspondingly.

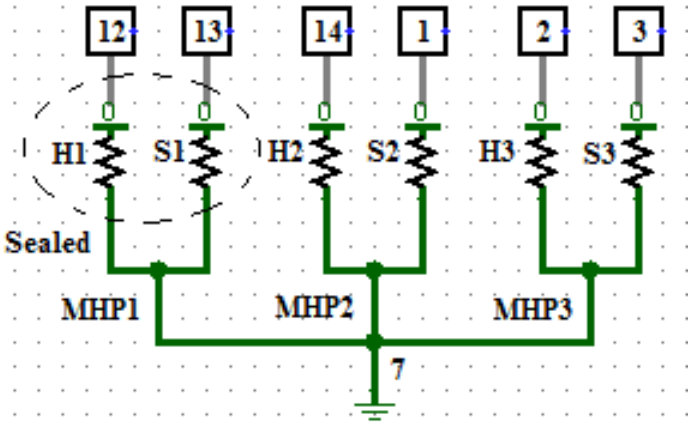

Fig. 3-14: Pinout schematic of the 3 MHPs

On the above figure, signal waveforms were obtained for the sealed MHP.

As was discussed in 3.3, a pulse signal was applied to U_{h0} and the output signal was recorded at U_1. Fig. 3-15 demonstrates the two resulting signals. The frequency of the function generator was set to 200Hz to obtain a decent view of symmetric warming and cooling of the sensor part of the MHP.

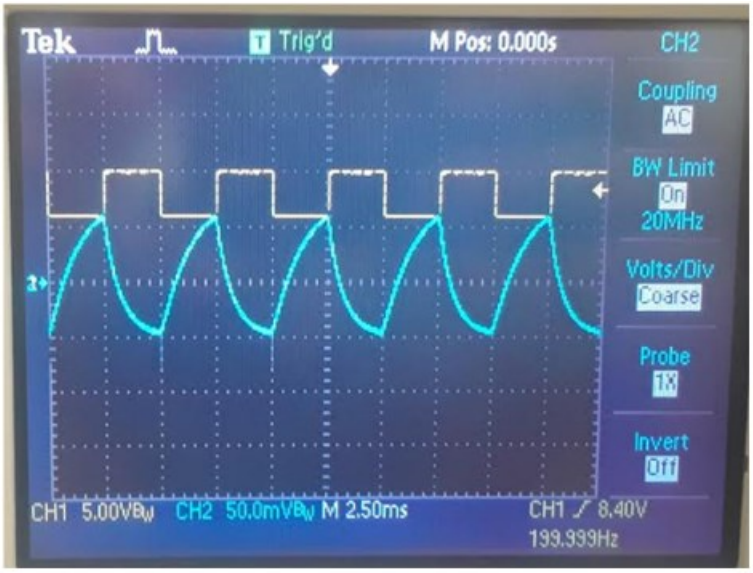

Fig. 3-15: Input signal (in yellow) with f = 200Hz. Output signal (in blue) with symmetric rising, falling edges. Plateaus are not observed.

In Fig. 3-15, the plateaus of the signal are not fully observed due to a short duration of the heating pulses. An increase of pulse duration results in the MHP heating waveforms with definite plateau similar to waveforms simulated in Fig. 3-12a.The results are presented in Fig. 3-16a,b.

In Figs. 3-16a, 3-16b, waveforms of the sensor voltage U_1 (see Fig. 3-10) and heaters outputs U_{h1} are shown respectively.

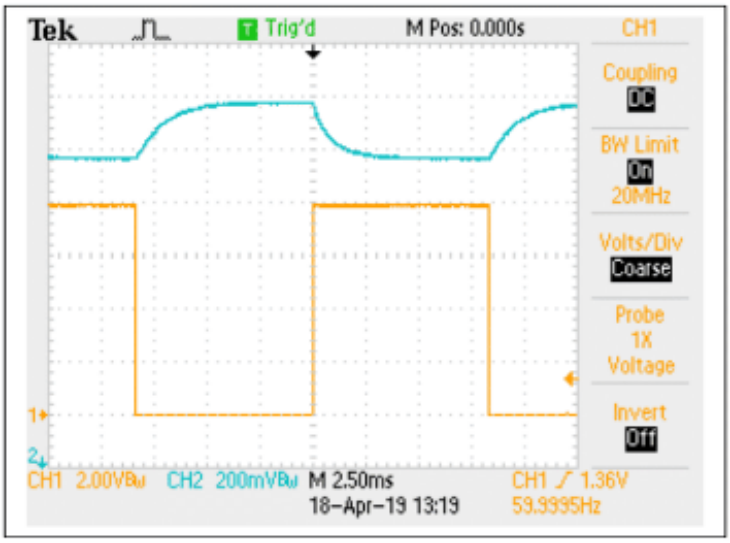

Fig. 3-16a: Input signal (in yellow) with f ~ 70Hz, V_{DC} = 2V. Output sensor signal (in blue) with symmetric rising and falling edges along with plateaus.

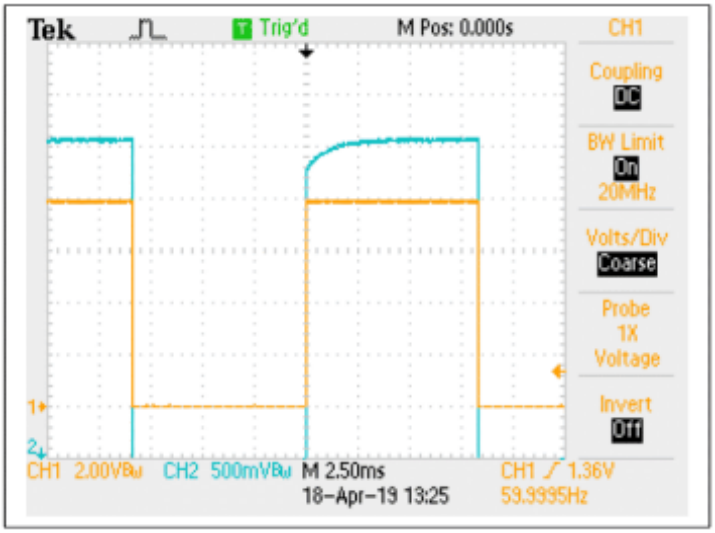

Fig. 3-16b: Output heater signal (in blue) with observed plateaus at f ~ 70Hz.

In the aforementioned explanation, the operating principle of the thermal sensor is based on a voltage drop measurement across the heater and the sensor at zero heating and at dissipated power P_{diss}. A second measurement should be performed in the condition when the overheating temperature reaches a plateau. A proper choice of the required settling time after the start of the MHP heating is important especially if heat losses to the ambient vary significantly during measurement sessions. For instance, the heating time for the MHP may vary from 5 to 10ms at atmospheric pressure to about 100-150ms at high vacuum.

An interesting observation is reported at the rising edge of the input signal. In Fig. 3-16a, the output of the sensor signal gradually decreases, whereas the output of the heater signal gradually increases. This remark can be explained by a negative *TCR* of the temperature sensor (-1300ppm/K) and a positive *TCR* of the heater (850ppm/K).

3.5 MHP's Resistance and Overheating Temperature vs Power

Another analysis has been performed to study the relationships between the temperature sensor, heater resistances, R_S, R_H, dissipated power and *HLC* in static mode. For this purpose, the circuit was tested with applying a DC voltage.

In Figs. 3-17a and 3-17b, the graphs of the sensor and the heater resistances versus the dissipated power are presented below. To avoid any ambiguities, it should be noted that the power is dissipated across the sensor and the heater.

Values were recorded from 0V to 10V with a step of 0.5V first for the sensor and then for the heater. The following voltages which are designated by U_0 was applied on pin 13 shown on Fig. 3-14.

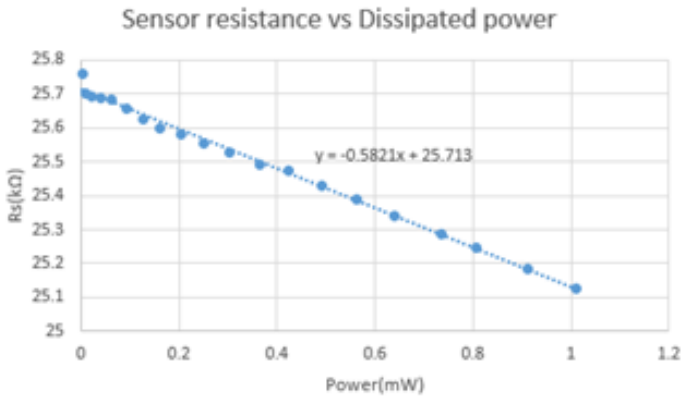

Fig. 3-17a: Sensor resistance as a function of dissipated power. R_{S0} = 25.713kΩ

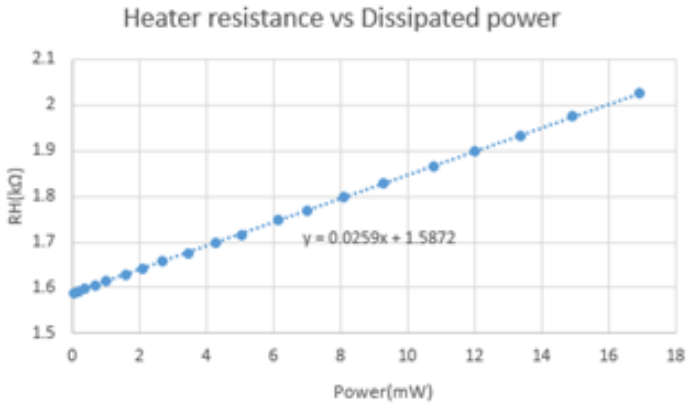

Fig. 3-17b: Heater resistance as a function of dissipated power. R_{h0} = 1.5872kΩ

As should be expected, R_S should decrease with rising dissipated power due to its negative *TCR* value (α_s = -1300ppm/K). For R_H, the opposite effect occurs due to a positive *TCR* value, (α_h = 850ppm/K).

In Figs. 3-18a and 3-18b, overheating temperatures (measured in K) as a function of dissipated power (mW) are reported for the sensor and the heater as U_0 is increased from 0V to 10V. Both graphs exhibit rising temperature behaviour with the heater part reaching much higher temperature values.

It should be noted that at U_0 = 10V, the power dissipated on the sensor is approximately 1mW compared with nearly 17mW dissipated on the heater. Moreover, the overheating temperature at 10V increased by 18K on the sensor part compared with almost 350K on the heater.

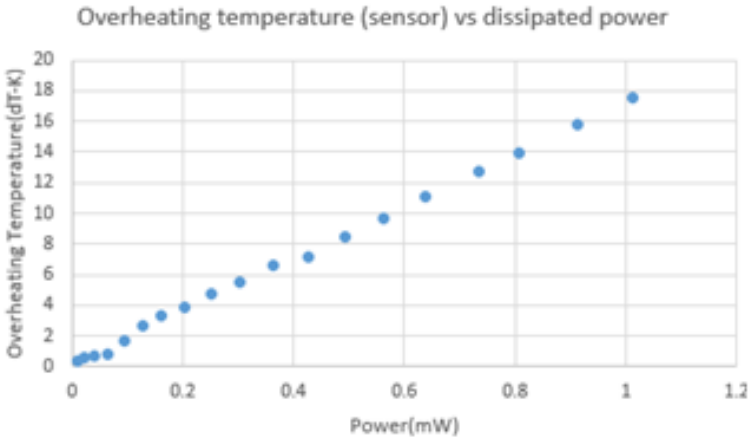

Fig. 3-18a: Overheating temperature as a function of power dissipated on the temperature sensor

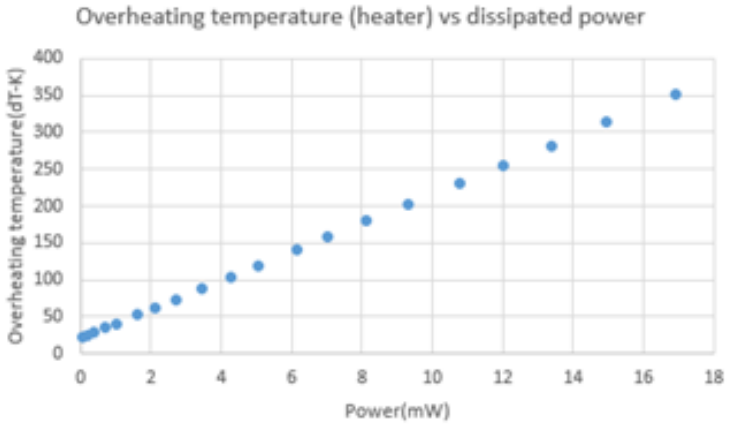

Fig. 3-18b: Overheating temperature as a function of power dissipated on the heater

Resistance values for the heater and the sensor have been selected in order to reach significant overheating temperatures with comparatively low excitation voltages, compatible with 5V

electronics and to cause negligible self-heating of the sensor when a constant voltage is applied to the measurement electronic scheme.

CHAPTER 4: SIMULATION OF TEMPERATURE DISTRIBUTION OF THE MHP

4.1 Governing Equations

Heat distribution across the MHP is governed by the famous Heat Equation presented in (4-14).

$$\sigma c_p \frac{\partial T}{\partial t} - \nabla(k\nabla T) = Q \tag{4-14}$$

The parameters in (4-14) are displayed in Table 3.

Table 3: Description of Parameters of the Heat Equation

Parameter	Description
σ , kg/m^3	Density of the Material
c_p, J/kg*K	Specific Heat Capacity
k, W/K	Thermal Conductivity of Gas
Q, W	Power supplied to the MHP
T, K	Overheating Temperature of the MHP

An idealized model used to present heat conduction is depicted on Fig. 4-19.

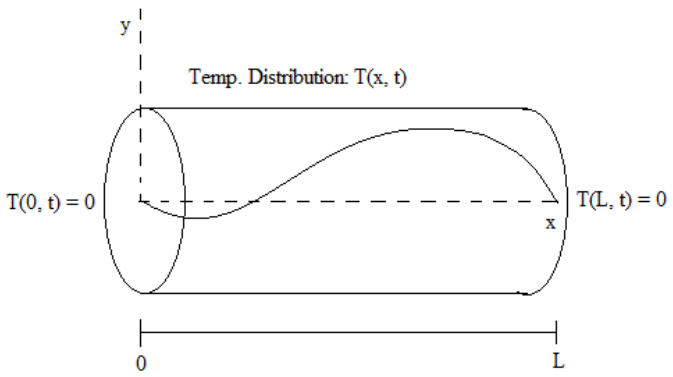

Fig. 4-19: Idealized heat distribution in a rod with two heat sinks at the edges

A similar approach is applied for the MHP design with two heat sinks at the boundaries of the device. The breakdown of the heat equation will be analyzed for the MHP. The common method to solve Equation (4-14) is to assume that the TCR of the heater is uniform across the entire region of the device. Since the time dependence of the heat distribution is of no importance to the set target, (4-14) can be elegantly decomposed into differential equation (4-15). (4-15) corresponds to a static case. Heat loss into the ambient gas is neglected which is comparable to the condition at high vacuum. Heating of the MHP is provided by the resistive heater.

$$\frac{\partial^2 T}{\partial x^2} = -K(1 + \alpha T),\ K = \frac{\rho I^2}{\lambda S} \qquad (4\text{-}15)$$

The following constants of (4-15) are described in Table 4.

Table 4: Description of the constants of Equation (4-15)

Constant	Description	Value/Units
ρ	Heater resistivity	1.7 Ω/um
I	Current flowing through poly-Si	0.5mA
λ	Effective thermal conductivity of the structure	W/um*K
S	Cross sectional area of the structure	λ *S = 3.4*10^{-4} W*um^2/um*K
α	TCR of the Heater	850ppm/K

The boundary conditions for (4-15) are as follows: T(-L/2) = T(L/2) = 0 where L is the length of the MHP.

The above differential equation can be re-arranged in the following manner. This is shown in (4-16).

$$\frac{\partial^2 T}{\partial x^2} + K\alpha T = -K \tag{4-16}$$

Equation (4-16) is further divided into homogeneous and particular equations. The homogeneous and particular equations are presented in (4-17) and (4-18), respectively.

$$\frac{\partial^2 T_h}{\partial x^2} + K\alpha T_h = 0 \tag{4-17}$$

$$K\alpha T_p = -K \tag{4-18}$$

Solution to (4-17) is simply a combination of sine and cosine. The homogeneous solution is shown in (4-19); particular solution is shown in (4-20).

$$T_h(x) = C_1 cos\left(\sqrt{K\alpha}x\right) + C_2 sin\left(\sqrt{K\alpha}x\right) \quad (4\text{-}19)$$

$$T_p(x) = -\frac{1}{\alpha} \quad (4\text{-}20)$$

The general solution is found by adding the homogeneous and the particular solutions. This is shown in (4-21).

$$T(x) = C_1 cos\left(\sqrt{K\alpha}x\right) + C_2 sin\left(\sqrt{K\alpha}x\right) - \frac{1}{\alpha} \quad (4\text{-}21)$$

Coefficients C_1, C_2, are found from the boundary conditions. The equation for the overheating temperature profile across the MHP is presented in (4-22).

$$T(x) = \frac{1}{\alpha}\left(\frac{cos\left(\sqrt{K\alpha}x\right)}{cos\left(\sqrt{K\alpha}\frac{L}{2}\right)} - 1\right) \quad (4\text{-}22)$$

Equation (4-22) can be further simplified when $\alpha \rightarrow 0$. The parabolic equation can be determined from this. Using Taylor's Series, the cosine terms are further decomposed in the following manner.

- $cos\left(\sqrt{K\alpha}x\right) = 1 - \frac{1}{2!}\left(\sqrt{K\alpha}x\right)^2 + \frac{1}{4!}\left(\sqrt{K\alpha}x\right)^4 - \frac{1}{6!}\left(\sqrt{K\alpha}x\right)^6 + \cdots$
- $cos\left(\frac{\sqrt{K\alpha}L}{2}\right) = 1 - \frac{1}{2!}\left(\frac{\sqrt{K\alpha}L}{2}\right)^2 + \frac{1}{4!}\left(\frac{\sqrt{K\alpha}L}{2}\right)^4 - \frac{1}{6!}\left(\frac{\sqrt{K\alpha}L}{2}\right)^6 + \cdots$

Selecting the first two terms of both cosines, *T(x)* is written in the following manner in (4-23).

$$T(x) = \frac{1}{\alpha}\left\{\frac{1-\frac{1}{2}\left(\sqrt{K\alpha}x\right)^2}{1-\frac{1}{2}\left(\frac{\sqrt{K\alpha}L}{2}\right)^2} - 1\right\} \quad (4\text{-}23)$$

Simplifying (4-23) further, the final temperature equation is presented in (4-24).

$$T(x) = \frac{-\frac{1}{2}Kx^2 + \frac{1}{8}KL^2}{1-\frac{1}{8}KL^2\alpha} \quad (4\text{-}24)$$

Analyzing (4-24), one should anticipate a parabolic heat distribution of the MHP.

4.2 Thermal Analysis of the MHP

Using Python programming language, thermal analysis of the temperature distribution was studied and analyzed. Fig. 3-11 will be used to study the physics of the model considered in Heat Equation in (4-15).

The temperature distribution of the MHP depends on the heat dissipated along the horizontal segments (along the y-axis in Fig. 3-11) and vertical segments (along the x-axis in Fig. 3-11).

Numerical analysis was done for the structure with the following parameters. The total length of all horizontal sides was taken to be 100µm and the current flowing through the heater of the MHP was chosen to be 1mA. The two heat sinks are located at the boundaries at room temperature (T ~ 293K).

Fig. 4-20 presents analytical and numerical solutions of the temperature distribution of the MHP along all horizontal sides.

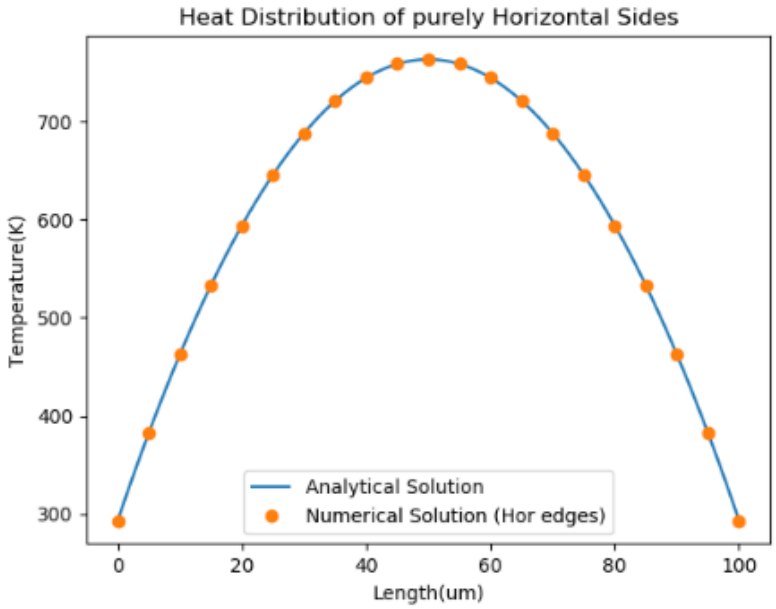

Fig. 4-20: Analytical and numerical solutions of the temperature distribution across horizontal edges of the MHP

Observing Fig. 4-20, the numerical solution is correct since the discrete points matched the analytical curve.

Afterwards vertical edge solutions are shown in Fig. 4-21. The vertical edges are subdivided into the following interval array: *x_discrete = [0, 20, 35, 50, 65, 80, 100]um* from one of the heat sinks of the MHP. An important physical factor to take into consideration is that there will be a temperature gradient, *dT/dx* resulting from each vertical edge.

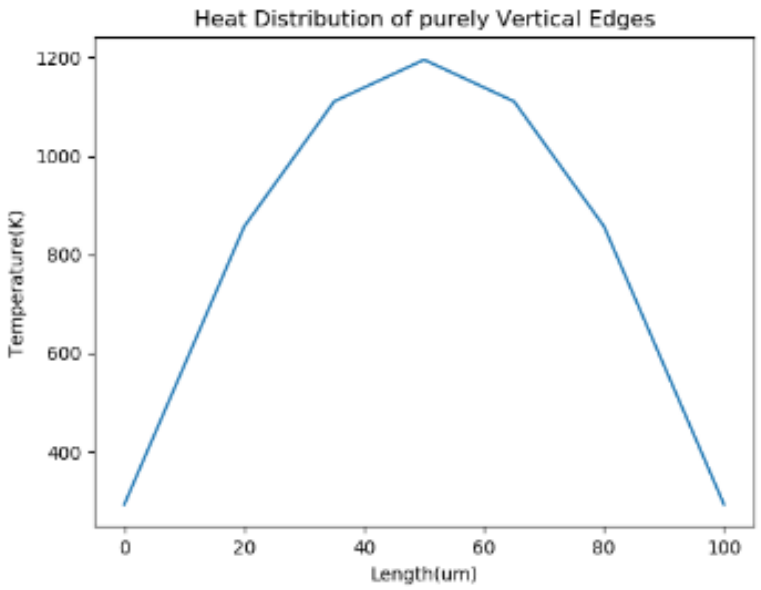

Fig. 4-21: Heat distribution of the vertical edges of the MHP

Finally, Fig. 4-22 presents the total heat distribution of the MHP by adding the heat distribution of horizontal and vertical edges.

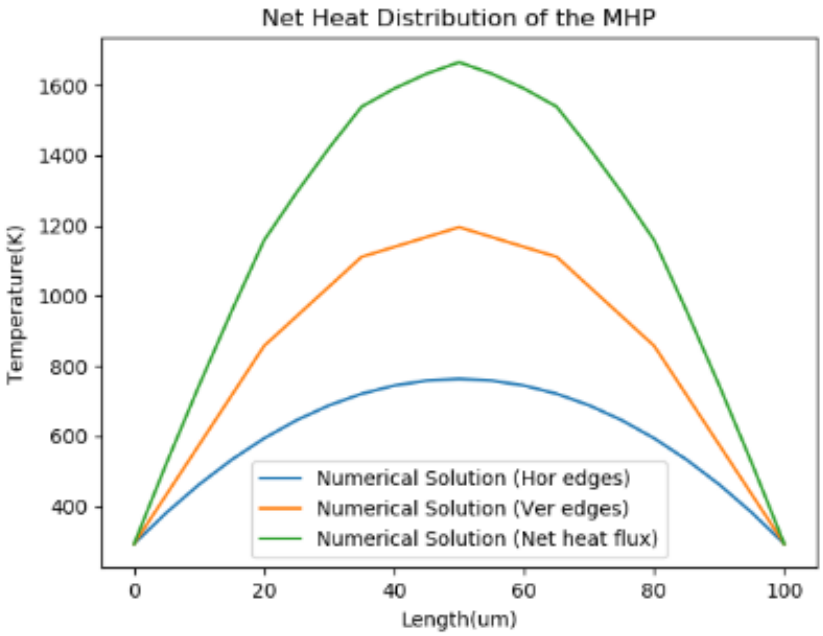

Fig. 4-22: Net heat distribution of the MHP (in green)

The numerical solution for the net heat distribution is obtained with a maximum temperature reaching 1665K at the center of the MHP at a current of 1mA. For the MHP to properly operate as a gas detecting sensor with optimal sensitivity, it is desirable to have temperature uniformity across the majority of the heater [35]. For this reason, a very thin Al slab of about 0.1um will be considered which will be placed directly on top of the MHP. Al is selected for this test since it is CMOS compatible and part of standard process technology. The melting temperature of Al is around 687°C or 960K which would cause the slab to melt at 1mA current and damage the device. However, for the coming experiments, the device will operate at much lower input power.

To avoid confusion, it should be noted that a heating current of 1mA was chosen arbitrarily. Actual operating temperatures were significantly lower and never exceeded 200°C. The following current of 1mA was simply chosen to demonstrate a theoretical representation of how the MHP should overheat. Not only will the slab lower the maximum temperature of the heater, but it will also distribute the temperature uniformly across the MHP. These results will be presented in section 4.4.

4.3 Simulation with COMSOL. Comparison with Python Results. Temperature Distribution across the MHP.

To further confirm the validity of the results obtained in Python, COMSOL Multiphysics was used to design and simulate the MHP under similar conditions.

A quantitative analysis of the temperature distribution across the MHP is presented below. Ideally, the entire MHP should be at constant temperature to optimize its sensitivity and the *TCR* of the heater resistor as much as possible. However, it is impossible to accomplish the following task because both ends of the MHP act as heat sinks for this device.

A simplified model of the MHP is presented in the figures below. Fig. 4-23a shows the MHP with the SiO_2 layer highlighted in blue; Fig. 4-23b shows the MHP with the poly-Si layer highlighted in blue.

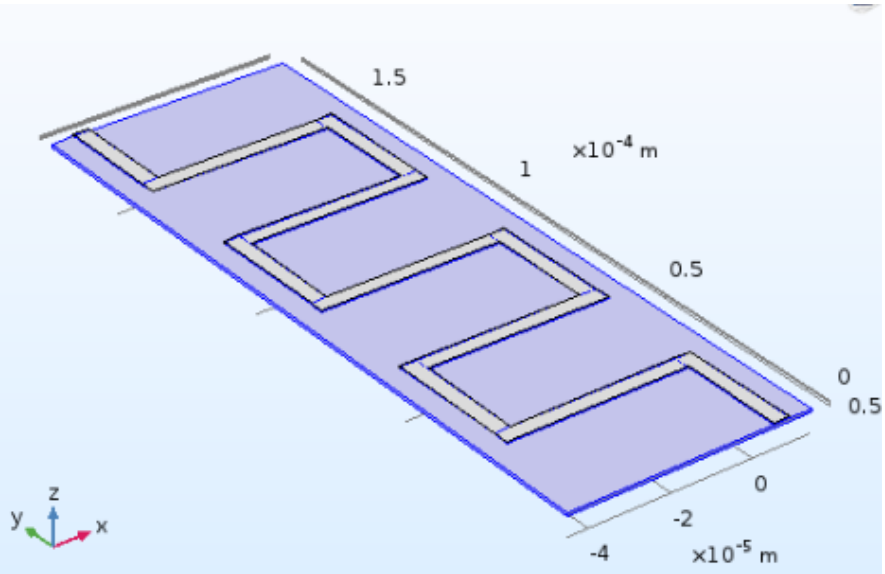

Fig. 4-23a: MHP with SiO_2 highlighted in blue

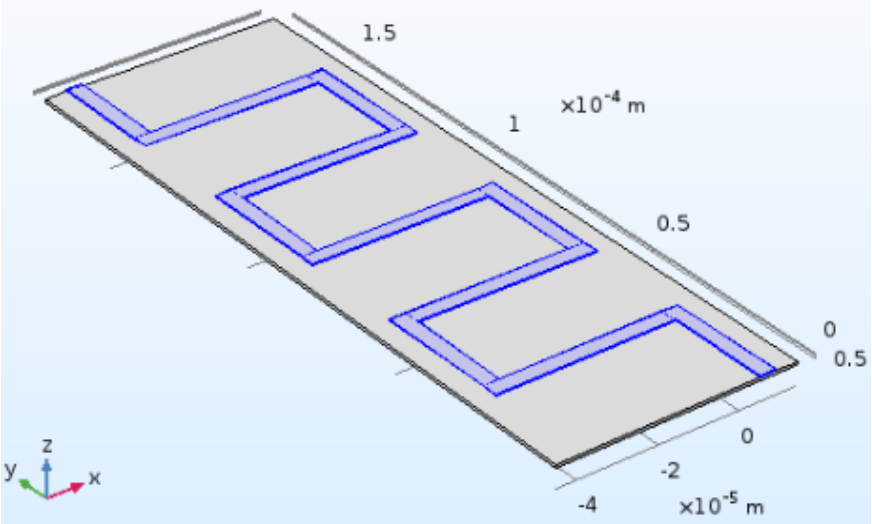

Fig. 4-23b: MHP with poly-Si highlighted in blue

The thicknesses of both layers are shown in Fig. 4-23c.

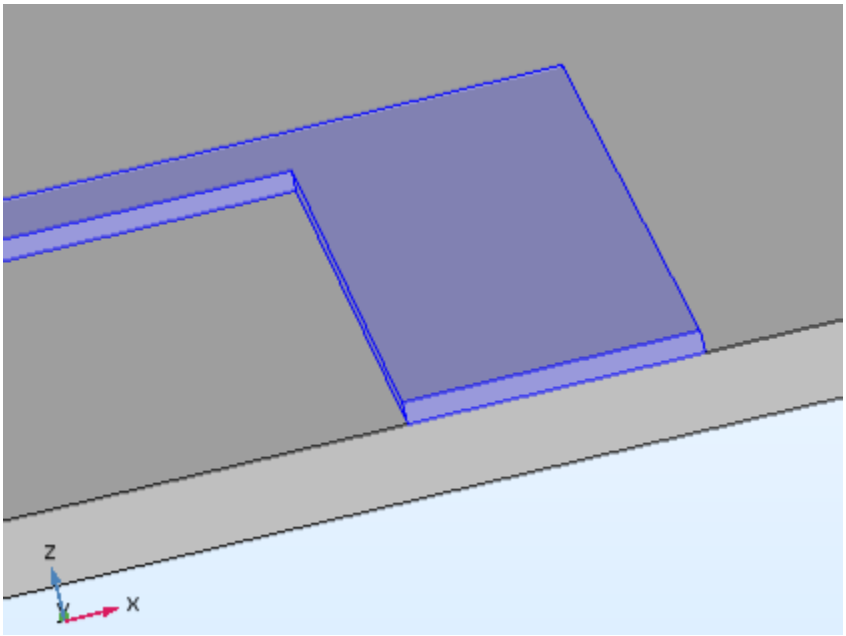

Fig. 4-23c: Thickness of SiO_2 layer (1um); thickness of poly-Si layer (0.3um)

The poly-Si layer acts as a heater resistor for the MHP. The following thicknesses of the layers were chosen to be 1um for SiO_2 layer; 0.3um for poly-Si layer. Thermal conductivities of SiO_2 and poly-Si layers are 1.4W/mK and 30W/mK, respectively.

The calculations are done in assumption that the heat transfer to ambient gas is negligible. This corresponds to high vacuum conditions. An arbitrary input current of 1mA was chosen to flow through the poly-Si layer.

Heat sinks were chosen at the two boundary ends of both SiO_2 and poly-Si layers. After simulating the structure, the temperature distribution of the MHP is obtained. In Fig. 4-24a, a visual representation is observed; in Fig. 4-24b, the temperature distribution as a function of the horizontal length is shown.

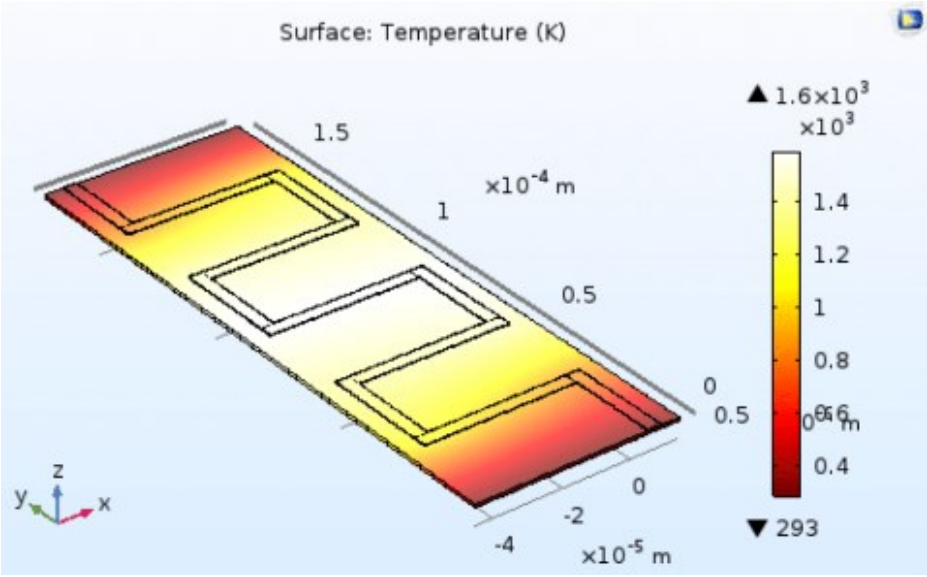

Fig. 4-24a: Visual representation of the MHP's temperature distribution

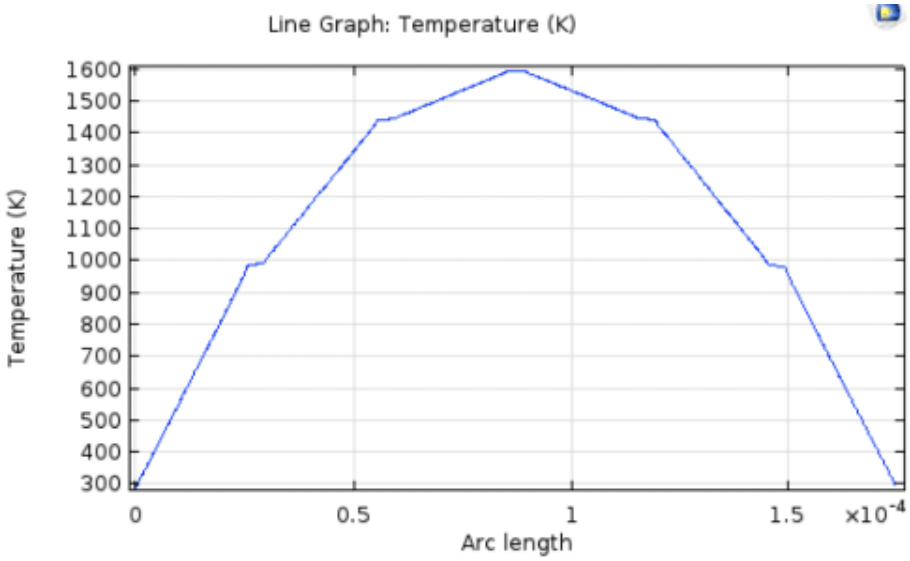

Fig. 4-24b: Graphical representation of the MHP's temperature distribution

As observed in Figs. 4-24a and 4-24b, a similar temperature distribution shape is obtained when analyzing the simulated results on Python. The maximum temperature attained using COMSOL simulation was 1594K (1321°C) in comparison with 1665K (1392°C) using Python. Despite the fact that both programs contain different convergence algorithms, the results are similar.

The temperature distribution across the MHP will be shown for two types of heater TCRs: a theoretically approximated constant value of 850ppm/K and an experimentally determined TCR value as a function of temperature obtained when the MHP was tested in a furnace. These simulations will be shown in subsections 4.3.1 and 4.3.2, respectively.

4.3.1 Constant TCR Case

In order to avoid splitting the net temperature profile along the horizontal and vertical edges of the MHP, a decent approximation would consist of stretching the heater serpentine in the horizontal direction. This would allow to neglect the temperature gradients along the discrete intervals of the MHP simultaneously keeping a similar temperature distribution across the entire length of the

MHP's heater. The total horizontal edge length would thus change from 100µm to 880µm with stretching.

The constant *TCR* case consists of directly solving (4-15). This equation can be directly solved analytically. Fig 4-25 presents the temperature distribution of the MHP with a constant *TCR* value of the heater. The MHP is shown with two heat sinks situated at -440µm and 440µm. The MHP was tested for an input current of 0.5mA flowing through the heater.

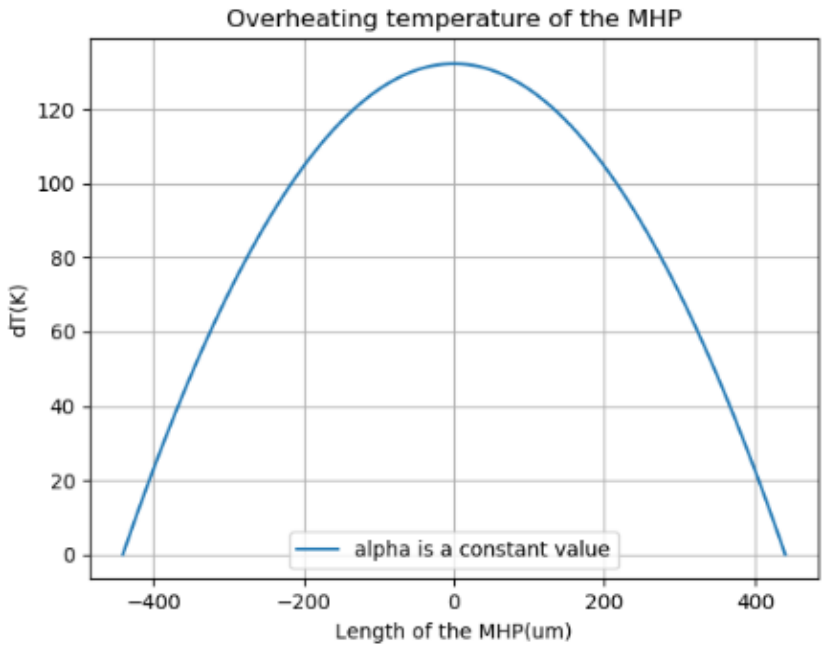

Fig. 4-25: Overheating temperature across the MHP length at I = 0.5mA. α(T) = 850ppm/K

As observed, the maximum overheating temperature is 132.12K at the center of the MHP for α(T) = 850ppm/K. A constant chosen *TCR* was an approximation for this problem. In reality, the poly-Si resistors used in the heater have a temperature dependent *TCR*.

4.3.2 Temperature-Dependent TCR case

Poly_Si resistors used in the heater were experimentally tested inside the furnace from -20°C to 250°C to find the dependence of *TCR* of the heater as a function of temperature. Functional

resistors of the MHP is the heater with a resistance of 4kΩ (P-doped). The dependence of *TCR* of the heater as a function of overheating temperature is presented in Fig. 4-26.

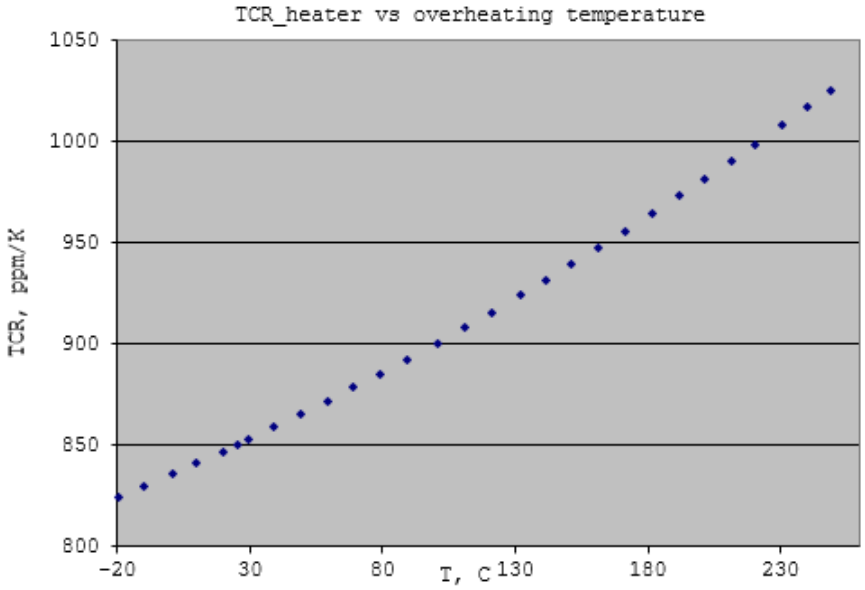

Fig. 4-26: *TCR* of the heater as a function of the overheating temperature of the MHP

The function that would linearize the set of raw data points in Fig. 4-26 was determined. The equation of TCR vs temperature (α(T) vs T) of the heater is presented in (4-25).

$$\alpha(T) = A + BT + CT^2 \tag{4-25}$$

In the above equation, the constants, A, B, C are the following:

- A = 847[ppm/K] = 847E-6[1/K]
- B = 0.602[ppm/K^2] = 0.602E-6[1/K^2]
- C = 0.00077[ppm/K^3] = 0.00077E-6[1/K^3]

Analyzing the curve, it is seen that when the overheating temperature changes from about 30°C to 130°C, the *TCR* of the poly-Si varies from approximately 850ppm/K to around 900ppm/K.

Replacing α in (4-15) by (4-25), the modified differential equation that needs to be solved will have the following form presented in (4-26).

$$\frac{\partial^2 T}{\partial x^2} = -K(1 + AT + BT^2 + CT^3), \text{ where } K = \frac{\rho I^2}{\lambda S} \qquad (4\text{-}26)$$

Equation (4-26) can only be solved numerically. Numerical simulation on Python was performed in order to solve it.

Fig. 4-27 demonstrates two temperature profiles across the MHP when the *TCR* is both a constant value and a function of temperature when a current of 0.5mA is flowing through the heater of the MHP.

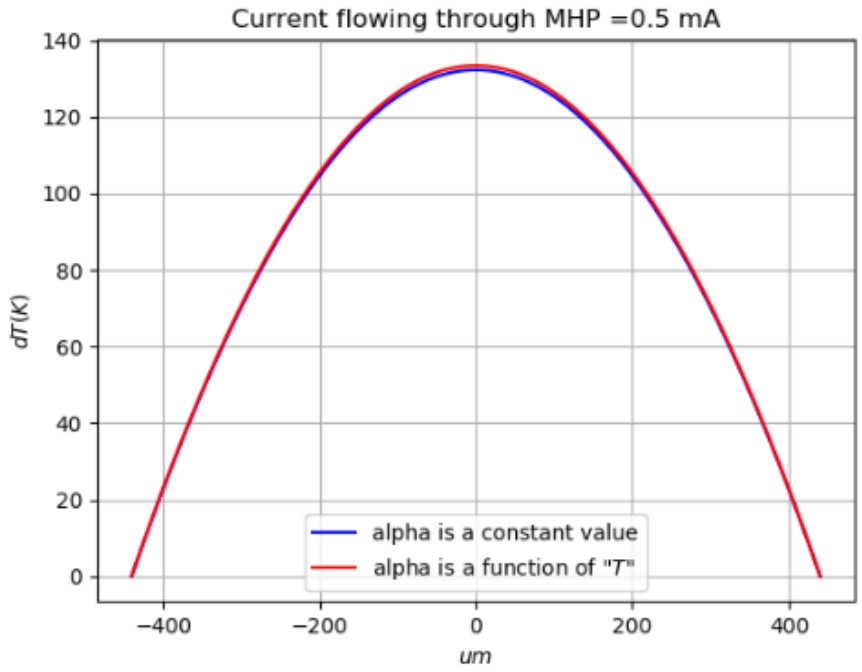

Fig. 4-27: Overheating temperature across the MHP for 2 different *TCR* values at I = 0.5mA.

As observed from Fig. 4-27, the temperature distribution in blue corresponds to a constant *TCR* value; the temperature distribution in red corresponds to a temperature-dependent *TCR* value. The two temperature profiles practically lie in unison. A slight variation occurs in the middle of the MHP. Fig. 4-28 presents the percent error in overheating temperatures between the theoretically chosen *TCR* value of 850ppm/K and an experimentally determined *TCR* behavior.

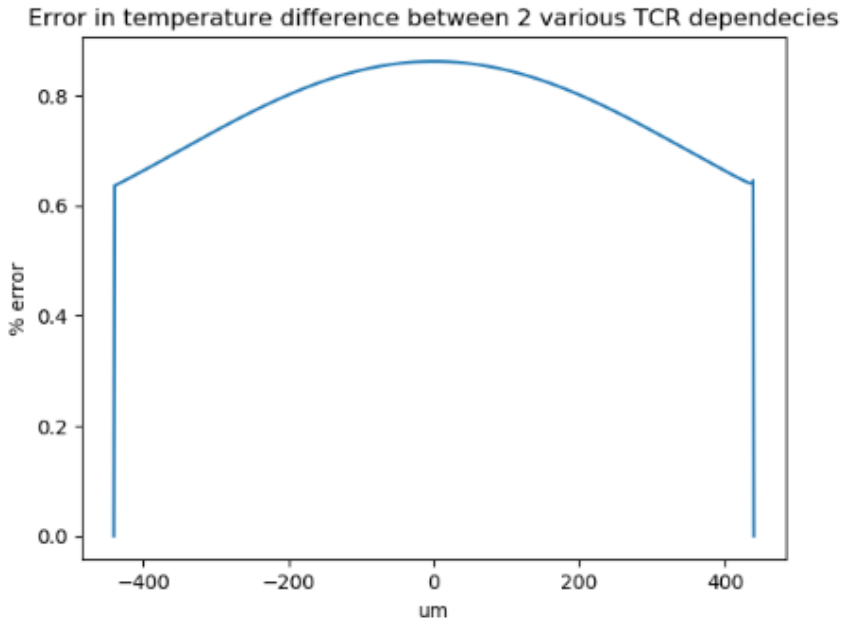

Fig. 4-28: % error between theoretical and experimental *TCR* dependencies

Analyzing Fig. 4-28 above, it is seen that the maximum error in both calculations is about 0.85%. Coefficients B and C in (4-25) do not contribute significantly to the shape of the overheating temperature of the MHP. Therefore, it is established that the *TCR* formula experimentally determined in (4-25) can be successfully approximated by a constant *TCR* value of 850ppm/K across the entire MHP.

4.3.3 Temperature Profiles for Various Currents

As described in Report 4.3.2, it is acceptable to approximate the TCR of the heater simply by (4-27).

$$\alpha(T) = 850\,\frac{ppm}{K} \tag{4-27}$$

The graphs depicted below show the dependence of the overheating temperature across the MHP for currents of 0.6mA (Fig. 4-29a), 0.7mA (Fig. 4-29b), 0.8mA (Fig. 4-29c) being applied to the MHP, respectively.

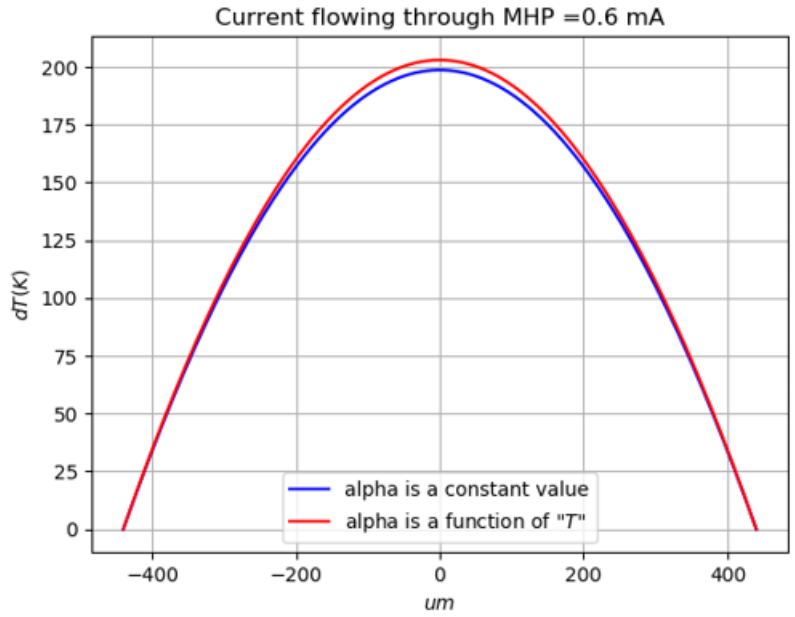

Fig. 4-29a: Overheating temperature across the MHP for 2 different TCR values at I = 0.6mA

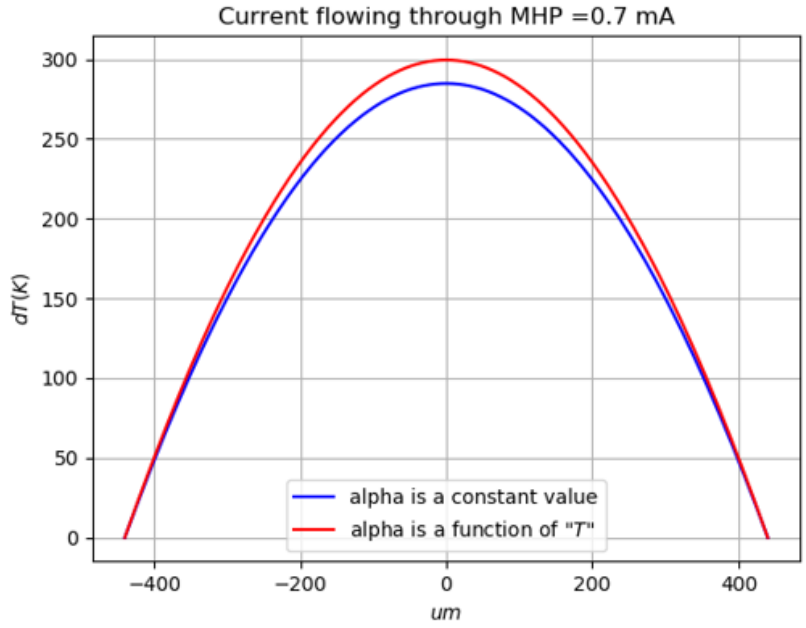

Fig. 4-29b: Overheating temperature across the MHP for 2 different TCR values at I = 0.7mA

Maximum % errors between theoretical and experimental TCR dependencies in Figs. 4-29a-c correspond to 1.82% for $I = 0.6mA$; 5% for $I = 0.7mA$; 12.77% for $I = 0.8mA$.

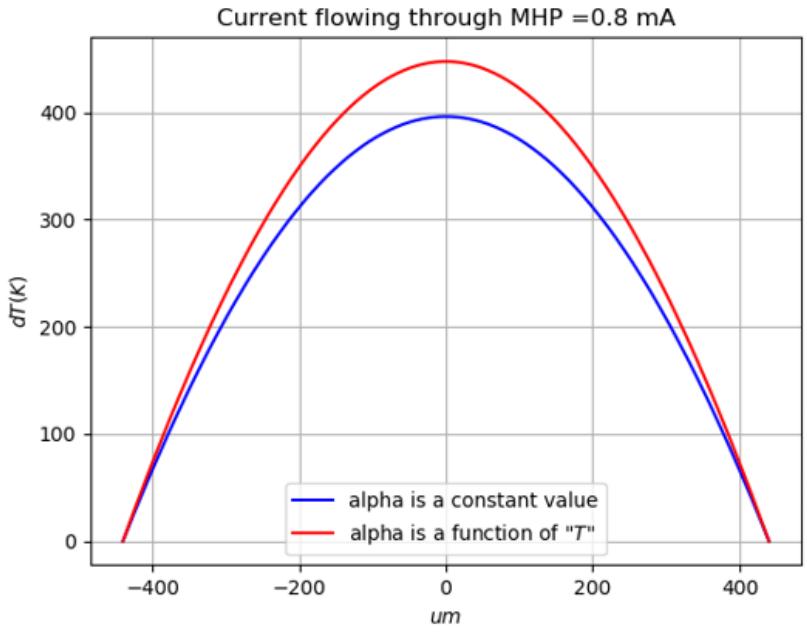

Fig. 4-29c: Overheating temperature across the MHP for 2 different TCR values at I = 0.8mA

Analyzing Figs 4-29a-c, as the current flowing through the MHP increases, the two overheating curves start to deviate from one another as the First-Order and the Second-Order coefficients, B and C contribute more to the overheating of the plate. Therefore, for currents in the range of ~0.8mA or larger, it is not possible to approximate the actual TCR function by (4-27) anymore. Fortunately, for the target of this project, large overheating temperatures of the MHP are not required. Input current of 0.5mA would suffice.

4.4 Improvement of Temperature Uniformity

To reduce the presence of hot spots across the MHP and to optimize the overheating temperature across the MHP, a piece of Al thin film is placed on top of the plate. Keeping in mind that the melting temperature of Al is about 960K (687°C), a current of 0.5mA is supplied to the device in order to maintain the maximum overheating temperature well below the critical value.

Fig. 4-30 shows two temperature profiles across the MHP containing an Al slab covering the majority of the MHP. The curve in blue shows a constant TCR value; the curve in red depicts a

temperature-dependent TCR across the device when a current of 0.5mA is flowing through the MHP's heater.

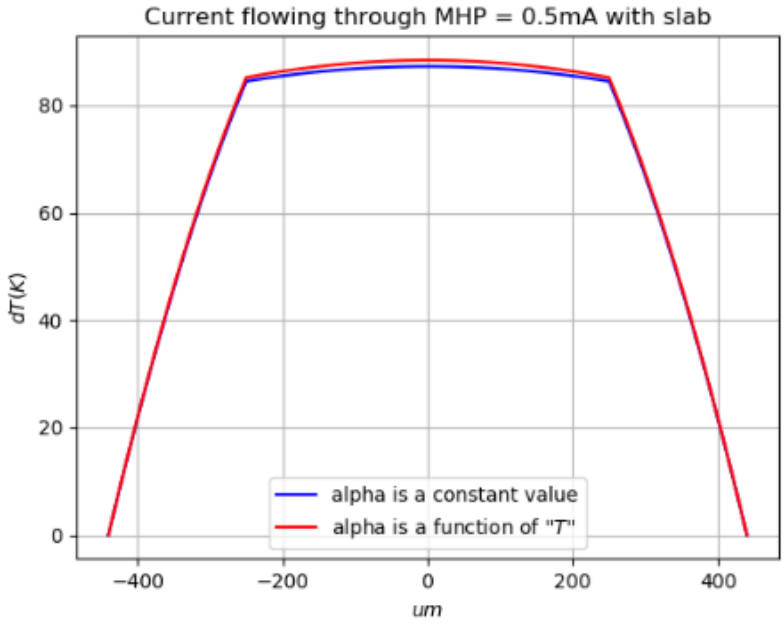

Fig. 4-30: Overheating temperature across the MHP for 2 different TCR functions at I = 0.5mA containing an Al slab

Analyzing Fig. 4-30, the slab significantly reduces the overheating temperature across the MHP as well as distributing it uniformly. The maximum overheating temperature decreased from 132°C to approximately 88°C for an input current of 0.5mA. This adjustment significantly optimizes the MHP's sensitivity. The thermal conductivity of Al was chosen to be 238W/mK with a thickness of 0.1um.

Temperature uniformity of the MHP was also simulated on COMSOL Multiphysics. Fig. 4-31a demonstrates a visual representation of the MHP covered by a 0.1µm thick Al thin film. In Fig. 4-31b, the temperature distribution as a function of the horizontal length is shown. The simulation was performed for the current of 1mA.

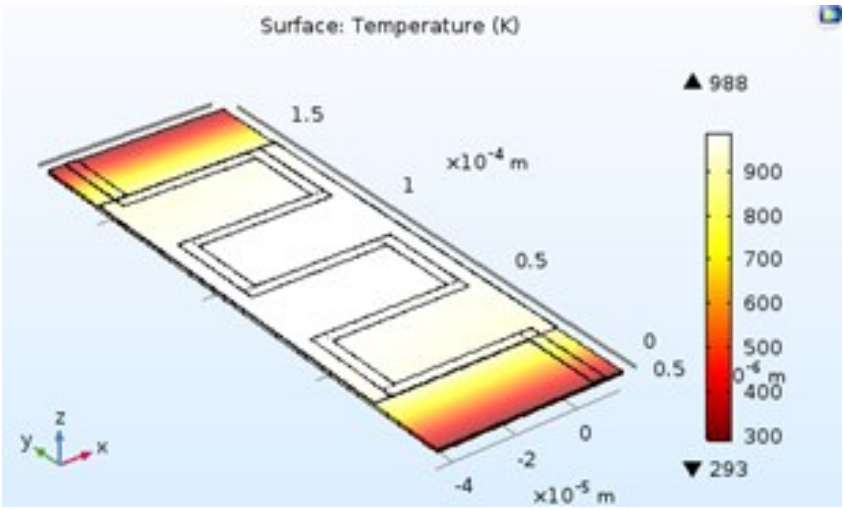

Fig. 4-31a: Visual representation of the MHP's temperature distribution with a 0.1µm Al slab

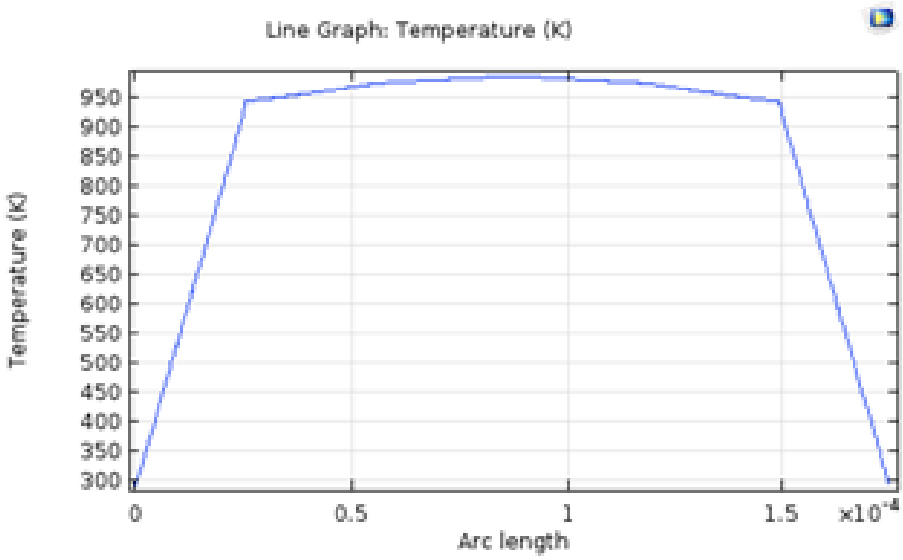

Fig. 4-31b: Graphical representation of the MHP's temperature distribution with a 0.1µm Al slab

Analyzing Figs. 4-31a,b, the temperature profile resembles to the results obtained on Fig. 4-30. The maximum temperature lowered and the distribution became more uniform to decrease the concentration of hot spots.

4.5 Summary

A thorough thermal analysis of the MHP was performed and the simulated results on Python and COMSOL Multiphysics were compared. It was found that despite various convergence algorithms in Python and COMSOL, final results correlated well. It was determined that the introduction of an Al slab significantly reduces the maximum temperature of the MHP and makes the temperature distribution of the MHP more uniform across the region thus avoiding the presence of hot spots and stabilizing the *TCR* of the poly-Si. Finally, simulations conducted on the temperature distribution of the MHP with a constant *TCR* and a temperature-dependent *TCR* resulted in minimal differences operated with a current of 0.5mA. For this reason, it is appropriate to approximate the *TCR* of the poly-Si heater to be 850ppm/K across the entire region of the device.

CHAPTER 5: EXPERIMENTAL MEASUREMENTS

5.1 Background

The MHP was experimentally tested in air at atmospheric pressure and in the vacuum chamber to detect changes in the overheating temperature, dT and Heat Loss Coefficient, HLC caused by gas composition and vacuum pressure variations. These experiments were conducted for air and water vapor measurements for pressure range from 1mTorr to atmospheric pressure. This was done to detect the level of minimal pressures the sensor can measure. Pirani-type sensors with MHPs provide a wide measurement range and good sensitivity at low power for different gases such as He, Ar, CH_4 (Methane), CO_2 [36].

In this chapter, the amplification circuit responsible for measuring heater and sensor voltages along with the signal processing unit and data acquisition board is presented. Signal processing routines of the MHP's heating will be explained. The MHP was tested with O_2, CO_2, and water vapor mixed in air. The device's sensitivity to every single gas is examined. Afterwards, the MHP's properties are evaluated in vacuum and freeze drying tests. Monitoring of water sublimation in vacuum based on pressure gradient measurement using at least two different Pirani sensors is discussed. The results obtained with three tested MHP's are presented after a reconfiguration of the Arduino-based system. Software application developed with Visual Basic.NET (a high-level programming platform) was combined with Arduino to display live measurement readings of the three sensors inside the vacuum chamber. Experimental results of the sensors are studied. Curve linearization technique is demonstrated for device calibration. Finally, results of water sublimation monitoring in vacuum during real freeze-drying process is presented.

5.2 Amplification Circuit, Data Acquisition, and Signal Processing

Signals from the thermal sensor were processed with a data acquisition system based on Arduino Uno microcontroller board as shown on Fig. 5-32a. Voltages U_0, U_{out}, U_{h0}, U_{h1} were measured

with a PmodAD5 24-bit analog-to-digital converter module built around the Analog Devices AD7193 Sigma-Delta ADC. An excitation voltage was generated with a MCP4725 12-bit DAC breakout board. Both ADC and DCA modules were assembled on a so-called PCB shield for Arduino Uno (Fig. 5-32a). Its block diagram is shown on Fig. 5-32b.

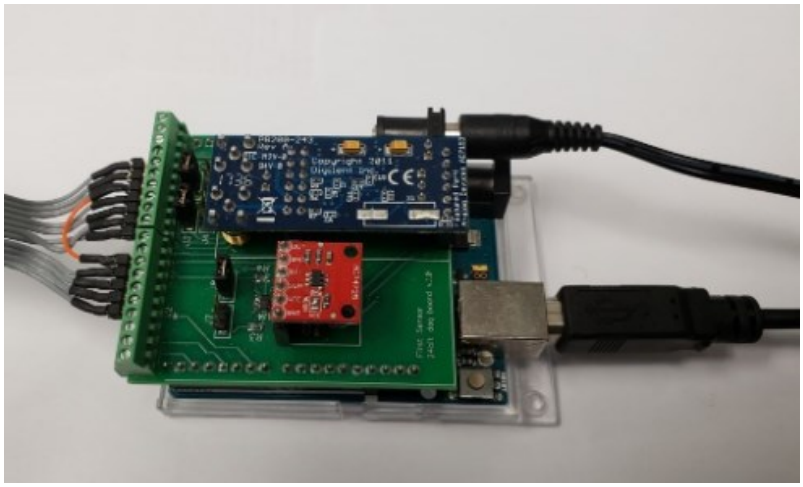

Fig. 5-32a: Data acquisition system

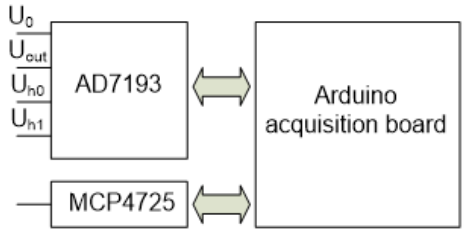

Fig. 5-32b: The system's block diagram

The usage of a microcontroller-based signal processing system allows simple implementation of an operating mode of the sensor with a constant overheating temperature. If the target overheating temperature is dT_{ref} and the actual overheating temperature measured at the heating voltage U_{h0} is dT, then the subsequent amplitude of the heating pulse can be determined as depicted in (5-28).

$$U_{h0\_next} = U_{h0} \frac{1+\frac{dT_{ref}}{dT}}{2} \quad (5\text{-}28)$$

By applying subsequent heating pulses with an amplitude defined in (5-28), it is possible to approach overheating temperatures close to the set target, dT_{ref} and keep it constant during the entire device's operation. In practice, the overheating temperature reaches a predetermined value, dT_{ref} with an accuracy of 0.05% or lower in approximately 5 pulses. Operating modes with constant dissipated power or constant heating voltage can be realized in a similar fashion.

The firmware uploaded on Arduino Uno provides the following signal processing routines described in the steps below.

Step 1: No heating of the MHP

- Applying a zero heating voltage, U_{h0}
- Measuring voltages, U_0 and U_{out}
- Calculating resistance, R_{s1}
- Calculating ambient temperature

Step 2: Heating of the MHP

- Applying a heating voltage, U_{h0}
- A delay of 10ms is applied (the time when dT of the MHP reaches a plateau)
- Measuring voltages U_0, U_{out}, U_{h0}, U_{h1}
- Calculating resistance, R_{s2} and dissipated power, P_{diss}
- Calculating overheating temperature, dT from R_{s2} and R_{s1}
- Calculating HLC: HLC = dT/P_{diss} [K/mW]
- Applying a zero heating voltage
- A delay of ~ 1000ms is applied (this time is needed for the cooling of the MHP)

Step 3: Optional (Performed at the end of Step 2)

- Adjustment of the heating voltage to keep a constant predetermined overheating temperature, dT_{ref} of the MHP

- Calculating the next heating pulse voltage depending on the deviation of the overheating temperature using (28)

Characterization of the sensor:

The targets of the experimental characterization of the thermal gas sensor include the following:

1) Estimate the basic performance of
    a) the sensor containing the MHP with a split electric heater and temperature sensor
    b) electronic circuitry
    c) signal processing algorithm
2) Evaluate the sensitivity of the sensor and a minimal detectable variation of thermal conductivity of the ambient gas
3) Investigate the functionality of the sensor as a Pirani-type vacuum sensor
4) Investigate the possibility to detect pressure gradients inside the vacuum chamber during freeze-drying process

The prototype of the thermal sensor along with its amplification circuitry are shown on Figs. 5-33a, 5-33b, respectively.

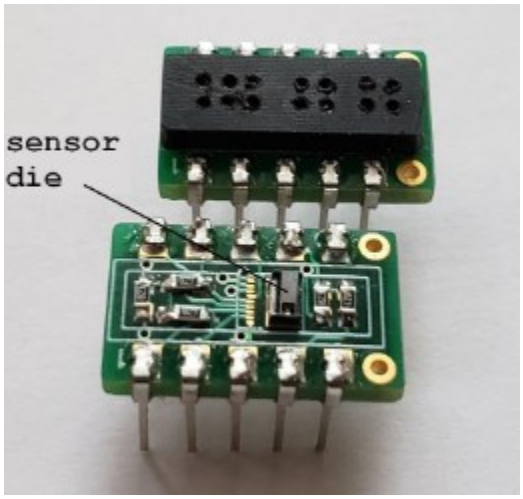

Fig. 5-33a: Prototype of the thermal sensor

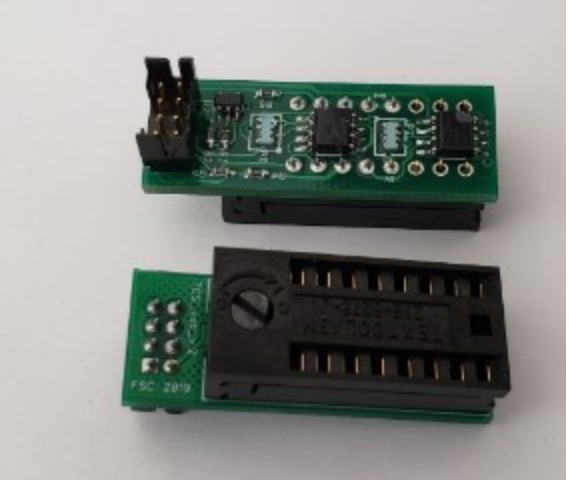

Fig. 5-33b: Thermal sensor's amplification circuitry

The sensor die containing three separate MHPs was packaged on a PCB with several ballast resistors (Fig. 5-33a). The amplification circuit assembled on a separate PCB has a ZIF (zero insertion force) socket for sensor connection. Signals from the sensor and amplification circuitry are processed with the Arduino based acquisition system described above in Fig. 5-32a.

5.3 Verification of Sensitivity to Different Gases Mixed in Air

Three gases have been chosen for experimental evaluation of the designed thermal sensor: Carbon dioxide (CO_2), Oxygen (O_2) and water vapor. The reasons for this choice are the following. First of all, a generation of gas mixtures with an accurate control of their thermal conductivity is important for sensor characterization. Oxygen and water vapor have thermal conductivities very close to air. That is why very small increments of thermal conductivity of gas mixtures of air/O_2 and of air/water vapor can be easily created by varying O_2 and water vapor concentrations. It is also important to take into consideration that such changes in concentrations can be accurately measured with commercially available humidity and Oxygen sensors.

Thermal conductivity of the third gas, CO_2 is significantly lower than air (about 33% less than air at room temperature). To create small increments of thermal conductivity of air/CO_2 gas mixtures, the concentration of CO_2 must be controlled at the level of hundreds and thousands of ppm.

Existing NDIR (non-dispersive infrared) sensors measure CO_2 concentration with an accuracy better than 100ppm. Therefore, it is possible to create miniscule changes of thermal conductivity of air/CO_2 gas mixtures by controlling the changes of CO_2 concentration.

An experimental setup for thermal conductivity measurements is shown on Fig. 5-34. The tested sensor was placed inside the metal box along with one of the two reference sensors. One reference sensor, SCD30 was used to monitor the concentration of CO_2 (using the NDIR principle), relative humidity and temperature. The second sensor is a galvanic cell type Oxygen sensor, KE-25.

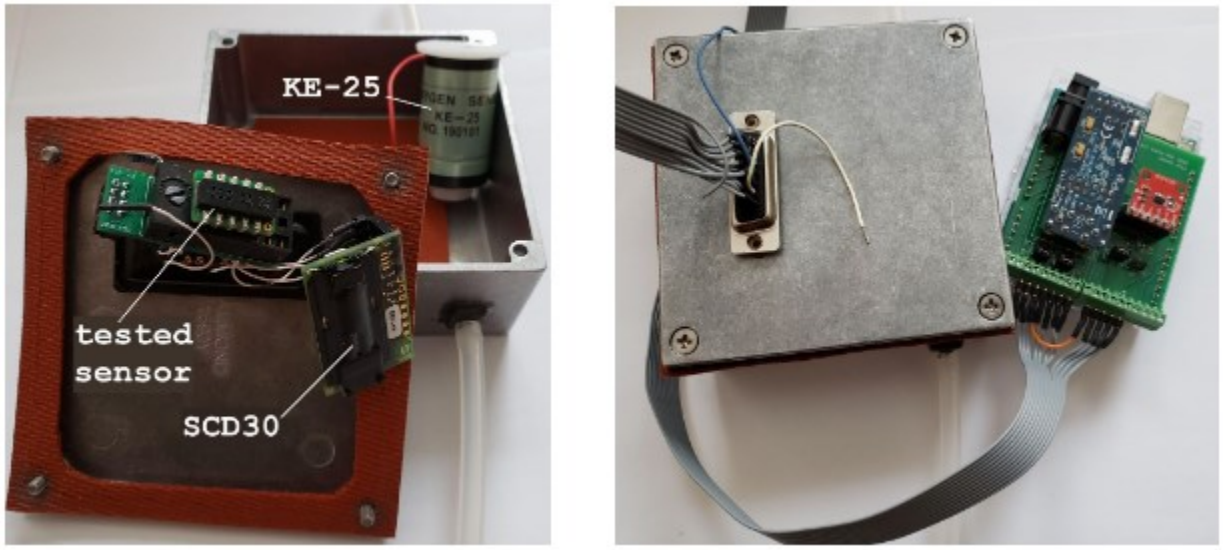

Fig. 5-34: Gas chamber with a tested sensor and reference sensors

5.3.1 Sensitivity to Oxygen

Measurements of Oxygen in the air/O_2 gas mixture by its thermal conductivity are assumed to be hardly possible because thermal conductivities of Oxygen and air are very close to one another. Nevertheless, the tested thermal sensor demonstrated significant sensitivity to Oxygen as shown on Fig. 5-35.

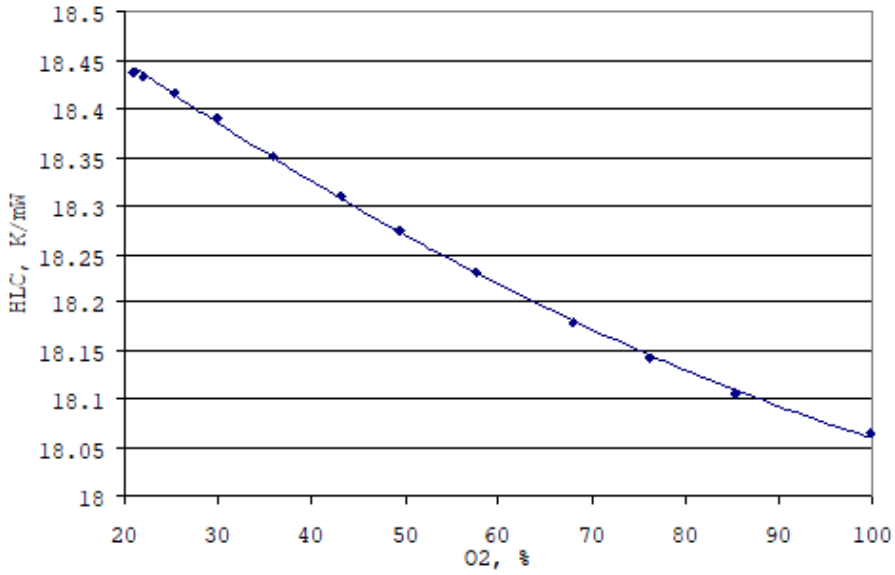

Fig. 5-35: HLC as a function of Oxygen concentration

5.3.2 Sensitivity to CO_2

Fig. 5-36 shows the heat loss coefficient, *HLC* as a function of CO_2 concentration. Measurements were performed at a constant ambient temperature of 23.5°C +/- 0.3°C and relative humidity of 16% +/- 0.1%. The same sensor's operating mode was used in all thermal conductivity tests which will be described below. The overheating temperature of the MHP was maintained at 40°C. Heating pulses of 10ms were applied at every second. The running average for five sequential measurements was used.

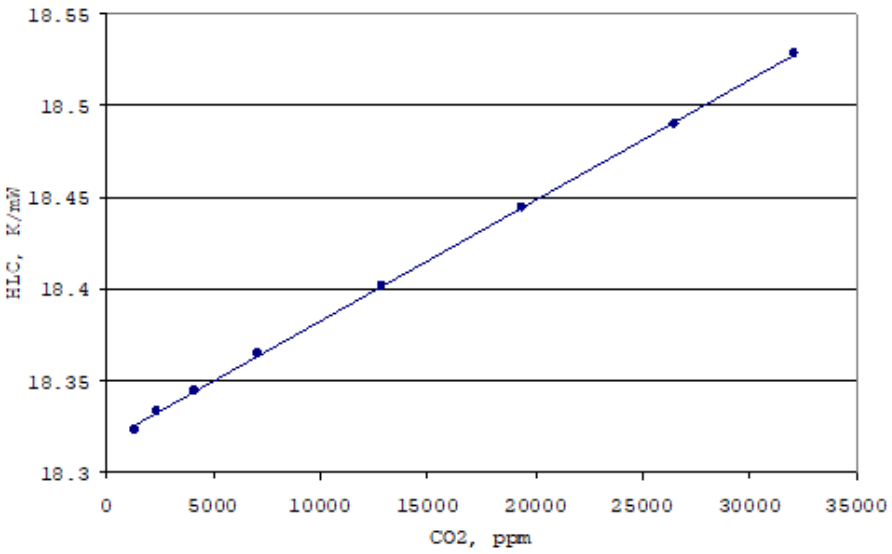

Fig. 5-36: HLC as a function of CO_2 concentration

5.3.3 Sensitivity to Water Vapor

The thermal sensor also demonstrated decent sensitivity to humidity. Relative humidity, *RH* is defined as the ratio of the partial water vapor pressure to the saturated vapor pressure. It was then converted to absolute humidity, *AH* which is proportional to the concentration of water molecules and is measured in grams of water vapor per cubic meter. The conversion formula is presented in (5-29). In (5-29), *T* is the ambient temperature.

$$AH = 216.7\frac{\frac{RH}{100\%}\alpha e^{\frac{\beta T}{\sigma+T}}}{273.15+T} \tag{5-29}$$

Table 5 presents the constants used in equation (5-29).

Table 5: Values of constants of (5-29)

Constant	Value
α	6.112hPa
β	17.62
σ	243.12°C

Fig. 5-37 presents data measured at 23.5°C +/- 0.5°C and at a constant CO_2 concentration of approximately 750ppm.

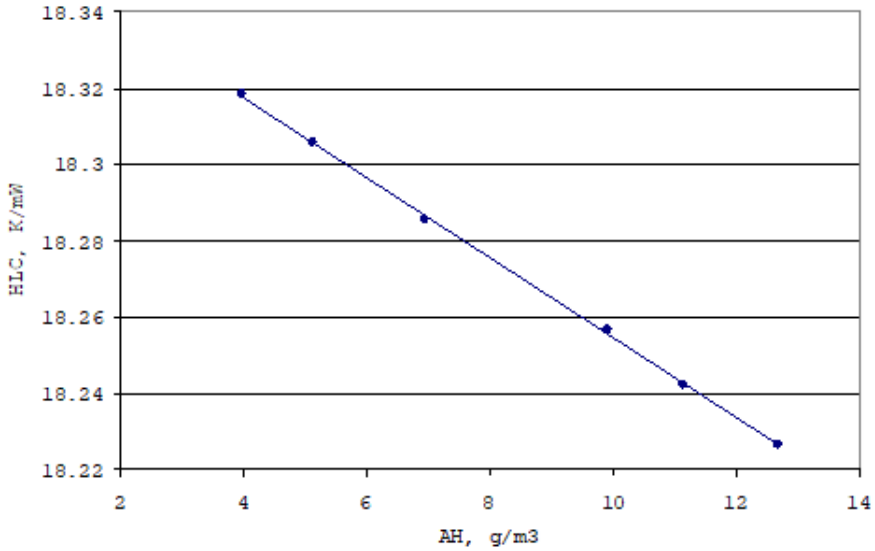

Fig. 5-37: HLC as a function of absolute humidity

5.3.4 Temperature Drift Compensation/TC Tests

In order to evaluate a minimal detectable change in thermal conductivity, the noise of the sensor was investigated. Fig. 5-38 shows the output of the sensor measured during 15 minutes of the experiment.

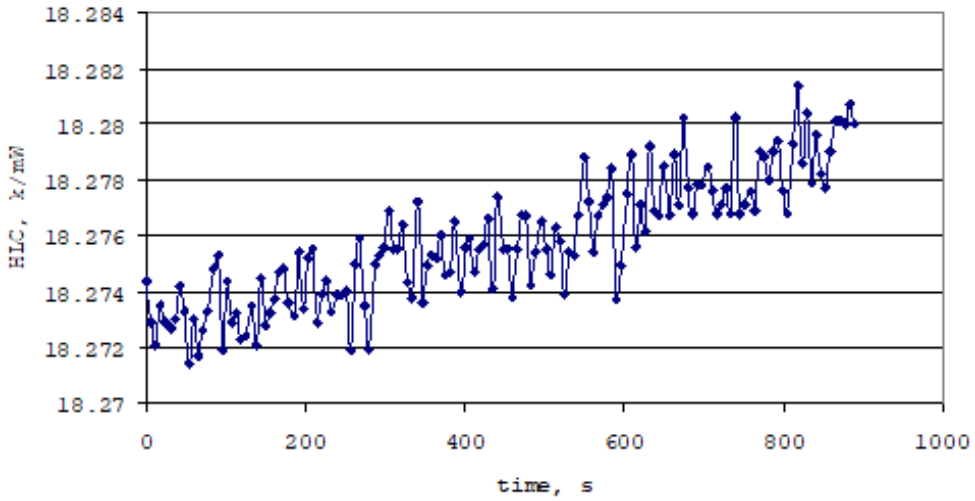

Fig. 5-38: Output noise of the thermal sensor during the 15 minutes of the experiment

It is known that the thermal conductivity of gases increases with temperature. Fig. 5-39 demonstrates temperature dependence of thermal conductivity of air (data obtained from [37]).

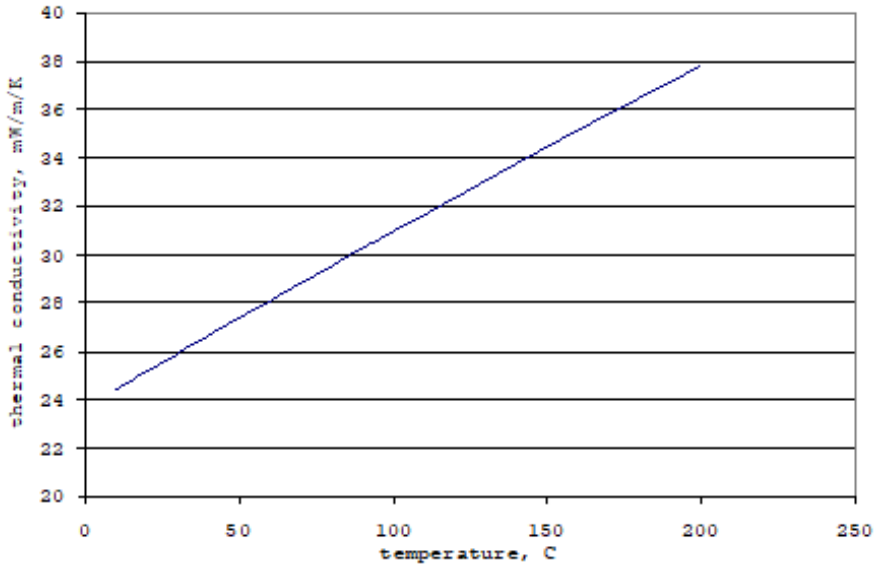

Fig. 5-39: Thermal conductivity of air versus temperature

The sensor's output demonstrates a time drift that can be explained by a drift of temperature. The temperature of the MHP measured during the same test (at zero dissipated power) is presented in Fig 5-40.

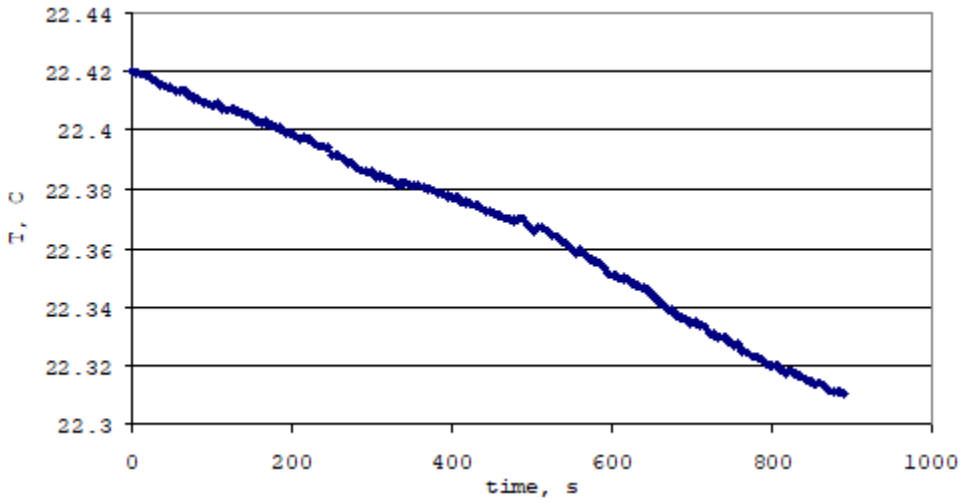

Fig. 5-40: Drift of the MHP's temperature during noise measurements

Thermal conductivity of air increases by approximately 0.29% per 1°C. To compensate for temperature drift of the sensor shown on Fig. 5-38 (which is inversely proportional to the thermal conductivity), the output signal must be multiplied by the following correction factor which is presented in (5-30).

$$CF = 1 + 0.0029(T - T_0) \tag{5-30}$$

Temperature, T_0 = 22.31°C was measured at the end of the test. The temperature compensated sensor output is shown on Fig. 5-41.

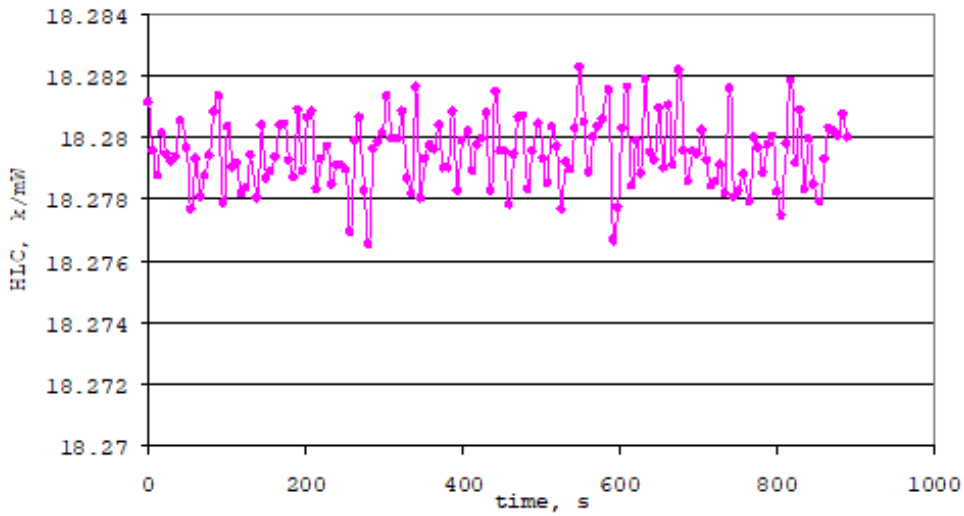

Fig. 5-41: Output noise of the thermal sensor after temperature drift compensation

Comparing Fig. 5-41 to Fig. 5-38, it is observed that with the introduction of the correction factor in (5-30) in order to compensate for the temperature drift, it is possible to stabilize temperature drift of the sensor.

Results of thermal conductivity tests are presented below.

1) The average value of HLC during the 15 minutes of the experiment (after temperature compensation): *HLC* = 18.2795K/mW
2) The standard deviation of the output signal with 5 second averaging (after temperature compensation): 0.00115K/mW or 0.0063% of the averaged *HLC*
3) Sensitivity to CO_2: 0.0066K/mW or 0.036% of *HLC* per 1000ppm of CO_2
4) Minimal detectable CO_2 concentration equivalent to standard deviation of the sensor signal during 15 minutes: 175ppm
5) Sensitivity to absolute humidity: -0.0105K/mW or -0.057% of HLC per 1g/m^3
6) Minimal detectable absolute humidity change which is equivalent to the standard deviation of the sensor signal during the 15 minutes: 0.1g/m^3
7) Sensitivity to Oxygen: -0.0058K/mW or -0.032% of HLC per 1% of O_2 between 21 and 40% of O_2 concentration in air
8) Minimal detectable O_2 concentration equivalent to the standard deviation of the sensor signal during the 15 minutes: 0.2%

5.4 Characterization of Thermal Conductivity Sensor in Vacuum

Tests were conducted for the sensors inside the vacuum chamber for air measurements.

Fig. 5-42a shows the overheating temperature of the thermoresistor, dT_s as a function of pressure from 1mTorr to atmospheric pressure recorded at three different excitation voltages. Excitation voltages are presented in Table 6.

Table 6: Voltages applied to the Data Acquisition System

Voltage	Value, V
V_1	0.61
V_2	0.86
V_3	1.84

Measurements in blue correspond to V_1; measurements in pink correspond to V_2; measurements in yellow correspond to V_3.

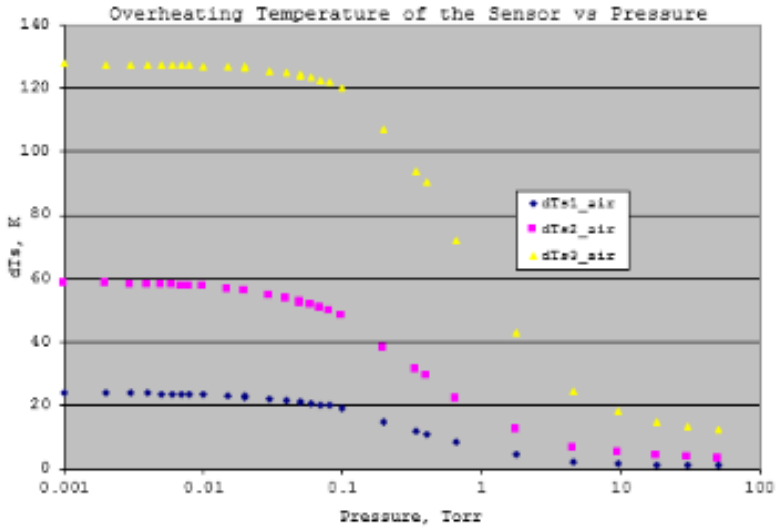

Fig. 5-42a: Overheating temperature of the sensor vs pressure (in air) for 3 voltages

As it is seen, dT_s is low for high pressures due to large heat transfer from the MHP into the ambient by the molecules of the ambient gas. As pressure lowers, heat transfer of the gas reduces. This forces the MHP to overheat to very large temperatures.

In Fig. 5-42b below, the overheating temperature of the heater, dT_h as a function of pressure is presented.

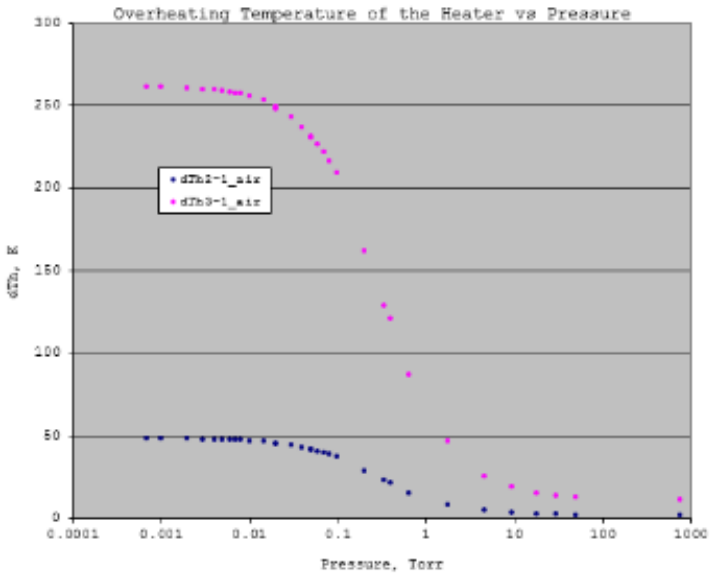

Fig. 5-42b: Overheating temperature of the heater vs pressure (in air) for 3 voltages

It is observed that for pressures of around 1mTorr, dT_h reaches around 260°C, whereas dT_s reaches around 130°C for V_3. This experimentally determined discrepancy is explained by the simulation of temperature distribution across the MHP and the investigation of *TCR* of poly-Si at different overheating temperatures.

Finally, in Fig. 5-42c, experimental data of the inverse of *HLC* vs pressure has been gathered and analyzed for the three excitation voltages.

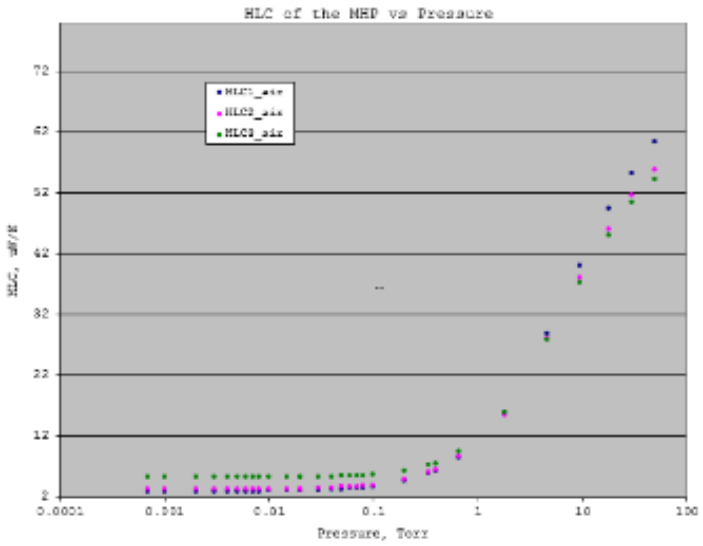

Fig. 5-42c: Inverse of HLC for 3 voltages as a function of pressure (in air)

As should be anticipated, the relationship of inverse of *HLC* vs pressure follows an inversely proportional behavior to that of *dT* vs pressure. This is due to P_{diss} being constant for all pressures.

5.5 Detection of Pressure Gradients at Vacuum during Water Sublimation. Measurements with Two Standard Pirani Sensors.

Emulation of freeze drying process:

Two tests have been conducted to imitate the process of freeze-drying and confirm the existence of pressure gradients caused by water sublimation. An additional Pirani gauge was connected to the vacuum chamber close to the vial with water as shown on Fig. 5-43.

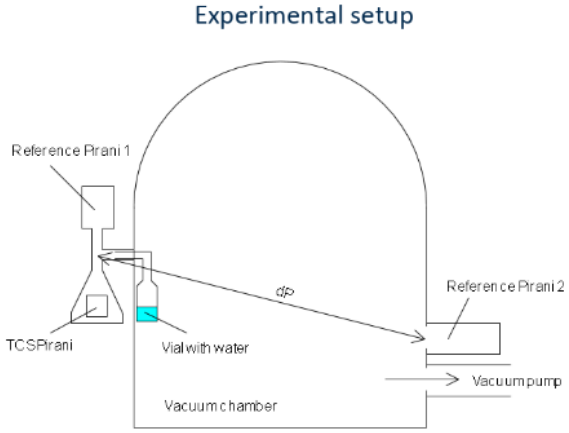

Fig. 5-43: Vacuum chamber with 2 different Pirani gauges

The following experiment was conducted with an empty vial and with a vial filled with water to detect differences in pressures between two gauges. In Fig. 5-44a, experimental data shows a pressure response of two Pirani sensors in the vacuum chamber with an empty vial.

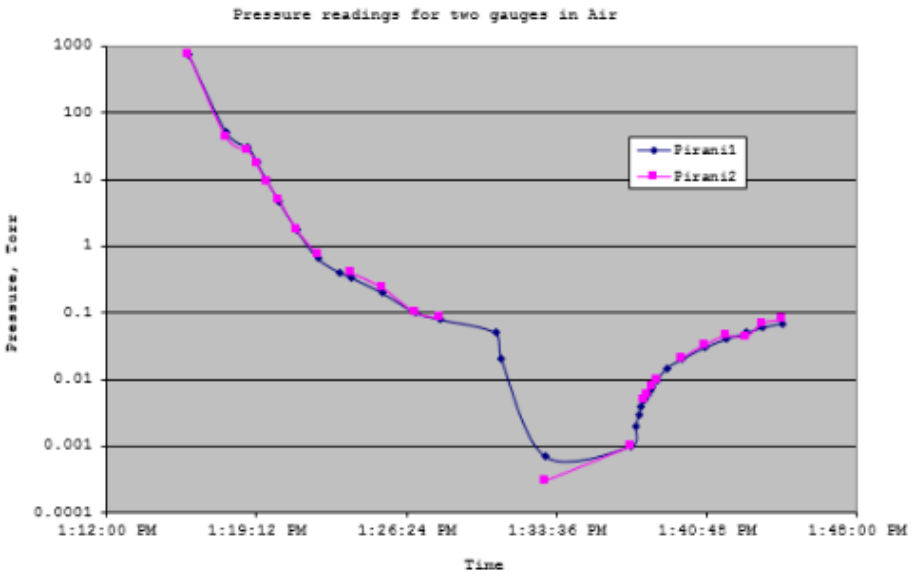

Fig. 5-44a: Pressure response of two gauges as a function of time with an empty vial

Analyzing the results, it can be noticed that in the absence of water, two Pirani sensors demonstrate similar curves when pressure inside the chamber varies. This part of the experiment indicates no pressure gradients, *dP* between two Pirani gauges.

In the 2nd part of the experiment, a vial was filled with water and placed inside the vacuum chamber and the experiment was repeated. Results are shown in Fig. 5-44b.

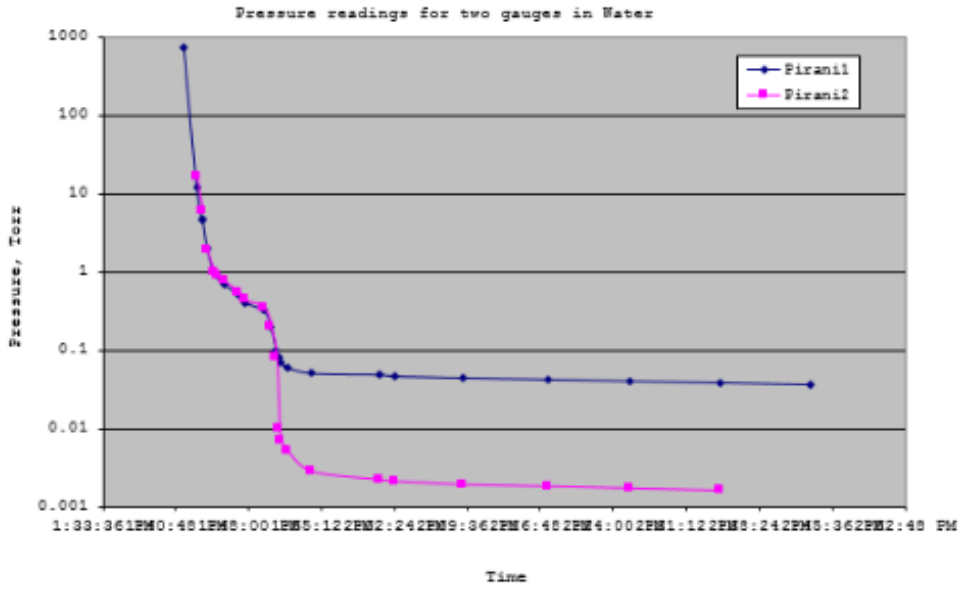

Fig. 5-44b: Pressure variations of two gauges as a function of time with a vial filled with water

In Fig. 5-44b, it is seen that both gauges at around 100mTorr begin to deviate from one another when a vial with a small amount of water is placed inside the chamber. This suggests that the vial with water resulted in significant and observable pressure gradients detected by two reference gauges.

To compare different times of water sublimation, a smaller amount of water was inserted inside the vial in the 2nd experiment. This is depicted in Fig. 5-44c.

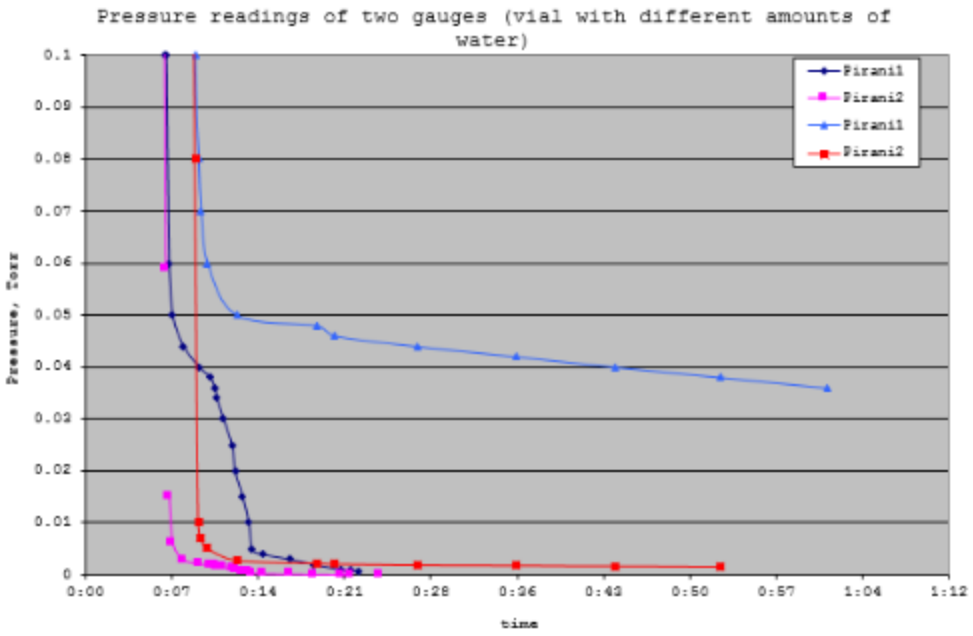

Fig. 5-44c: Pressure response of 2 gauges vs time with different amounts of water in the vial

The curves in dark blue and pink correspond to the pressure readings of the two gauges (Pirani I, Pirani II) with four droplets of water inside the vial. The curves in light blue and red correspond to the same two gauges but with the vial containing seven droplets of water. As it is observed, the more liquid is added inside the vial, the longer it is required to wait until complete sublimation. It is also demonstrated that for larger amounts of water added to the vial, larger pressure gradients, *dP* are observed between the two Piranis when the water has fully sublimated.

The described experimental setup was used in the experiments to verify the concept of controlling freeze-drying processes with miniaturized Pirani sensors.

5.6 Detection of Pressure Gradients with Miniature TC Sensors

Electronic circuitry was modified for vacuum and freeze-drying tests. An Arduino based data acquisition system was re-configured to collect data from three different thermal sensors. The MHPs of the sensors contain 4kΩ heating resistors with R_h connected to 4kΩ ballast resistors, R_{bh}.

Heating pulses with a duration of 150ms and constant amplitude of 1.1V (dissipated power of approximately 0.3mW) were applied with intervals of 1000ms.

5.6.1 Experimental Setup

Vacuum tests and an imitation of freeze-drying process were conducted at Concordia University. Fig. 5-45a,b shows the location of thermal sensors inside the vacuum chamber. Sensors 1 and 2 were placed beside the openings of the vials. Sensor 3 was placed close to the input of the vacuum pump.

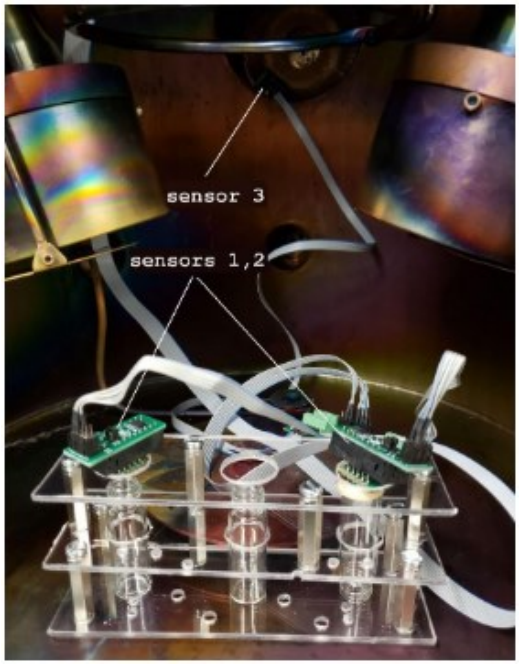

Fig. 5-45a: Three thermal sensors inside the vacuum chamber

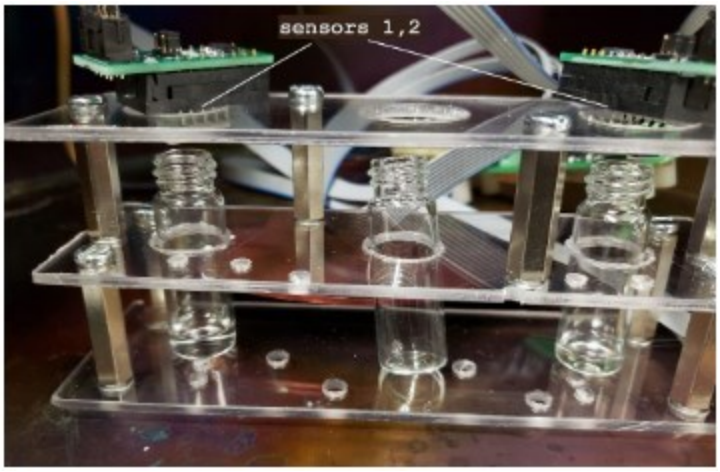

Fig. 5-45b: Zoomed-in view of the three thermal sensors inside vacuum chamber

5.6.2 VB-Based Application for TC sensors

Measurements were taken on 3 MHP sensors. The control board design was modified in order to place 2 more sensors and to establish a connection between the Arduino kit and the pad.

Arduino was programmed to control all physical parameters of the 3 sensors such as P_{diss}, HLC, dT, R_s. A high level programming platform, Visual Basic.NET was integrated with Arduino using the handshaking protocol to automatically display all the appropriate measured values inside the text boxes while Arduino kept on updating new recordings of the sensors. The default form view of the program is presented in Fig. 5-46.

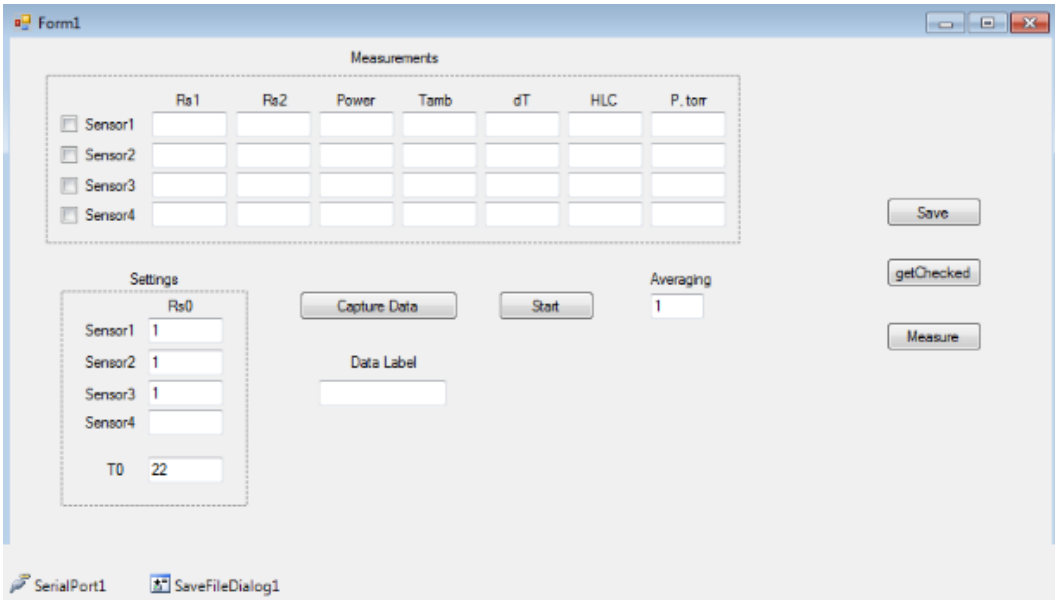

Fig. 5-46: Default Visual Basic Form (before program compilation)

The three sensors were tested for vacuum and freeze-drying measurement processes. The data labels above the text boxes and buttons are explained in Table 7. Button descriptions are presented in Table 8. The relationship between R_{s1} and R_{s2} is shown in (5-31).

$$R_{s2} = R_{s1}\left(1 + \alpha_{poly}\, dT\right) \tag{5-31}$$

From (5-31), α_{poly} is the *TCR* of the polysilicon of the thermo-resistor for each of the 3 sensors. α_{poly} = -1300ppm/K for temperature ranges from 10°C to 200°C. Taking into consideration that the overheating temperature of the sensors does not exceed 90°C at the lowest pressures (in the 50mTorr ranges), it is correct to use a constant value of α_{poly} over the entire experimental measurement course.

Table 7: Explanation of Data Labels

Data Label, Unit	Explanation
R_{s0}, Ω	Initial thermo-resistor sensors' values at atmospheric pressure (before the start of the experiment)
R_{s1}, Ω	Subsequent thermo-resistor sensors' values at recorded pressure readings (after the start of the experiment)
R_{s2}, Ω	Thermo-resistor sensors' values after being overheated by an incremental change of temperature, dT. The relationship between R_{s1} and R_{s2} is presented in (31)
Power, mW	Dissipated power across the thermo-resistor MHPs
T_{amb}, °C	Ambient temperature of the 3 sensors for different pressures
dT, °C	Overheating temperature of the 3 sensors for different pressures
HLC, µW/K	Heat loss coefficient for the 3 sensors for different pressures (defined as *Power*/*dT*)
P, torr	Text box originally designed to display pressure readings from the Pfeiffer sensor of the vacuum chamber. It was decided to abort this idea due to its complexity. The pressure readings would be automatically typed in the textbox under the label 'Data Label'.
Averaging	Textbox which displays the amount of data recordings that will be averaged from Arduino's processing.
T_0, °C	Textbox that displays the room temperature

Table 8: Description of Buttons

Button(s) Name	Description
Start	Button responsible for starting the program (beginning of program execution, full display of all the values inside their respective text boxes, button's text is changed from "Start" to "Stop" once pressed). When the experiment is decided to be terminated by the user, the user clicks the "Stop" button
Capture Data	Button responsible for capturing data from all textboxes and saving them in a text format. For instance, when a pressure reading is decided to be saved, the user enters that pressure reading in the text box below 'Data Label' and afterwards presses the button, 'Capture Data'
Save, getChecked, Measure	Corresponding buttons were added for verification and testing purposes. These buttons were unused during sensor measurements

In Fig. 5-47 below, the running program is presented. The readings are initially recorded for atmospheric pressure (760Torr). The first test was performed for air measurements; the second test was performed for water measurements in order to detect the stage of freeze drying process.

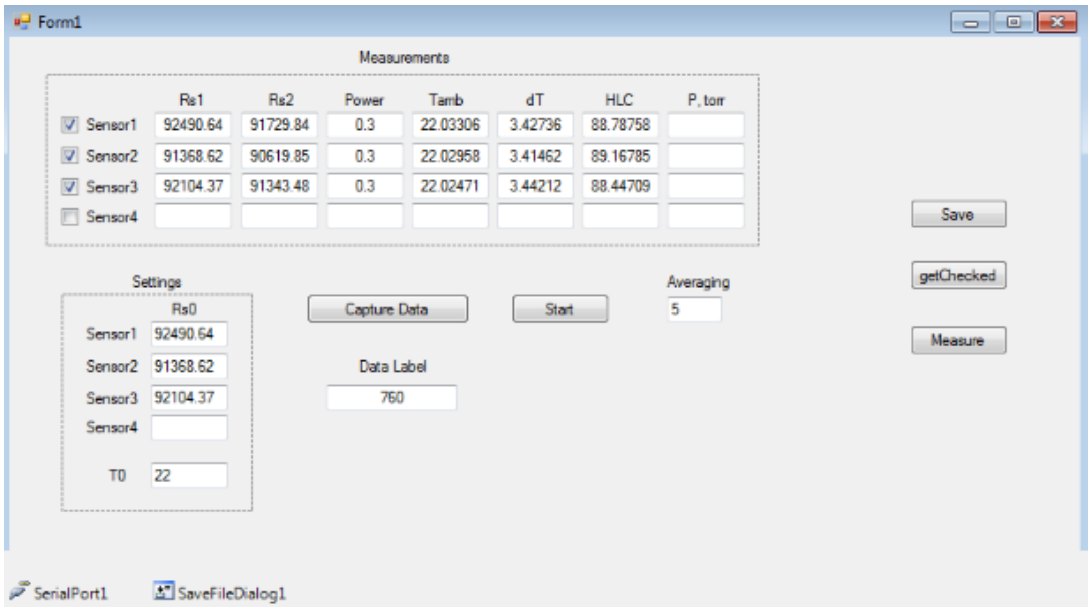

Fig. 5-47: Execution of the program (sensor value parameters at 760Torr) – air measurements

As it is observed from Fig. 5-47, all 3 sensors are checked and their information is displayed in the corresponding textboxes of the Visual Basic program. The averaging was set to 5 which averages 5 data point measurements. In Fig. 5-48, the program depicts sensor results for a pressure reading of 10mTorr.

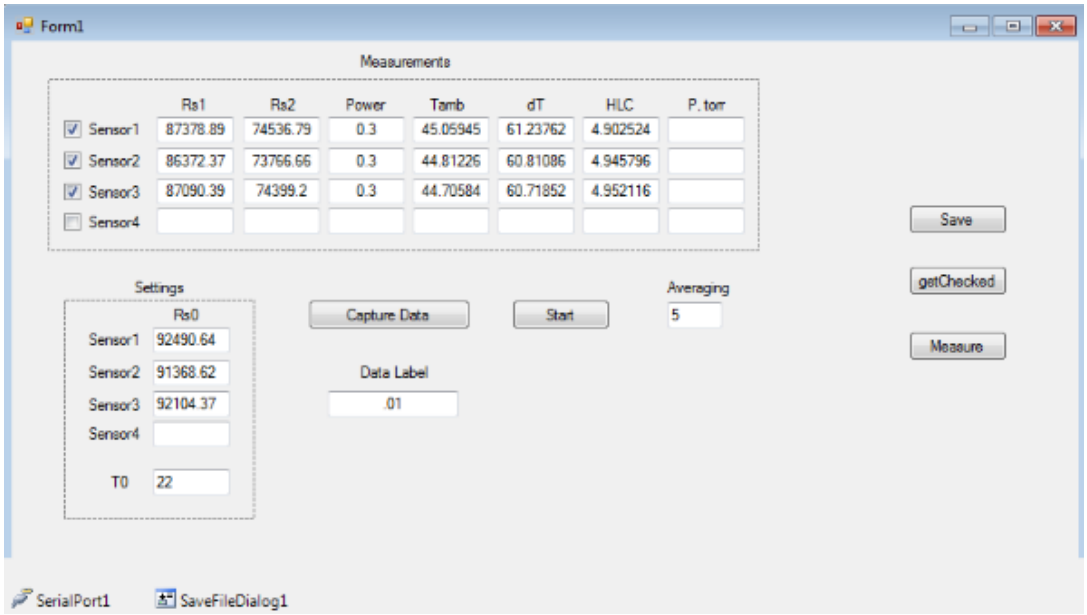

Fig. 5-48: Execution of the program (sensor value parameters at 10mTorr) – air measurements

Analyzing the three sensor results from Figs. 5-47, 5-48, it can be noticed that the overheating temperature, *dT* for the 3 sensors has increased on average by nearly 20 times (from ~3°C to ~60°C) for a pressure change from 760Torr to 10mTorr. As a result of an increase of *dT*, thermo-resistor values have dropped from approximately 90kΩ on average to about 74kΩ on average for the 3 sensors. This is a direct consequence of equation (5-31) where the *TCR* of the polysilicon corresponds to a negative value. Further analysis indicates a decrease of the average inverse *HLC* readings for the 3 sensors (~89μW/K to ~4.9μW/K). This is once again an anticipated result since the inverse *HLC* is inversely proportional to *dT*.

In Fig. 5-49, the sensor readings are recorded for the same 3 sensors at a pressure of 10mTorr, however this time, for water measurements (2nd experiment). Sensor 3 was empty; Sensor 1 was filled with 4 droplets of water; Sensor 2 was filled with 7 droplets of water. This experiment was conducted in order to determine the stage of freeze drying process.

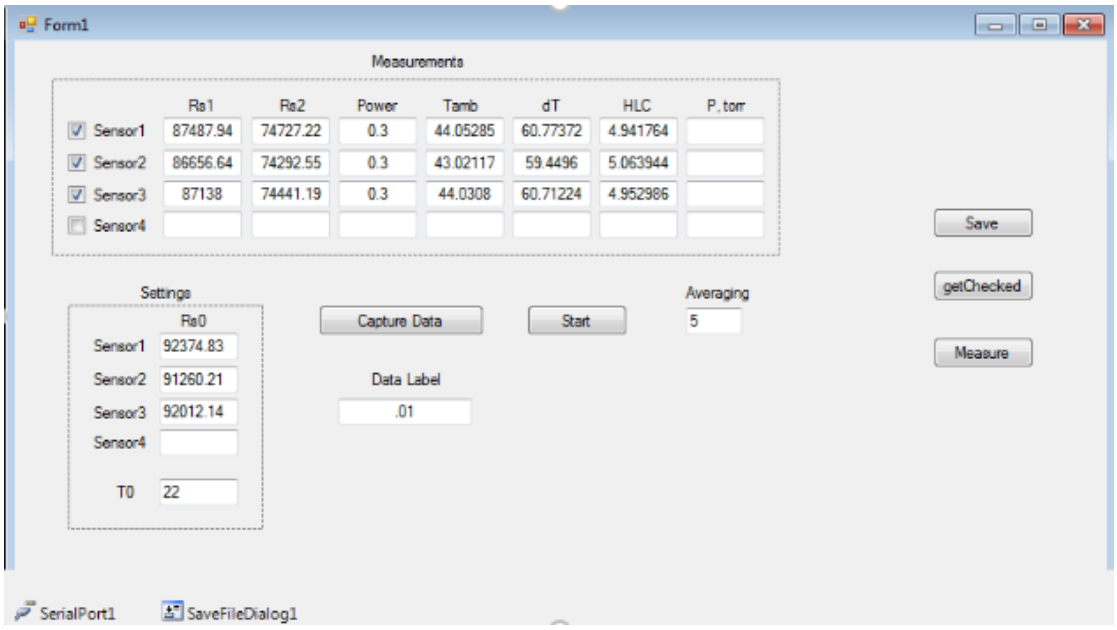

Fig. 5-49: Execution of the program (sensor value parameters at 10mTorr) – water measurements

Observing the overheating temperatures of the 3 sensors at 10mTorr from Fig. 5-49 and comparing them with the results depicted on Fig. 5-48, it can be suggested that with the addition of water, the

overheating temperatures of Sensors 2 and 3 have lowered particularly for Sensor 2, since 7 droplets of water has been added inside the vial which was located directly below Sensor 2's sensing area.

After all pressure readings were captured from the executing program, the 'Stop' button was pressed and all the data were saved in a text format as represented below in Fig. 5-50.

```
0.007           ,12:43:53 PM
87410.16,74594.65,0.3,44.4037,61.08896,4.915256,
86557.23,74111.32,0.3,43.47506,59.91178,5.023572,
87052.72,74310.21,0.3,44.41701,60.99036,4.92955,
```

Fig. 5-50: A sample data measurement at 7mTorr saved in the following manner – water measurements

As pictured in Fig. 5-50, a sample data is saved at 7mTorr conducted for a water measurement experiment. Row 1 indicates the pressure being stored along with the recorded current time the experiment took place at. Rows 2, 3, 4 indicate Sensors' 1, 2, 3 parameters (R_{s1}, R_{s2}, *Power*, T_{amb}, *dT*, inverse *HLC*), respectively. Afterwards, the text file was formatted using Java programming language to contain each sample data measurement in 1 row instead of 4 rows. These data were then copied to Excel where processing of results took place.

5.6.3 Experimental Results

First vacuum tests were conducted with no water in the vials. The pressure response for the three thermal sensors is shown on Fig. 5-51a,b. The overheating temperature of the sensors reaches ~ 72°C for high vacuum which defines a maximum heat loss coefficient, *HLC* = 240K/mW. The sensors demonstrate sensitivity to pressure down to about 1mTorr. At pressures below 1mTorr, the sensors' output reaches saturation.

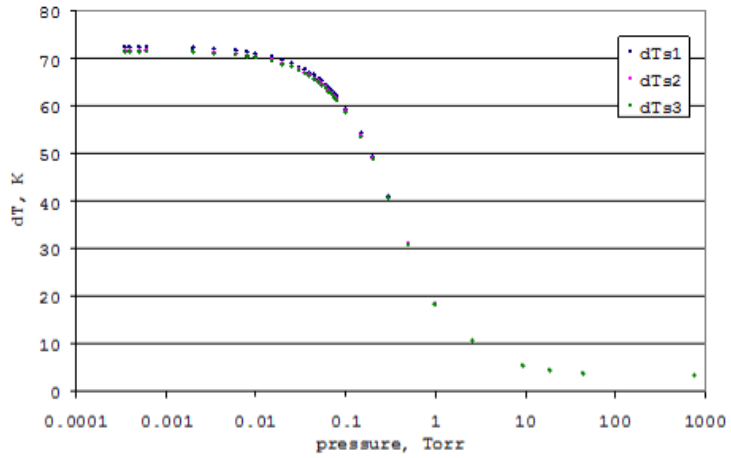

Fig. 5-51a: Pressure response of three thermal sensors (0.1mTorr – 760Torr)

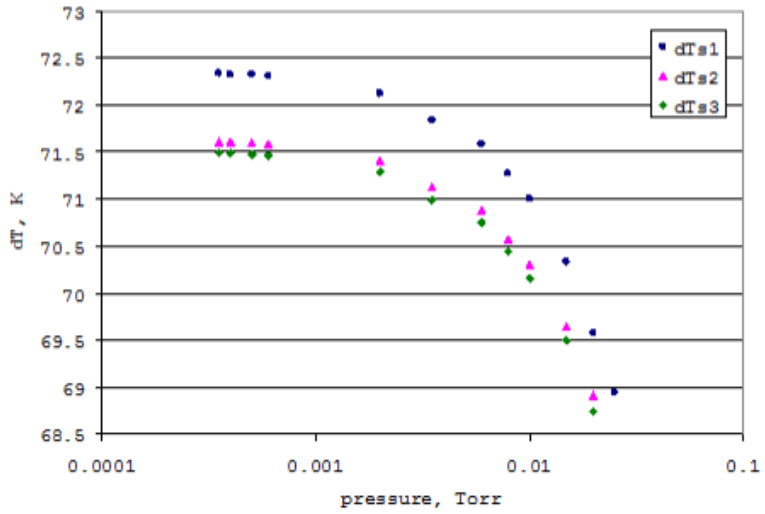

Fig. 5-51b: Pressure response of three thermal sensors (0.1mTorr – 0.1Torr)

The present setup was used to investigate a possibility to measure pressure gradients caused by water sublimation. Afterwards, the vacuum pump started to operate. Fig. 5-52a shows the overheating temperature of the three sensors versus time. Evaporation of water causes its rapid cooling and freezing in about 5-7 minutes after the start of the experiment.

Fig. 5-52b presents the difference of overheating temperatures between sensors 3 and 1 and between sensors 3 and 2, respectively. A rapid change of temperature difference occurred in ~ 19

minutes for vial 1 (sensor 1) and in ~ 25 minutes for vial 2 (sensor 2). It is assumed that the observed inflection of the temperature curves is an indicator of the end of water sublimation. Until sublimation is not finished, sensors 1 and 3 measure pressure higher than that of sensor 2. The end of sublimation is associated with a reduction of average pressure and pressure gradients inside the chamber. Water sublimation for the second vial takes longer time because more water was added to this vial.

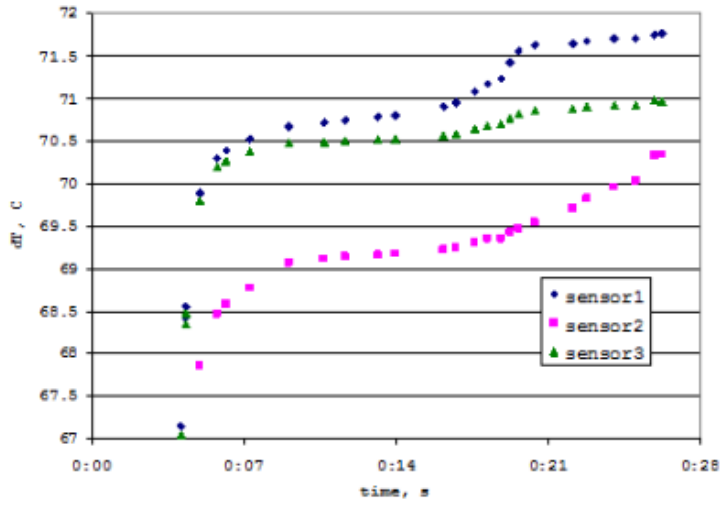

Fig. 5-52a: Overheating temperature of the three sensors during water sublimation process

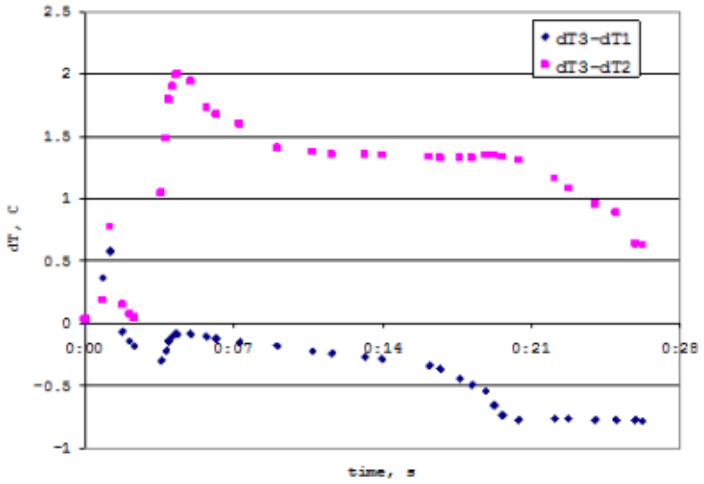

Fig. 5-52b: Difference between overheating temperatures of the sensors

5.6.4 Curve Linearization Analysis

Once all the data measurements have been recorded, it is essential to linearize pressure response of the sensor for device calibration.

In this sub-section, the transfer output of HLC vs pressure will be demonstrated. A formula will be determined which approximates the behavior of the transfer signal versus pressure. The device needs to be properly calibrated. The output of the sensor must be converted into pressure readings. The procedure of this conversion is by nature a linearization procedure.

A sample test was performed in air at a voltage of 1.1V. Fig. 5-53 below shows the relationship between the transfer signal vs pressure.

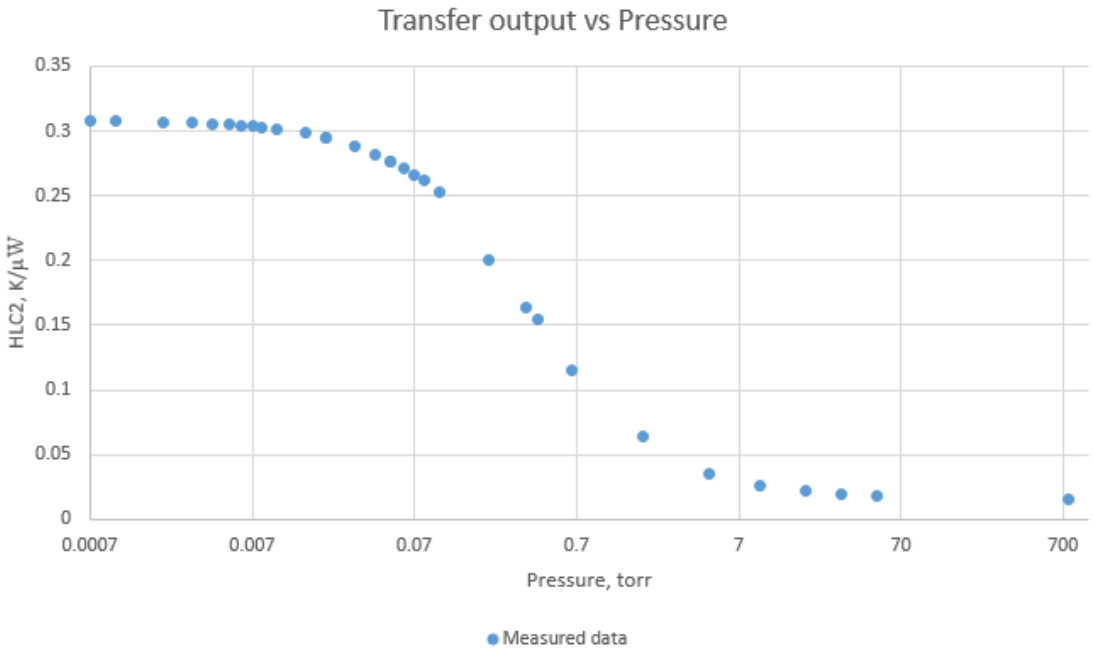

Fig. 5-53: Measured transfer signal of the MHP for a range of pressures inside the vacuum chamber. Device was tested in air at V = 1.1V

In order to properly calibrate the following curve, it is necessary to determine the equation of the curve above. Van Herwaarden et al [38] explained how to correctly linearize the transfer signal curve.

A theorem governing vacuum measurements of the MHP is the gradient of pressures of the thermal conductivities of different gases [10]. On Fig. 5-54, a simple schematic of the MHP with two heat sinks is shown.

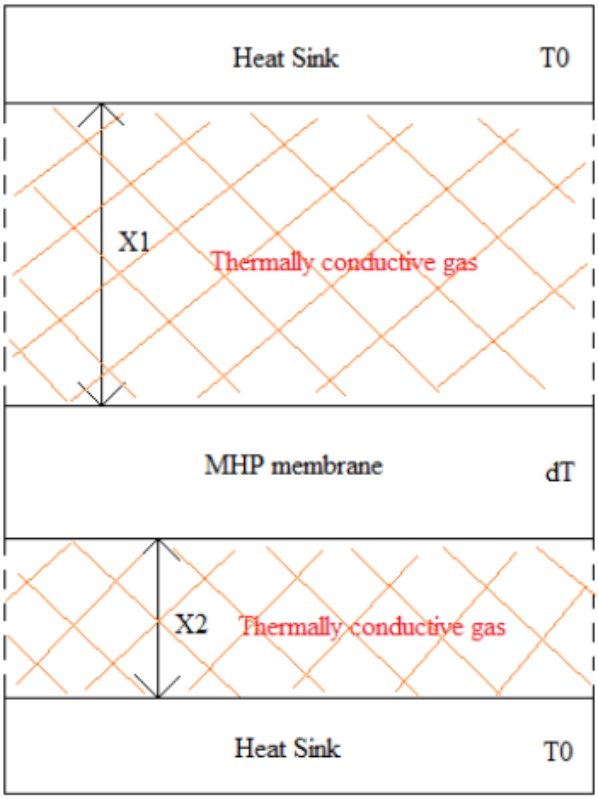

Fig. 5-54: Simple schematic of the MHP showing two heat sinks at ambient temperature, T_0 with corresponding distances, X_1 and X_2 from the membrane, conductive gas surrounding the MHP, the MHP membrane at an overheating temperature, dT

As pictured above, the membrane is located at distances X_1 and X_2 from both heat sinks. In the presence of a thermally conductive gas along with pressure differences, heat will be transported across the entire MHP.

Molecular theory of gases states that the amount of heat that is conducted between the spacing gaps of the membrane and the sinks is proportional to the number of gas molecules when condition (5-32) is satisfied, where μ is the mean free path of molecules.

$$X_1, X_2 \gg \mu \tag{5-32}$$

In this case, the thermal conductivity of a gas is proportional to pressure. However, when the mean free path becomes greater than the gap spacing, thermal conductivity of the gas is no longer proportional to the pressure. This results in a stabilization of thermal conductivity of a gas.

Van Herwaarden et al [38] presented a formula for the total thermal conductivity of a gas as a function of pressure. This is presented in (5-33) and the description of its parameters are presented in Table 9.

$$G = \frac{1}{2} G_0 P \left(\frac{P_{t1}}{P + P_{t1}} + \frac{P_{t2}}{P + P_{t2}} \right) \tag{5-33}$$

Table 9: Description of Parameters of Equation (5-33)

Parameter	Description
G_0	low-pressure thermal conductance of the gas (pressure-independent)
P	Pressure readings of the Pfeiffer sensor
Expression inside the ()	Stabilization of thermal conductivity at high pressures
P_{t1}, P_{t2}	Transition pressures of the heat transfer between the gaps. They are inversely proportional to gap spacings, X_1, X_2

Taking into consideration that both sinks are located equally from the device's membrane, $P_{t1} = P_{t2}$. Applying the selection method, the corresponding coefficients were determined. The values of G_0 and P_t are presented in Table 10.

Table 10: Values of G_0 and P_t of Equation (5-33)

Parameter	Value
G_0	0.76
$P_{t1} = P_{t2} = P_t$	0.3875Torr

Plugging in the aforementioned coefficients into (5-33), the calibrated curve along with the measured data is presented in Fig. 5-55 below.

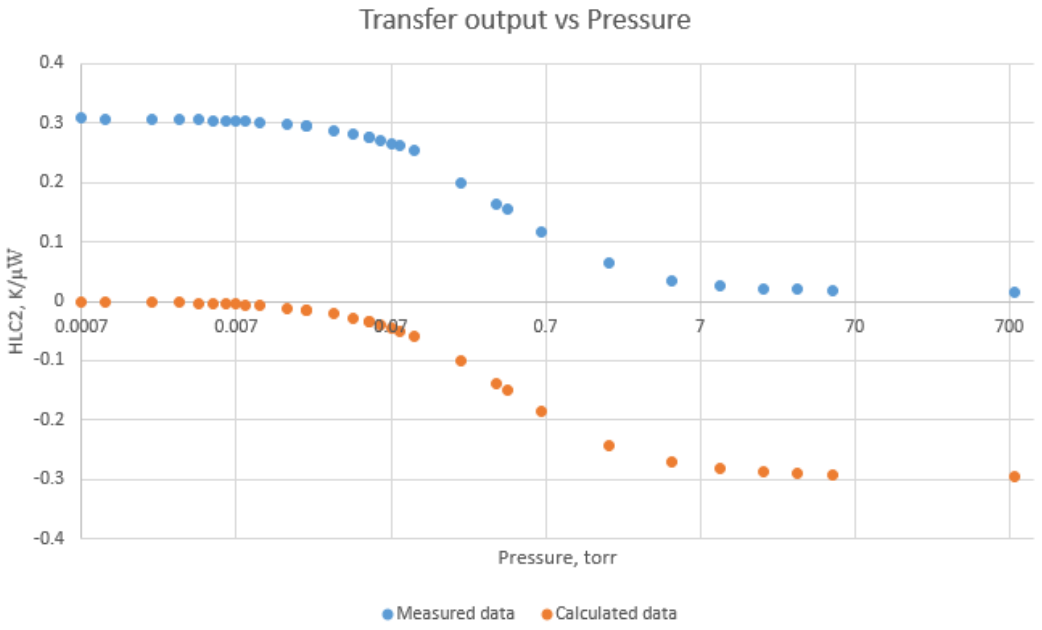

Fig. 5-55: Transfer output vs pressure for the measured transfer signal and the calculated curve for the device tested in air at V = 1.1V used for sensor calibration. No offset.

Analyzing the curves, it can be seen that both of them run parallel to one another. The last adjustment that needs to be made is the inclusion of the offset for the calibrated curve. The offset was chosen based on the value of the transfer signal at the lowest pressure. The offset is denoted by G_{mem}. Based on experimental data point measurements, the lowest pressure to be recorded was 0.7mTorr. This corresponds to a G_{mem} of a value of 0.308071K/mW. Hence, the calibrated relationship of the output signal versus pressure is modified in (5-34).

$$G = G_{mem} + \frac{1}{2} G_0 P \left(\frac{P_{t1}}{P + P_{t1}} + \frac{P_{t2}}{P + P_{t2}} \right) \tag{5-34}$$

(5-34) is further simplified since $P_{t1} = P_{t2}$. The final calibrated curve is presented in (5-35).

$$G = G_{mem} + G_0 P \left(\frac{P_t}{P + P_t} \right) \tag{5-35}$$

The final calibrated result is presented in Fig. 5-56 below.

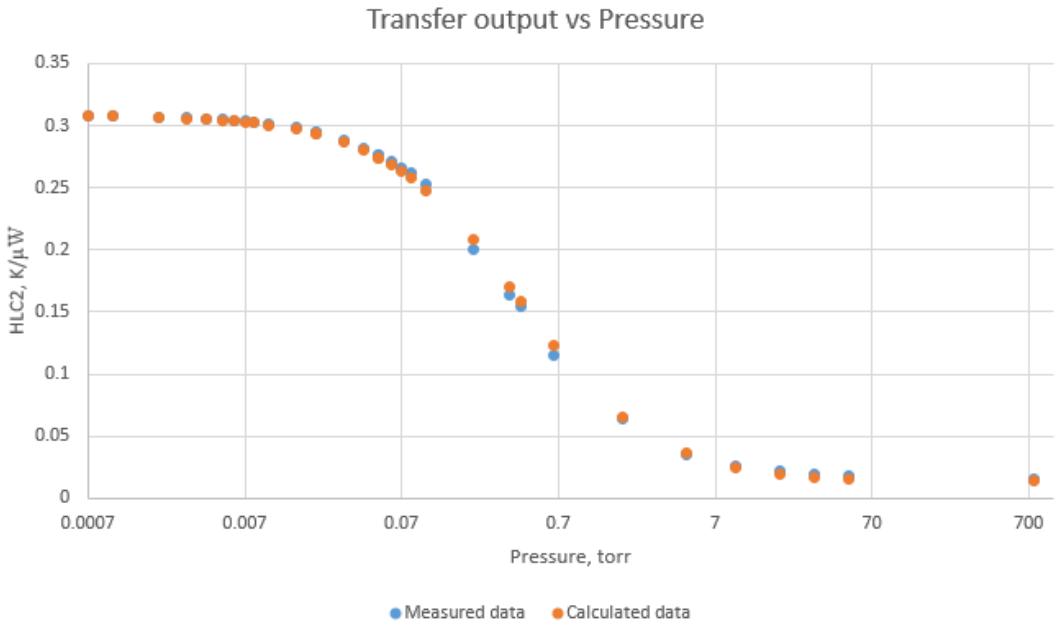

Fig. 5-56: Transfer output vs pressure for the measured transfer signal and the calibrated curve for the device tested in air at V = 1.1V with offset

5.7 Detection of Pressure Gradients in Real Freeze-Drying Process

The real freeze-drying test was performed at Palladin Institute of Biochemistry of the National Academy of Science of Ukraine (NASU) in Kiev.

A Laboratory Freeze Dryer LyoQuest-80 was manufactured by AZBIL TELSTAR Technologies (Spain) was used in the tests as shown on Fig. 5-57.

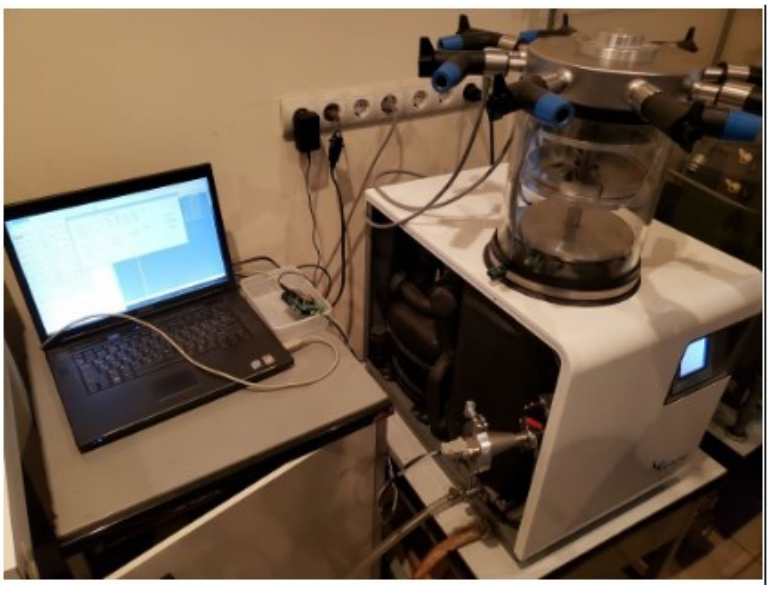

Fig. 5-57: Freeze-drying setup

The dried material used in the experiment was Protein C, 50µg in the vial. The volume of the water solution was 0.5mL, buffer – Tris C. Molar mass 121.14 g/mol, chemical formula $C_4H_{11}NO_3$, density 1.326 g/cm^3, pH = 7.4. The material in the vials was frozen at -20°C before the start of freeze-drying.

Fig. 5-58 depicts the vials with the dried material (after sublimation) along with the sensors placed on the shelves. Sensors 1 and 3 were placed on the shelves close to the vials with the sublimated material. LyoQuest Dryer contained a condenser – cylindrical cavity with the walls cooled down to -83°C where the water sublimated from the vials was condensed. Sensor 2 was placed inside the cylindrical volume.

In approximately 75 minutes after the start of the process, the shelves began to heat. Their temperature steadily increased up to approximately 50°C. The output signals of the three sensors were monitored during the freeze-drying process.

Fig. 5-58: Vials with sublimated material along with thermal sensors

Fig. 5-59a,b shows the obtained results. Though, the walls of the condenser were cooled down to -83°C, the temperature of sensor 2 stayed between 15°C and 18°C during the test. The heating of the shelves also caused sensors 1 and 2 to heat.

After about 2 hours and 30 minutes after the start of freeze-drying, the raise of overheating temperatures of sensors 1 and 2 ceased which can be interpreted as an indication of the end of the sublimation stage. During the next 2 hours and 30 minutes, overheating temperatures of sensors 1 and 2 remained constant.

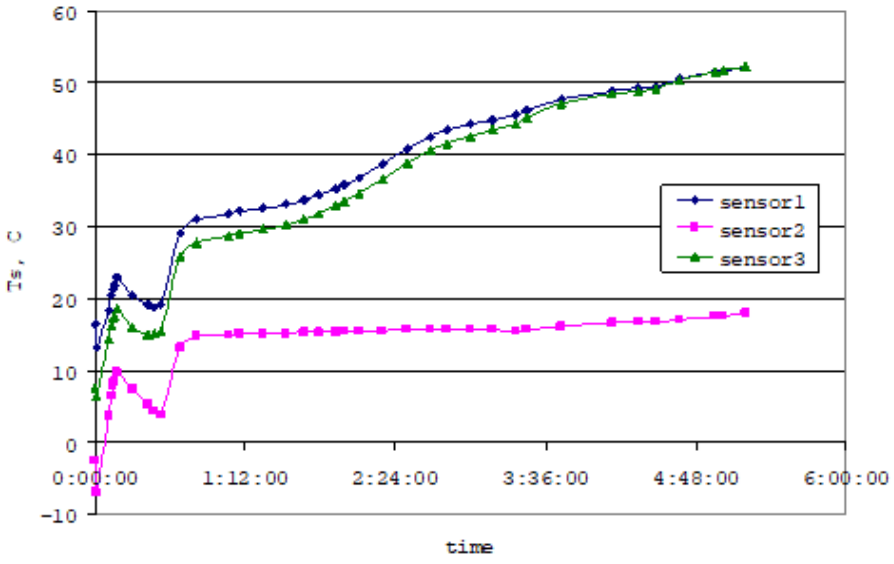

Fig. 5-59a: Temperature of the sensors during freeze-drying process

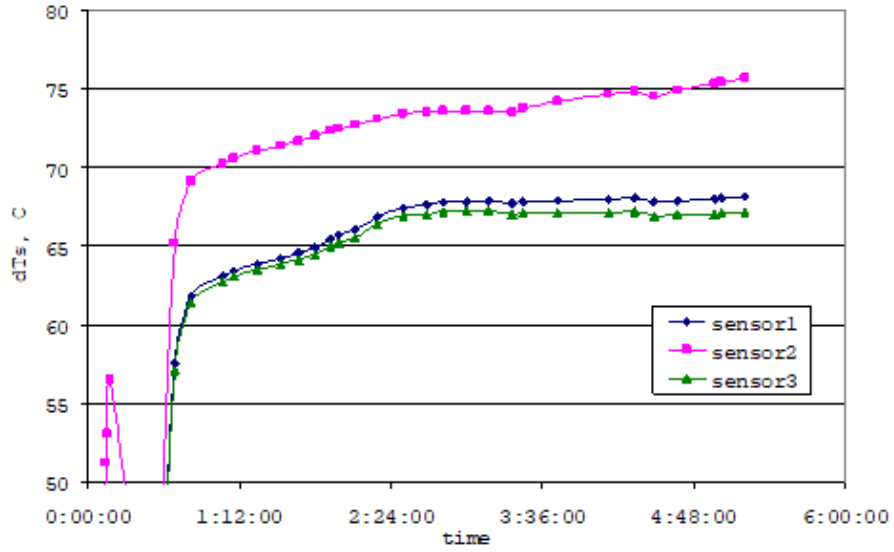

Fig. 5-59b: Overheating temperature of the sensors during freeze-drying process

5.8 Summary

The CMOS compatible MEMS-based thermal gas sensor was investigated. The sensor was fabricated using the technology owned by First Sensor Corp. The MHP of the sensor contained two functional polysilicon resistors used as an electric heater and a temperature sensitive element.

The resistance of polysilicon resistors was investigated from -20°C to 250°C and a significant reduction of the absolute value of thermal coefficient of resistance, *TCR* with temperature increase was discovered. The observed effect has serious consequences for the sensor design and its operating mode. First, the operation at temperatures (ambient plus overheating temperature) higher than ~ 200°C must be avoided because the sensitivity of the sensor reduces due to a drop of its *TCR* value. Second, the design of the MHP layout must exclude local hot spots as much as possible where the *TCR* of the temperature sensitive resistor is reduced resulting in a decrease of sensitivity of the sensor. Third, the calculation of the actual temperature of the MHP must be performed along with the *TCR* as a temperature dependent parameter. Temperature calculation based on the assumption of a constant *TCR* gives a significant error.

The temperature distribution across the MHP was simulated. It was shown that a placement of an Aluminum slab on top of the MHP improves temperature uniformity and minimizes the negative effect of hot spots.

The operating mode of the thermal sensor with an electrically split heater and temperature sensitive resistors was analyzed. It was shown that the influence of potential instability of polysilicon resistors can be minimized at calculations of power dissipated across the MHP and its overheating temperature. As a result, the output parameter of the sensor – heat loss coefficient, *HLC* defined as the ratio of overheating temperature and dissipated power can be determined with high accuracy. Possibilities of the thermal sensor to detect small variations of gas compositions and measure vacuum pressures were investigated. It was experimentally proven that the sensor can detect extremely small variations of thermal conductivity of air to about 0.006% of its absolute value. This resolution of the thermal sensor in the measurement of gas thermal conductivity is equivalent to changes of CO_2 concentration in air at the level of ~ 175ppm or variations of concentration of Oxygen in air at the level of ~ 0.2%. Such high resolution of the sensor may be of interest for gas sensing applications.

The investigated thermal sensor also can be used for vacuum pressure measurements. It demonstrated a good sensitivity down to about 1mTorr.

The operation of the thermal sensor in the freeze-drying process was experimentally tested. Three sensors were placed inside the commercial Freeze Dryer LyoQuest-80 and the measured pressure gradients inside the vacuum chamber during the freeze-drying process were obtained. First, experimental results indicated a possibility of the sensors to detect changes in pressure gradients caused by water sublimation process. A control system based on several miniature thermal sensors can indicate the end of primary drying stage that may be very important in optimization of the freeze-drying technique.

CHAPTER 6: DESIGN OF A TC SENSOR USING POLYMUMPS PROCESS

6.1 Background

A thermal conductivity sensor was designed for gas sensing applications using Cadence Virtuoso software. PolyMUMPs process was used to fabricate the MHP. The reason behind this was to come up with another design different from the MHP designed by First Sensor Corp. The MHP designed using CMOS technology contained the heat sink 100µm from the membrane's sensing element. However, using PolyMUMPs process, the heat sink would be only 2µm away from the sensing area. This significant difference would result in a different heat transfer mechanism and would increase the sensitivity of the sensor at higher pressures. Another important difference from the structure described in the previous chapters that may change is the heat transfer and as a result, the performance of the MHP device is that the heater and the temperature sensor are not laying on the same dielectric membrane but are separated by gaps.

PolyMUMPs is one of the oldest commercially available surface-micromachining processes [39]. Its abbreviation stands for polysilicon multi-user micromachining process (specifically a three-layer polysilicon process). The process starts with a 150mm n-type (100) silicon wafers of 1-2Ω-cm resistivity [40]. Figs. 5-60a,h show a graphical representation of the PolyMUMPs process.

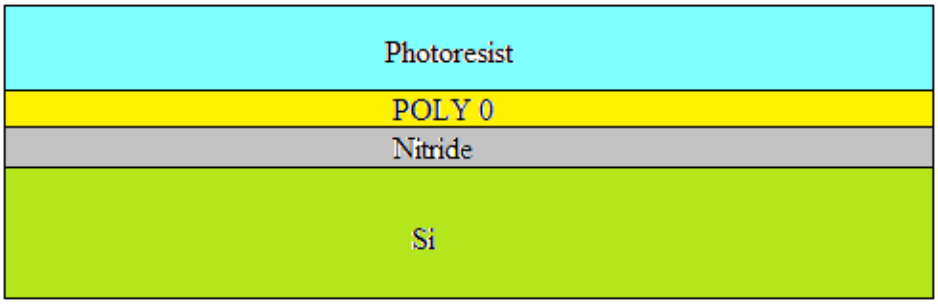

Fig. 5-60a: Surface of the n-type (100) wafers are heavily doped with phosphorus. A 600 nm layer of low stress of Si_3N_4 (Nitride) is deposited followed by a layer of 500 nm polysilicon (Poly 0). The wafers are then coated with a UV-sensitive photoresist.

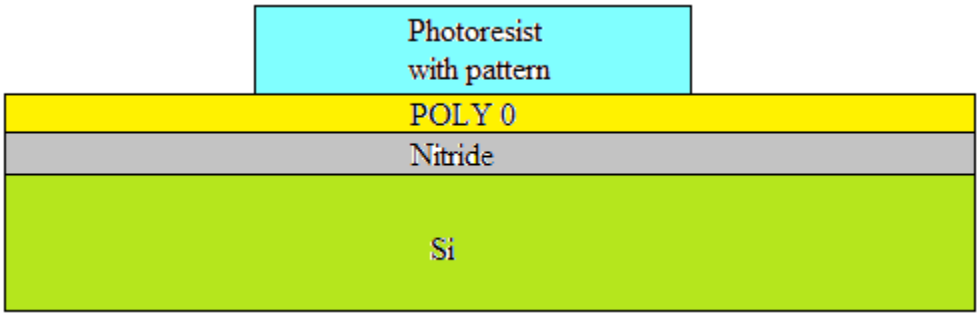

Fig. 5-60b: The photoresist is lithographically patterned by exposing it to UV light through the first level mask (POLY 0). The photoresist in unwanted areas is removed leaving behind a patterned photoresist mask for etching.

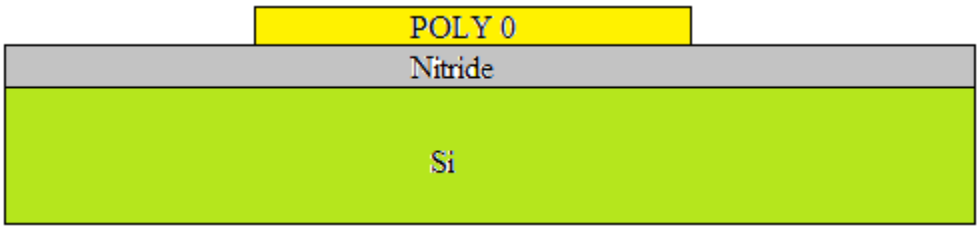

Fig. 5-60c: Etching is performed to remove the unwanted polysilicon.

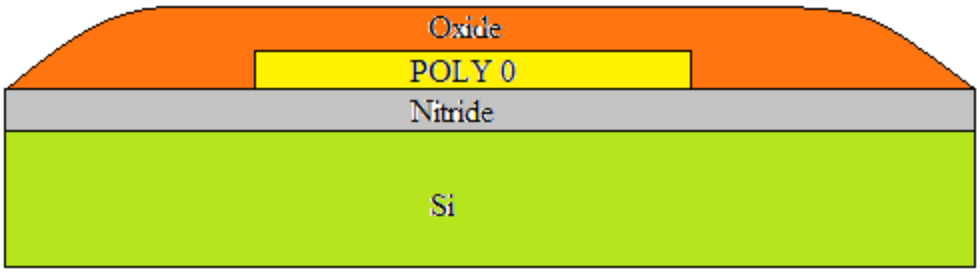

Fig. 5-60d: A 2 µm layer of SiO_2 is deposited (1st layer). This corresponds to the first sacrificial layer.

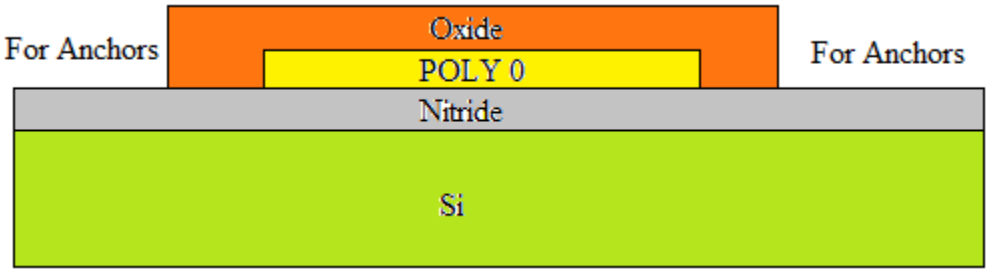

Fig. 5-60e: The unwanted oxide is removed to create areas for anchors.

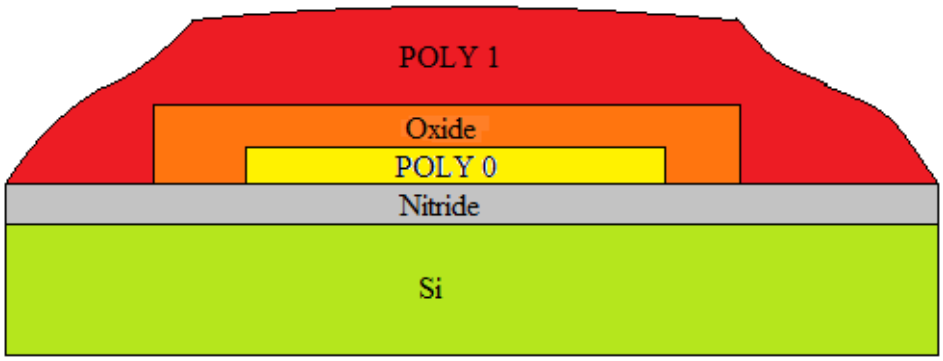

Fig. 5-60f: A 2 µm layer of un-doped polysilicon is deposited (POLY 1).

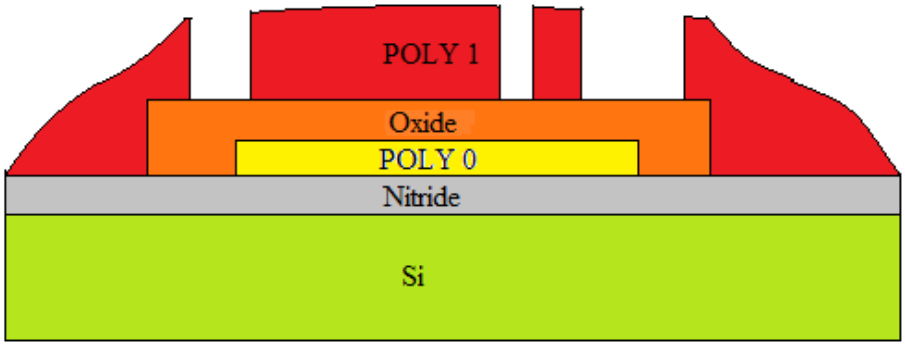

Fig. 5-60g: The wafer is coated with photoresist and the fourth level (POLY 1) is lithographically patterned. POLY 1 is etched using plasma processing.

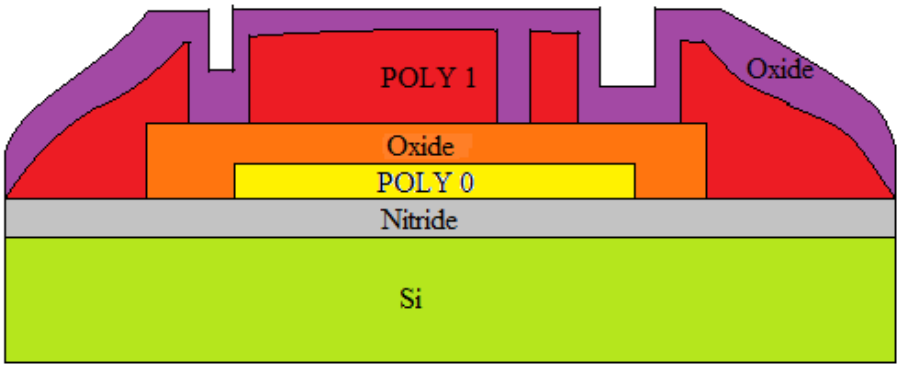

Fig. 5-60h: 2nd Oxide layer is deposited on the wafer. This layer is patterned twice to allow contact to both POLY 1 and substrate layers. Similar process continues for POLY 2 deposition.

In order to correctly design the following MHP using PolyMUMPs technology, a particular set of rules needed to be obeyed. These set of rules are defined by the limits of the process [40]. The MHP was designed by adhering to all minimum line widths, spaces and overlaps between different material layers to avoid design rule violations.

6.2 Layout of the Sensing Element

The final layout of the MHP designed using PolyMUMPs process is presented in Fig. 5-61.

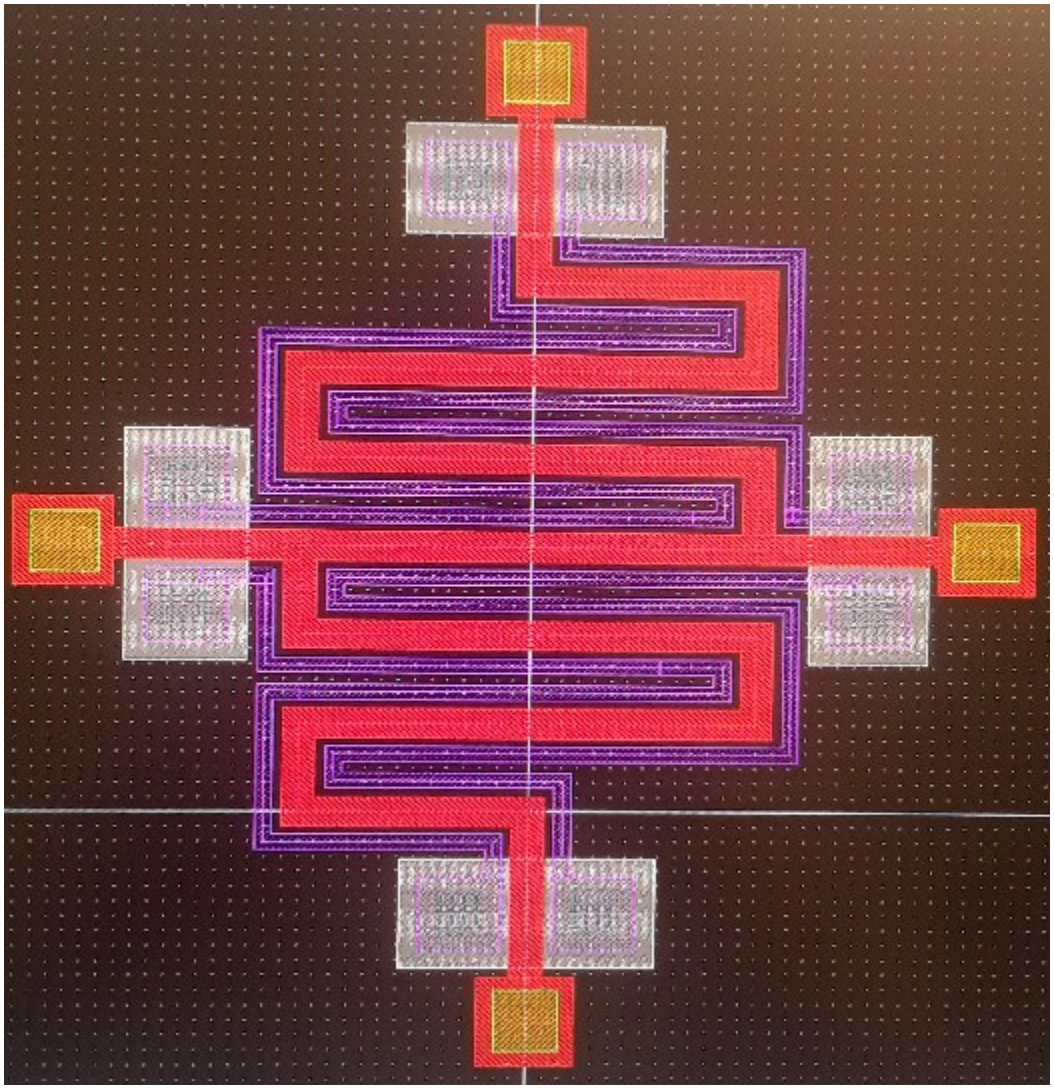

Fig. 5-61: Final Layout Design of the MHP using PolyMUMPs technology. Layer in red corresponds to the heater (POLY 1); layer in purple corresponds to the thermo-resistor (POLY 2). 4 rectangular layers in grey (POLY 0) are used to short-circuit 2 serpentine thermo-resistor layers.

As it is shown on Fig. 5-61, the heater layer (in red) runs parallel to two thermo-resistor layers (in purple). The heater is supported by four anchors (designated in yellow); the thermo-resistor is

supported by 8 anchors (designated in turquoise color). POLY 0 layer was used to short-circuit separate POLY 2 layers. POLY 0 lies underneath POLY 1 layer. Table 11 below presents the characteristics of the heater and sensor.

Table 11: Characteristics of the MHP designed using PolyMUMPs

	Width, µm	Length, µm	Resistivity, Ω/□
POLY 1	10	1050	5
POLY 2	5	2060	25

From Table 11, it is possible to calculate the resistances of the heater and sensor components by knowing the length and their resistivity. Table 12 presents the resistances of the heater and sensor.

Table 12: Resistances of the heater and sensor of the designed MHP

	Resistance, kΩ
Heater (POLY 1)	~ 0.5
Sensor (POLY 2)	~ 10

From the following design it is determined that $R_h = 0.5k\Omega$ and $R_s = 10k\Omega$. The reasoning behind these selections are explained in the following:

- Resistance of the thermo-resistor was intentionally chosen to be larger to decrease the current flowing and to minimize the overheating of the device.

- Resistance value of the heater was chosen such that to provide the overheating of the structure by an excitation voltage of up to 5V which is typical for the processing circuit. If the expected HLC of the structure is 30K/mW, then ~ 2mW is needed to overheat it by 60°C. This dissipated power is reached at approximately 1V excitation voltage for a 500Ω heater.

The designed MHP structure passed through the DRC check in Cadence Virtuoso and was planned for submission for fabrication through CMC. Electronic circuitries, signal processing algorithms, testing procedures and experimental setups developed for the existing thermal sensor and described in the previous chapters can be used in the same manner with the newly designed structure.

CHAPTER 7: CONCLUSION AND FUTURE WORK

7.1 Conclusions

The micro-hotplate designed using a CMOS compatible MEMS process was studied. The sensor was fabricated using First Sensor's Corp technology. The MHP comprised of two split polysilicon resistors which were used as an electric heater and a temperature sensor.

It was determined that with the addition of an Al slab atop of the MHP, non-uniformity of overheating temperature significantly reduces across the MHP and temperature distribution becomes more evenly spread. This results in a reduction of hot spots across the MHP which improves the sensitivity of the device.

The MHP with the newly developed signal processing circuitry demonstrated decent capability to measure tiny variations of thermal gas conductivity and vacuum pressure down to about 1mTorr. This feature was reached with the following limitations, which differ from traditional thermal gas sensors which use Nickel or Platinum for their structural membrane.

1) The thermo-resistor used as a temperature sensor was made from poly-Si (typical for CMOS process) with a TCR of -1300ppm/K. This TCR is significantly lower than the TCRs of Platinum and Nickel film resistors exceeding 4000ppm/K [7], [42], [12].
2) The surface area of the MHP is 0.02mm^2. This is also much lower than the area of traditional thermal gas sensors that have about 1-4mm^2 [7], [42], [10-12].

The operating mode of the MHP is characterized by a low dissipating power of about 2.2mW in gas sensing tests and 0.18mW at vacuum pressure measurements. The overheating temperature was limited to 40°C for atmospheric pressure and reached a maximum value of 72°C for high vacuum. A low operating temperature is preferable for poly-Si in order to provide better long-term stability.

The MHP has a high resolution to thermal gas conductivity and has estimated a minimal detectable variation of concentration of CO_2 in air of 165ppm and O_2 in air of 2000ppm.

The operation of the thermal sensor in the freeze-drying process was experimentally verified. Three sensors were placed inside the Freeze Dryer. The measured pressure gradients inside the vacuum chamber during the freeze-drying process were then obtained. Experimental results indicated a possibility of the sensors to detect changes in pressure gradients caused by the water sublimation process. A control system based on several miniature thermal sensors can indicate the end of primary drying stage that may be very important in the optimization of the freeze-drying technique and potential use in pharmaceutical and biological applications.

The designed MHP can be administered as a universal functional element for different thermal sensors used in gas sensing applications and vacuum pressure measurements.

7.2 Contributions

The following project was supported by NSERC-ENGAGE fund. First Sensor Corp. have fabricated the micro-hotplate for gas sensing and vacuum measurements and provided test samples and electronic boards. The objective of the project was to characterize and optimize the structure and its functionality. The device was successfully characterized and its signal processing algorithm was optimized. To further improve the device, an alternative fabrication method was proposed to develop a new micro-hotplate.

7.3 Suggestions for Future Work

The results of the first experimental tests of the MHP fabricated using CMOS compatible process demonstrated very high resolution of the device, ability to detect minimal variations in thermal conductivity of the ambient gas and changes in heat loss in vacuum. All tests were performed at room temperature and with a limited number of samples. To build real devices on the basis of the described MHP, further investigations should be conducted.

Characterization of temperature dependence of the sensor response is needed to provide sensor functionality in real operating conditions. The development of temperature compensation

algorithms is needed to maintain metrological characteristics of the sensors in the operating temperature range.

Investigation of long-term stability of the sensors is an important part of the developmental process. Possible optimization of the layout design, overheating temperature, operating mode, composition of poly-Si material (doping), drift compensation algorithms must improve the stability of the sensors' operation.

Signal processing circuit integration with the sensing element in one package is the important part of further development. The circuit should contain interfacing analog circuitry, analog-to-digital and digital-to analog converters and microprocessor implementing processing algorithms.

Further investigations of the developed vacuum sensors in freeze drying application are needed to build sensors' network for accurate monitoring of water sublimation across the volume of vacuum chamber with drying material. Optimization of recognition algorithms for identification of the end of primary drying process is of special interest.

Continuation of the development of an alternative MHP design based on poly-MUMPS process may bring new and interesting results. This MEMS structure has a small distance between the MHP and the surface of the Si wafer which significantly changes heat transfer in the vicinity of the MHP. The vacuum sensor based on this structure is expected to operate at higher pressures. Investigations of sensitivity of this new MHP to gas composition should be investigated.

References

[1] Patel, S. M., Doen, T., & Pikal, M. J. (2010). Determination of end point of primary drying in freeze-drying process control. *Aaps Pharmscitech*, *11*(1), 73-84.

[2] Ma, Y. (2004). *A Low-Cost Short-Distance Thermal Conduction Pressure Sensor* (Doctoral dissertation, School of Engineering Science-Simon Fraser University).

[3] Kimura, M., Manaka, J., Satoh, S., Takano, S., Igarashi, N., & Nagai, K. (1995). A new type humidity sensor using micro-air-bridge heaters. *Microsystem Technologies*, *1*(3), 143-148.

[4] Kimura, M. (1996). A new method to measure the absolute—humidity independently of the ambient temperature. *Sensors and Actuators B: Chemical*, *33*(1-3), 156-160.

[5] Kimura, M. (1996). Absolute-humidity sensing independent of the ambient temperature. *Sensors and Actuators A: Physical*, *55*(1), 7-11.

[6] Okcan, B., & Akin, T. (2007). A low-power robust humidity sensor in a standard CMOS process. *IEEE Transactions on Electron Devices*, *54*(11), 3071-3078.

[7] Simon, M., Dütsch, C., Schieferdecker, J., Storck, K., Völklein, F., & Grau, M. (2012). 1.1. 4 MEMS Pirani type vacuum sensor with extended sensitivity range. *Tagungsband*, 42-47.

[8] Shie, J. S., & Weng, P. K. (1994). *U.S. Patent No. 5,347,869*. Washington, DC: U.S. Patent and Trademark Office.

[9] *"Thermal Conductivity Gauge XEN-TCG3880"*, Xsensor Integration, Distributieweg 28 2645 EJ Delfgauw The Netherlands

[10] Van Herwaarden, A. W., & Sarro, P. M. (1988). Performance of integrated thermopile vacuum sensors. *Journal of Physics E: Scientific Instruments*, *21*(12), 1162.

[11] Van Herwaarden, A. W., Van Duyn, D. C., Van Oudheusden, B. W., & Sarro, P. M. (1990). Integrated thermopile sensors. *Sensors and Actuators A: Physical*, *22*(1-3), 621-630.

[12] Weng, P. K., & Shie, J. S. (1994). Micro-Pirani vacuum gauge. *Review of Scientific Instruments*, *65*(2), 492-499.

[13] Sisto, M. M., García-Blanco, S. M., Le Noc, L., Tremblay, B., Desroches, Y., Caron, J. S., ... & Picard, F. (2010). Pressure sensing in vacuum hermetic micropackaging for MOEMS-MEMS. *Journal of Micro/Nanolithography, MEMS, and MOEMS*, *9*(4), 041109.

[14] Wang, J., Yang, J., Chen, D., Jin, L., Li, Y., Zhang, Y., ... & Wu, F. (2018). Gas detection microsystem with MEMS gas sensor and integrated circuit. *IEEE Sensors Journal*, *18*(16), 6765-6773.

[15] Wang, C. C., Hou, Z. Y., & You, J. C. (2018). A high-precision CMOS temperature sensor with thermistor linear calibration in the (− 5 C, 120 C) temperature range. *Sensors*, *18*(7), 2165.

[16] Veeramani, P., Vimala, J. A., Sam, J. J., & Jagadish, R. (2018). Design and Fabrication of Temperature Sensor for Weather Monitoring System using MEMS Technology. *Oriental Journal of Chemistry*, *34*(5), 2510.

[17] Lee, C. Y., Lin, C. H., & Lo, Y. M. (2011). Fabrication of a flexible micro temperature sensor for micro reformer applications. *Sensors*, *11*(4), 3706-3716.

[18] Ahmed, M. G., Dennis, J. O., Khir, M. M., & Rabih, A. A. (2018, August). Characterization of Micro-heater and Temperature Sensor in Micro-electromechanical System Device for Gas Detection. In *2018 International Conference on Computer, Control, Electrical, and Electronics Engineering (ICCCEEE)* (pp. 1-6). IEEE.

[19] Fang, W. (1998). Design of bulk micromachined suspensions. *Journal of Micromechanics and Microengineering*, *8*(4), 263.

[20] Fan, J., Tan, C. S., & Pardhi, Y. (2012). Low temperature wafer-level metal thermo-compression bonding technology for 3D integration. *Metallurgy-Advances in Materials and Processes*, *52*(2), 302-311.

[21] https://sens4.com/pirani-working-principle.html

[22] Pikal, M. J., Roy, M. L., & Shah, S. (1984). Mass and heat transfer in vial freeze-drying of pharmaceuticals: Role of the vial. *Journal of pharmaceutical sciences*, *73*(9), 1224-1237.

[23] Khairnar, S., Kini, R., Harwalkar, M., & Chaudhari, S. R. (2014). A Review on Freeze Drying Process of Pharmaceuticals. *International Journal of Research in Pharmacy & Science*, *4*(1).

[24] Johari, H. (2003). Development of MEMS sensors for measurements of pressure, relative humidity, and temperature.

[25] Hsu, Tai-Ran. *MEMS & microsystems: design and manufacture*. Boston: McGraw-Hill, 2002.

[26] Madou, M. J. (2018). *Fundamentals of microfabrication: the science of miniaturization*. CRC press.

[27] Mehregany, M., & Zorman, C. A. (2001). Surface micromachining: a brief introduction. *MRS Bulletin*, *26*(4), 289-290.

[28] Judy, J. W. (2001). Microelectromechanical systems (MEMS): fabrication, design and applications. *Smart materials and Structures*, *10*(6), 1115.

[29] Bustillo, J. M., Howe, R. T., & Muller, R. S. (1998). Surface micromachining for microelectromechanical systems. *Proceedings of the IEEE*, *86*(8), 1552-1574.

[30] Landsberger, L. M., Grudin, O., Saed, S., & Frolov, G. (2014). *U.S. Patent No. 8,677,818*. Washington, DC: U.S. Patent and Trademark Office.

[31] Stix, G. "Micron machinations." *Scientific American* 267.5 (1992): 106-117.

[32] Mendoza-Acevedo, S., Reyes-Barranca, M. A., Vázquez-Acosta, E. N., Moreno-Cadenas, J. A., & González-Vidal, J. L. (2012). Release Optimization of Suspended Membranes in MEMS. *Micromachining Techniques for Fabrication of Micro and Nano Structures*, 183-204.

[33] Wang, J., Yang, J., Chen, D., Jin, L., Li, Y., Zhang, Y., ... & Wu, F. (2018). Gas detection microsystem with MEMS gas sensor and integrated circuit. *IEEE Sensors Journal*, *18*(16), 6765-6773.

[34] Deng, X., Zhang, L., Guo, J., Chen, Q., & Ma, J. (2017). ZnO enhanced NiO-based gas sensors towards ethanol. *Materials Research Bulletin*, *90*, 170-174.

[35] Hwang, W. J., Shin, K. S., Roh, J. H., Lee, D. S., & Choa, S. H. (2011). Development of micro-heaters with optimized temperature compensation design for gas sensors. *Sensors*, *11*(3), 2580-2591.

[36] Zhang, F. T., Tang, Z. A., Yu, J., & Jin, R. C. (2006). A micro-Pirani vacuum gauge based on micro-hotplate technology. *Sensors and Actuators A: Physical*, *126*(2), 300-305.

[37] https://www.engineeringtoolbox.com/air-properties-viscosity-conductivity-heat-capacity-d_1509.html

[38] Van Herwaarden, A. W., & Sarro, P. M. (1988). Integrated thermal vacuum sensor with extended range. *Vacuum*, *38*(6), 449-453.

[39] Koester, D., Cowen, A., Mahadevan, R., Stonefield, M., & Hardy, B. (2003). PolyMUMPs design handbook. *MEMSCAP Inc*.

[40] Carter, J., Cowen, A., Hardy, B., Mahadevan, R., Stonefield, M., & Wilcenski, S. (2005). PolyMUMPs design handbook. *MEMSCAP,*.

[41] https://www.engineersedge.com/heat_transfer/thermal-conductivity-gases.htm

[42] Alvesteffer, W. J., Jacobs, D. C., & Baker, D. H. (1995). Miniaturized thin film thermal vacuum sensor. *Journal of Vacuum Science & Technology A: Vacuum, Surfaces, and Films*, *13*(6), 2980-2985.